EXPERIMENTAL AND THEORETICAL APPROACHES IN MACROMOLECULES DESIGN, SYNTHESIS, MODIFICATION AND NANOSENSOR APPLICATIONS

by

MERVE SENEM AVAZ

Submitted to the Graduate School of Engineering and Natural Sciences

in partial fulfilment of the requirements for the degree of

Doctor of Philosophy

Sabancı University

July 2017

EXPERIMENTAL AND THEORETICAL APPROACHES IN MACROMOLECULES DESIGN, SYNTHESIS, MODIFICATION AND NANOSENSOR APPLICATIONS

APPROVED BY:

Prof. Dr. Yusuf Ziya Menceloğlu

....

(Thesis Supervisor)

Prof. Dr. Canan Atılgan

....

Assoc. Prof. Dr. Ayhan Bozkurt

....

Prof. Dr. Ersin Serhatlı

....

Assoc. Prof. Dr. Derya Yüksel İmer

....

DATE OF APPROVAL:

24 / 07 / 2017

To my beloved...

"Honey, your soul could never grow old; it's evergreen."

EXPERIMENTAL AND THEORETICAL APPROACHES IN MACROMOLECULES
DESIGN, SYNTHESIS, MODIFICATION AND NANOSENSOR APPLICATIONS

Merve Senem AVAZ

MAT, Doctor of Philosophy, 2017

Thesis Supervisor: Prof. Dr. Yusuf Ziya MENCELOĞLU

ABSTRACT

Chitosan shows merit as a biomaterial in medical research particularly in terms of its good biocompatibility, but its poor solubility at physiological pH values narrows its potential scope of use. In this first part of this thesis, a freeze-concentrated chemical modification approach was developed to transform chitosan, yielding derivatives with reduced chain regularity and improved solubility. In confirming the generality of this approach, chitosan solutions spiked with acrylic, citraconic, itaconic, or maleic acid were incubated at -10 °C, transforming primary amino groups to the corresponding Michael type adduct. The purified derivatives were characterized via ^{13}C-NMR, ATR-FTIR, XRD, ninhydrin, solubility measurements, and SEM, with changes in XRD and ninhydrin profiles particularly correlating well with improved solubility. It follows to reason that this approach enhanced processability of challenging or thermally sensitive biopolymers and contribute to the Michael reactions in the sense our method yields the free acid directly, which is in fact another novelty in chitosan research.

In the second part, a molecularly imprinted chitosan and graphene-based nanosensor was fabricated to selectively detect nitrotriazolone (NTO) molecules with a molecularly imprinted film via simple electrical measurements. Molecularly imprinted polymer comprising chitosan was

used as sensitive layer. Gold electrodes for electrical measurements were lithographically fabricated on Si/SiO2 substrate, followed by monolayer graphene transfer and polymeric film coating. Monolayer graphene and molecularly imprinted polymer were characterized by ATR-FTIR, UV-Vis, SEM and Raman spectroscopy. Transfer-length measurements (TLM) indicate that the sensor selectively and linearly responds against aqueous NTO solutions within a wide range of concentration of 0.01–0.1 mg mL_1 that covers the lowest toxic level of NTO determined by USEPA. This nanosensor with embedded electrodes is re-usable and suitable for field applications, offering real-time electrical measurements unlike current techniques where complex analytics are required.

Third part of the thesis deals with theoretical investigation of structure-morphology-property relationship in thermoplastic polyurethanes. Soft segment (SS) chain length is known to affect the morphologies and mechanical behavior of poly(ethylene oxide) based-segmented poly(urethane-urea) copolymers in binary solvents. Here, a multi-scale computational study is carried out to determine the origins of this behavior. First, single chains of a series of poly(ethylene oxide) (PEO) of varying lengths are comparatively examined by molecular dynamics (MD) and dissipative particle dynamics (DPD) simulations in THF:DMF mixture to verify that the coarse graining strategy is applicable to the system at hand. In the second step, hard segment (HS) beads containing urethane groups are attached into PEO chains to study the effect of hard segment on morphology. Density fields obtained from DPD calculations results in a stable channel formation of soft segment molecules in the copolymers with the lower soft segment lengths. Morphologies of copolymers with three different soft segment lengths investigated by DPD are followed by reverse mapping to full atomistic detail. Monitoring the trajectories and the reverse mapped structures, we find that urethane-PEO interactions are significantly stronger in copolymer with lowest soft segment length leading to channel formation. The findings are corroborated by atomic force microscopy (AFM) images obtained for the corresponding copolymers. The strategy employed in this work lays the foundations for predicting novel morphologies and macro-properties using designs based on HS-SS cooligomers.

MAKROMOLEKÜLLERİN DİZAYNI, SENTEZİ VE MODİFİKASYONUNDA DENEYSEL
VE TEORİK YÖNTEMLER VE NANOSENSÖR UYGULAMALARI

Merve Senem AVAZ

MAT, Doktora Tezi, 2017

Tez Danışmanı: Prof. Dr. Yusuf Ziya MENCELOĞLU

Anahtar kelimeler: Kitosan Modifikasyonu, Donma derişimi, Moleküler Çapraz Bağlama, Grafen, Nanosensör fabrikasyonu, Moleküler dinamik simülasyonu, Orta ölçek moleküler dinamik, Yapı-morfoloji-fonksiyon ilişkisi

ÖZET

Kitosan makromolekülü özellikle yüksek biyouyumlulukta bir biyomalzeme olması sebebiyle biyomedikal araştırmada sıklıkla kullanılmaktadır. Kitosanın bu alanda daha geniş kullanımının önünde en büyük problem fizyolojik pH değerlerinde düşük çözünürlüğüdür. Bu tezin ilk aşamasında kitosanın donma derişimi reaksiyonlarıyla kimyasal modifikasyonu gerçekleştirilmiş ve zincir düzenliliği düşük ve yüksek çözünürlükte kitosan türevleri elde etmek hedeflenmiştir. Bu amaçla hazırlanan kitosan çözeltileri organik asitler ile karıştırılarak b -10 derecede Michael katılma reaksiyonu gerçekleştirilmiştir ve kitosanın yapısında bulunan ve yüksek kristalinite, dolayısıyla düşük çözünürlükten sorumlu olan birincil amin grupları ikincil ve üçüncül aminlere indirgenmiştir. Sentez sonrasında saflaştırılan türevler ^{13}C-NMR, ATR-FTIR, XRD, ninhidrin testi, çözünürlük testleri, XRD ve SEM ile karakterize edilmiştir. Özellikle XRD ve ninhidrin testleri artan çözünürlüğü doğrulamıştır. Diğer bir taraftan, tezin bu aşamasında kullanılan donma derişimli kimyasal reaksiyon yöntemi ile termal olarak hassas ve zor işlenen biyomalzemelerin modifikasyonuna alternatif bir yöntem sunarken, reaksiyon esnasında serbest asidin doğrudan elde edilmesi de Michael katılması reaksiyonları literatürüne bir katkı sağlamaktadır.

Tezin ikinci kısmında nitrotriazolon (NTO) moleküllerini çevresel su ve toprak örneklerinden algılamak için moleküler baskılama yöntemiyle hazırlanan kitosan film ve grafenden oluşan bir nansensör üretilmiştir. Elektriksel ölçümleri gerçekleştirebilmek için altın elektrotlar Si/SiO$_2$ substrat üzerine litografi yöntemiyle işlenmiş, bunu takiben elektrotlar üzerine tek tabaka grafen yerleştirilmiştir. Moleküler baskılanmış kitosan filmler ise sensörde en üst tabaka olan algılayıcı tabaka olarak kullanılmıştır. Sensör üzerindeki tek tabaka grafen ve moleküler baskılanmış film ATR-FTIR, UV-Vis, SEM ve Raman teknikleriyle karakterize edilmiştir. Elektriksel TLM ölçümleri üretilen nanosensörün NTO moleküllerinin USEPA tarafından belirlenen toksik seviyelerini de kapsayan 0.01-0.1 mg/mL aralığında seçici ve lineer bir şekilde yanıt verdiğini göstermiştir. Yapılan çalışmalar üretilen nanosensörün çok kullanımlılık, eş zamanlı ölçüm ve saha uygulamalarına uygun olması nedeniyle diğer kompleks tekniklere göre daha avantajlı olduğunu göstermektedir.

Tezin üçüncü kısmı termoplastik poliüretanların yapı-morfoloji-fonksiyon ilişkisinin teorik çalışması üzerinedir. PEO bazlı segmente termoplastik poliürethanlarda yumuşak segmentin zincir uzunluğunun morfoloji ve mekanik özellikleri etkilediği bilinmektedir. Bu çalışmada bu özelliğin temellerini belirlemek adına çok ölçekli hesaplamaya dayalı bir çalışma gerçekleştirilmiştir. Bu amaçla ilk aşamada uygulanacak iri taneleme (*coarse graining*) stratejisinin geçerliliğini doğrulamak adına zincir uzunlukları değişen bir dizi tek zincirli PEO yapıları THF:DMF çözücüleri içerisinde moleküler dinamik (MD) ve dağılımlı parçacık dinamiği (DPD) yöntemleriyle incelenmiştir. İkinci adımda iri taneleme yöntemiyle elde hazırlanan yumuşak segment (SS) PEO modellerine yine aynı yöntemle hazırlanan sert segment (HS) taneleri eklenerek bu segmentin morfoloji üzerindeki etkileri incelenmiştir. DPD hesaplamalarından elde edilen yoğunluk alanları kısa yumuşak segment zincirli kopolimerlerde stabil kanal yapılarının oluştuğunu göstermiştir. Üç farklı kısa segment zincir uzunluğunda hazırlanan kopolimerin morfolojileri DPD ile incelenmiş ve ardından "ters haritalama" yöntemiyle atomistik detaylar eklenmiştir. Ters harita modelleri ve DPD sonuçları üretan-PEO etkileşimlerinin kısa zincirli kopolimerde belirgin bir şekilde daha güçlü olduğu gözlenmiş ve bu etkileşimlerin yapıda oluşan kanallara yo açtığı belirlenmiştir. DPD bulguları AFM görüntüleriyle

de desteklenmiştir. Çalışmada kullanılan strateji HS-SS ko-oligomerleriyle dizayn edilecek yeni ve özgün morfolojilere ve makro-özelliklere temel oluşturmaktadır.

ACKNOWLEDGEMENTS

TABLE OF CONTENTS

LIST OF FIGURES

LIST OF TABLES

LIST OF SYMBOLS AND ABBREVIATIONS

MW   : Molecular weight

PEG   : Polyethylene glycol

H-bond   : Hydrogen bond

EDTA   : Ethylenediaminetriacetic acid

FC   : Freeze Concentration

FTIR   : Fourier Transformed Infrared spectroscopy

ATR-FTIR   : Attenuated Total Reflectance- Fourier Transformed Infrared spectroscopy

^{1}H-NMR   : Proton Nuclear Magnetic Resonance

^{13}C-NMR   : Carbon-13 Nuclear Magnetic Resonance

XRD   : X-Ray Diffractometry

SEM   : Scanning electron microscopy

TGA   : Thermogravimetric analysis

NTO   : Nitrotriazolone

CS   : Chitosan

TLM   : Transfer Length Measurements

GA   : Glutaraldehyde

CVD   : Chemical Vapor Deposition

PMMA   : Poly(methyl methacrylate)

SEI   : Secondary Electron Intensity

Uv-Vis   : Ultraviolet-Visible

HS   : Hard Segment

SS   : Soft Segment

THF   : Tetrahydrofuran

DMF   : Dimethyl formamide

PEO   : Poly(ethylene oxide)

TPU   : Thermoplastic Polyurethane

MD   : Molecular Dynamics

DPD   : dissipative Particle Dynamics

AA   : All atom

AFM   : Atomic Force Microscopy

RDF   : Radial Distribution Function

QM   : Quantum Mechanics

NPT   : Constant Temperature and Pressure

NVE   : Constant Energy and Volume

NPH   : Constant Pressure and Enthalpy

NVT   : Constant Volume and Temperature

COMPASS   : Condensed Phase Optimized Molecular Potentials for Atomistic Simulation
             Studies

CED   : Cohesive Energy Density

HMDI: Bis(4-isocyanatocyclohexyl)methane

DBTDL: Dibutyltin dilaurate

IPA: Isopropyl Alcohol

MDAP: 2-methyl-1,5-diaminopentane

CHAPTER 1 Introduction

This thesis is composed of five chapters, in which, synthetic, and theoretical approaches were employed to modify/process and understand the nature of the material at hand that serve in various applications. The first and the fifth chapter are brief descriptions of other chapters and a conclusion, respectively. The second chapter deals with verification of an unusual reaction method, which is useful to chemically modify natural materials. The method called as freeze concentration (FC) reactions has been known for over decades and is validity was approved with small organic molecules' reactions. On the other hand, this method has not been tested on synthesis or modification of macromolecules especially thermosensitive macromolecules. For this purpose, a model macromolecule was selected to test the validity of proposed reaction tool. The model macromolecule chitosan is a widely used naturally occurring biopolymer with various advantages as a biomaterial, such as low toxicity, biocompatibility and biodegradability. On the other hand, its processability is lowered by low solubility in physiological pH values. Therefore the selected reaction pathway is aimed to increase its solubility while proving the applicability of FC reactions in macromolecular scale. At the end of FC reactions; the product was chemically characterized by spectroscopic techniques such as NMR, FTIR and with chemical indicator methods. In addition to this, crystallinity, thermal and morphological properties were also investigated by X-Ray diffraction spectroscopy (XRD), thermogravimetric analysis (TGA), and scanning electron microscopy (SEM) methods. With this chapter, the concept of freeze concentration reactions is proven to be a useful tool in chemical modification of thermosensitive macromolecules.

The third chapter describes the design, fabrication and performance optimization of a chemical nanosensor to detect trace amount of nitroaromatics from ecological samples. The use of toxic nitroaromatics in military and other purposes has long been an environmental issue, which was reported by numerous environmental health and safety authorities. The first act in preventing a contamination is to detect the toxic amounts of analyte of subject. With this motive, we aimed to develop a chemical sensor that is able to detect the toxic levels of nitroaromatics on site. But one

of the main challenges in design of a sensor to detect very low concentrations of the analyte requires high sensitivity and selectivity. Thanks to the recent developments in nanotechnology and its reflections on fabrication techniques, scientific methods of today enable us to develop sensors to meet these criteria. The extraction of monolayer graphene did not only earned Prof. Geim and Novoselov a noble prize, but it also introduced the exceptional properties of this 2 dimensional material to research world. The main advantage that comes with monolayer graphene was its remarkable electrical properties. As a zero-overlap semimetal with both holes and electrons as charge carriers, graphene has a very high electronic mobility, which directed us to the idea of detecting very low concentrations of analyte with high sensitivity and thus inspired us to use this material as the transducer layer in our nanosensor. On the other hand, selectivity of the designed sensor was improved by employing molecularly imprinted polymers as the active layer of the sensor. Molecular imprinting technique creates shape-specific recognition sites on polymers that interact template molecule and reject others. On the other hand, nitroaromatics are known to form reversible salts with amine groups. Therefore, the molecular imprinting technique was applied on chitosan and this biopolymer was selected as active layer due to its good film forming properties and vast amount of primary amine groups to ensure the interaction with analyte not only through shape recognition, but also through secondary interactions. Chemical characterizations of the analyte components were performed using FTIR and Raman spectroscopic techniques.

In addition to its materials selection, advances in nanotechnology also reflected on sensor fabrication methods. To detect the change in electrical properties of graphene upon interaction of the active layer with the analyte, we needed metallic electrodes to carry out the measurements. In literature examples of electrical measurements of graphene, the electrodes are usually placed on top of graphene layer that lies on an insulated substrate. Although this approach was proven to be useful, we faced with severe contamination issues during fabrication and contact development steps. Therefore, we employed a reverse-approach in electrode placement and embedded the electrodes inside the substrate. This "*embedded electrodes*" approach is developed in Sabancı University Nanotechnology Research and Application Center facilities, and to our knowledge, is a unique design and a first in literature.

2

To detect the change in sheet resistance of graphene upon analyte interaction, electrical measurement were carried out using Transfer Length Measurement (TLM) method. For this purpose, the metallic contact lines were placed in an increased distance pattern, and a series of I-V measurements were performed to measure the sheet resistance. TLM measurements indicated that the developed sensor is sensitive enough and respond selectively to toxic levels of the analyte. The main improvements that come with the developed sensor can be listed as the easy measurement technique that is suitable for on-field measurements, its wide range of response against the analyte in acceptable response times and low levels of noise.

The fourth chapter deals with theoretical investigations on structure-morphology-function relationship of poly(ethylene oxide based poly(urethane-urea) copolymers. Thermoplastic polyurethanes (TPUs) are versatile copolymers possessing both flexibility that comes with its soft segment (SS) of poly(ethylene oxide) (PEO), and toughness comes with its hard segment (HS). Experimental evidences reveal that several functions such as mechanical properties of TPUs differ with respect to SS chain length. Although there are numerous experimental and theoretical studies available on explaining the change in macro properties of TPUs, the structural explanation on this change has not been explained in detail. The question of the effect of SS chain length on morphological properties of PEO based TPUs constitutes the main objective of the third chapter of this thesis. With the improvements in computing power over the past decades, Molecular Dynamics (MD) simulations enable the researchers to observe atomistic events of macromolecules in nanosecond time scales. But MD simulations today are only limited to model macromolecules up to 10000 atoms, and production of models with multiple polymer chains and solvent molecules requires very high computing costs. On the other hand, Dissipative particle Dynamics (DPD) simulations allow simulations of the dynamic of systems with multiple polymer chains over longer time periods. This is done by a coarse grained approach that clusters sets of atoms into beads. Therefore, DPD can be defined as a scale-up method for MD simulations where bead interactions are produced, but the atomic information is lost. A solution to atomic information loss during DPD is fine graining, where the atomic information can be re-introduced to DPD models.

To find an atomistic scale explanation to the change in macroscopic properties of TPUs with varying SS chain length, we employed a multi scale computational approach. The first step in this approach is the development of single chain models of PEO chains, which serves as SS, and comparison of all atom and coarse-grained models by MD and DPD simulations. By comparing all atom simulation results with DPD in terms of end-to-end distances, we aimed to assess the validity of DPD model. In the second step, we prepared multiple chains of copolymer by incorporating HS beads into the model and carry out DPD simulations of copolymer. DPD results were then compared to Atomic Force Microscopy (AFM) results in terms of morphology. In the final step, atomic information is re-introduced into DPD models by reverse mapping method. This chapter provided useful information on the unusual behavior of PEO based TPUs on atomistic level where experimental data is not available. The findings of the study are useful in understanding the nature of these types of copolymers and enable researchers to design of novel materials with fine-tuned properties in the future.

CHAPTER 2 Freeze-Concentrated Modification of Chitosan to Water-Soluble Derivatives

2.1 Introduction

Although its history dates back to 1850s, the interest in Chitosan has increased dramatically in the 1970s along with the increase in natural products, and has been growing ever since [1]. Today Chitosan, N-deacetylated form of its precursor chitin, is a widely used biological material with its remarkable properties of biocompatibility, biodegradability, low toxicity and many others [2]. Therefore, researchers have particularly focused on its biomedical applications, mostly in the areas of drug delivery systems, biotechnology, tissue engineering and wound dressing materials [3, 4]. Figure 1 is an abstract of chitosan and its prominent properties in terms of polymeric, chemical, pharmacological, biomedical and environmental importance.
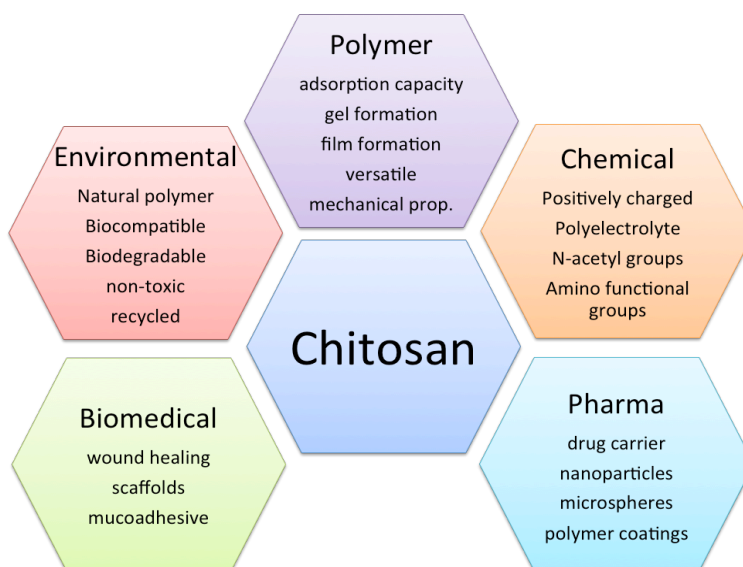
Figure 1 Schematic representation of general overview of chitosan

As alkaline solution-treated (e.g. sodium hydroxide) form of its precursor chitin, commercial chitosans are found in deacetylation degrees of 60-90%. Deacetylation is usually carried out by treating chitin with concentrated alkali solution for 6-7 h. It was shown that the reaction time has

more influential effect on degree of deacetylation than alkali concentration [5]. On the other hand, deacetylation via enzymatic degradation is an alternative to thermochemical conversion of chitin. For this purpose, chitin deacetylase enzyme is used to catalyse the deacetylation reaction of N-acetyl glucosamine residues [6].

In addition to degree of deacetylation, molecular weight (MW) is also another important factor that determine many physical properties of chitosan. High MW chitosans has a molecular weight range of 310-375 kDa, whereas low MW ranges between 50-190 kDa. It was shown that tensile strength of high molecular weight chitosans were higher that that of low molecular weight [7]. Moreover, aqueous solutions of high molecular weight chitosans exhibit very high viscosity, thus their applications are limited [8].

Despite the fact that Chitosan is a good candidate for biological uses with its promising properties, its processability is lowered by poor water solubility especially at basic pH values. This solubility issue of biopolymer arises from its crystalline structure [9] that is mainly established by high regularity of intermolecular Hydrogen bonds between the polymer chains and the sheets. Figure 2 shows the chemical structure of chitosan repeating unit. Chitosan biopolymer composes of two randomly distributed monomeric units, glucosamine and N-acetyl glucosamine, respectively. The amino groups and hydroxyl groups attached to D-glucosamine monomer unit gives the structure an intra- and intermolecular H-bonding regularity, which enhances the crystallinity of the structure. In addition to the basic nature of amino groups (Pka=6.5) [10], crystallinity is the main obstacle against water solubility. Therefore, one has to derange the regularity of Hydrogen bonds within/between polymer chains in order to overcome the solubility issue of the polysaccharide.

Chitosan has shown to exhibit different structural behavior than its precursor chitin due to the free primary amino groups introduced by deacetylation. Moreover, solid-state chitosan is found in different conformations than hydrated form, differentiating hydrogen bond formations [11].
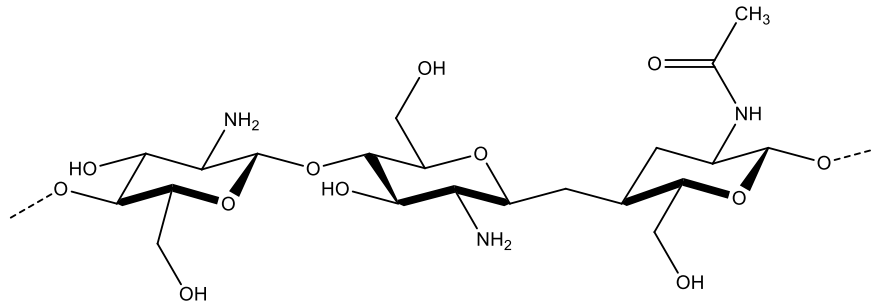
Figure 2 Chemical Structure of chitosan.

Chemical modification of amino groups gives rise to an increase in solubility of Chitosan by decreasing the crystallinity of the molecule. As the regularity of the structure decreases by adding bulkier side groups upon Michael addition, intermolecular spacing within backbone of the polymer chains enlarges and allows more water molecules to access. Although there are several synthetic routes available to modify H-bond forming groups within the monomeric units, perhaps the most direct approach is to modify primary amino groups of the N-deacetylated monomeric units. Besides, pH solubility range of the molecule also widens upon modification, due to the decrease in the number of amino groups, which are only soluble in acidic pH values.

2.1.1 Literature Review

In general, there are two synthetic approaches to soluble chitosan; N-substitution and O-substitution of the monomeric cyclic unit via two different reaction sites. Here, the primary reaction site is the N-group, where the nucleophile substitution reactions are more probable. These types of reactions include N-alkylation [12], N-acylation [13], N-carboxyalkylation, N-sulfation [14] and quaternization [15]. On the other hand, there are some O-substitution reactions reported in the literature by suppressing N-substitution via experimental conditions with [16] /without [17] using N-protective agents. Due to its more nucleophillic nature, N-site of the monomeric unit is more preferable in chitosan solubilization reactions.

2.1.1.1 N-Alkylation of Chitosan

In literature, there were several attempts to improve chitosan's solubility, or widen its pH-solubility range by N-alkylation reactions. In 2000, Sashiwa *et. al.* [18] employed N-reductive alkylation to prepare alkyl derivatives of chitosan using p-formylphenyl α-sialoside as alkylating agent; $NaCNBH_3$ as reducing agent and successfully proved the lectin binding capacity of the newly formed derivative. It was shown that this chitosan derivative was only soluble when prepared in high degrees of substitution. In another example, N-alkyl derivatives of chitosan was prepared with levulinic acid, and it was observed that the solubility of end products were dependent on degree of substitution [19].

In the following years, N-alkylation of chitosan with mono- and disaccharides was carried out and it was found out that chitosan derivatives with disaccharides are soluble around physiological pH [20]. This group also stated that rheological properties of chitosan derivatives were related with degree of substitution, e.g., aqueous solutions switched from pseudo-plastic to Newtonian as the degree of substitution increased. Strategically-similar, Yang *et. al.,* prepared a set of N-alkylated disaccharide derivatives of chitosan and optimized the degree of substitution and its effect of on antibacterial activity [21]. This report stated that a degree of disaccharide substitution around 0.3-0.4 showed the highest antibacterial activity at physiological pH. Authors related this property primarily with the change in pH-solubility range. As another example of increased solubility with N-alkylation, polyethylene glycol (PEG) was grafted into chitosan by N-alkylation and drug release kinetics were studied [22]. It was shown that solubility and viscosity in 40% of PEG alkylation was enough to prepare an injectable solution of chitosan derivative. In addition, it was demonstrated that a linear release between to 5 to 70 hours was achieved with injected liquid, while prolonged release up to 40 days was possible with crosslinking.

Higher degrees of substitution may not always be necessary to overcome the poor solubility issue of chitosan biopolymer. In a report [23], it was claimed that low degrees of substitution around 0.03 was enough to prepare water-soluble chitosan at neutral pH without disrupting its cationic nature. In another study [24], where chitosan was hyper branched with chitosan side-chains, it was stated that chitosan derivatives with a degree of hyper branching of 0.04-0.06 exhibited good water-solubility. The study conducted by Ying *et. al* in [25] may be addressed as an extended

version of [24] since they also hyper branched chitosan but expanded the reaction dataset with various carbohydrates. They showed that reduced viscosities of the water-soluble chitosan derivatives were decreased with increasing degree of substitution. In addition, they quantitatively showed that all the derivatives prepared were soluble at neutral and basic pH values. Worth to mention, this study is the first in quantitative solubility testing of chitosan modification.

Another factor that affect the solubility of chitosan derivatives is the structure of side-chain attached to chitosan backbone upon modification. In a recent study Buranaboripan *et. al.* prepared β-cyclodextrin aldehyde derivatives of chitosan by reductive alkylation and showed that water solubility was affected by residue side-chain length and flexibility [26].

Although it is mainly employed to increase the solubility of chitosan, there are some examples of alkylation reactions, which put additional properties into structure and widen its applications. In order to take the advantage of both hydrophilicity and hydrophobicity arising from different side chains and thus controlling the solubility, Ramos *et. al.* [27] introduced insoluble alkyl branches into a water soluble chitosan derivative (N-methyl-) containing phosphonic groups. This way, they increase the water solubility in neutral conditions and moreover, integrated amphiphilic aspects and extended emulsifying properties of chitosan. Same group prepared another water-soluble chitosan derivative by adding an longer alkyl chain (N-propyl-) into chitosan backbone and showed that solubility was slightly increased upon addition of longer alkyl chain [28]. A similar approach was adapted by Ngimhuang *et. al.* [29], where they substituted a long alkyl chain and a hydrophobic residue into chitosan structure by N-alkylation and aimed to enhance the versatility of chitosan in terms of polymeric surfactant. They reported that the stability of polymeric micelles was highly dependent on the degree of substitution of hydrophobic side-chain.

As another important aspect to mention, chemoselectivity becomes prominent in some N-substitution reactions including N-alkylation since there are available primary and secondary hydroxyl groups attached to both glucosamine and N-acetyl glucosamine rings that form the backbone of chitosan ring in random distribution. To prevent O-alkylation, protective groups may be used. Másson *et. al.* developed a chemoselective reaction strategy to prepare N,N,N-trimethyl

derivatives of chitosan using an O-protector prior to N-alkylation reaction [30]. The resulting products were fully water-soluble with no sign of O-alkylation.

There are alternative methods to conventional wet-preparation of N-alkyl chitosans in the literature, such as microwave-assisted reactions. In the study conducted by Petit *et. al.*, N-alkylation was carried out by microwave irradiation and resulting derivative exhibited similar rheological and surface properties without breaking biopolymer's backbone [31]. This method was advantageous in terms of having shortest reaction times to amphiphilic derivatives and degree of conversion. In a study conducted in 2016, methylation of chitosan was carried out using deep eutectic solvent mixtures of urea and glycine [32]. Unlike conventional methods, which employ hazardous organic solvents such as DMF, this method allowed selective methylation using eco-friendly "green chemicals". These very recent examples highlight that the trend in chitosan modification research is propagating towards alternative reaction methods.

2.1.1.2 N-Acylation of Chitosan

N-acyl chitosans were widely studied in the literature, frequently in terms of their solubility, structure-function relationships, and biomedical applications. Therefore literature survey in this section is divided into 3 subsections with respect to the subjects described above.

Solubility: There are vast amount of studies in the literature that correlates solubility of N-acyl chitosan with degree of substitution and acyl chain length. For instance, Badawy *et. al.* prepared N- and O-acyl derivatives of chitosan and stated that derivatives exhibited higher solubility than native chitosan [33]. In addition, they reported that antifungal activity of the derivatives were significantly higher than native chitosan. Another group; Lee *et. al.* studied the effect of degree of substitution on solubility and effect of acylation on crystallinity, hence solubility [34]. They prepared a set of acylated chitosan and observed that degree of acylation and solubility are inversely proportioned. According to Lee, chitosan derivatives with a degree of acylation <0.6 were insoluble even in acidic medium, whereas samples with degree of acylation of 0.1 and 0.2 are fully soluble at pH 4.0. They added that, independent of the acylation degree, all samples were insoluble above pH 7.0. On the other hand, they stated that samples with a low acylation degree were soluble, because only low extents of acylation helped crystallinity to be destroyed.

As the substitution rate increased, hydrophobic character of the polymer became more dominate and resulted in lower solubility; independent of the decrease in crystallinity. From the literature examples it can be concluded that solubility of acyl derivatives of chitosan depend on two parameters; degree of substitution and acyl chain length. There's an inverse proportion between acyl chain length and solubility. In addition, solubility also increases with decreasing degree of substitution in chitosan derivatives with short acyl chains. On the other hand, chitosan derivatives with high degree of acylation are insoluble in water, independent of acyl chain length. In a very recent study, Fujita and Sakairi synthesized water-soluble chitosan-ethylenediaminetriacetic acid (EDTA) by acylation [35] to remove copper ions from drinking water. They reported that the newly synthesized derivative acted as a very strong chelating agent due to its wide range of pH solubility and amphoteric nature.

Structure & Function: In [36] it was reported that the hydrophobic character of chitosan increased during acylation with fatty acids which was believed to enhance the stability of chitosan due to "self assembly". Jiang *et. al.* developed a method to prepare amphiphilic chitosan micelles by N-fatty acylation and obtained water-soluble N-acyl derivatives [37]. They stated that the derivatives prepared by N-acylation showed higher stability than a previously reported coupling reaction derivative of chitosan [38]. In another report on stability upon N-acylation [39], 3-dimensional nano-matrices of different modified polycations were prepared to stabilize iron oxide nanoparticles. Among the polycationic matrices produced, N-acylated chitosan demonstrated the highest stability at physiological pH. Evaluated from a different viewpoint, Choi *et. al.* reported that, after N-acylation, chitosan derivatives with longer acyl side chain exhibited higher tensile strength [40]. In the same report it was also highlighted that mechanical properties were enhanced upon N-acylation when compared to N-acetylated chitosans.

Biomedical: One of the first acylation reactions of chitosan was carried out in solid state with a series of carboxylic anhydrides. Hydrolysis rates of acylated fibers were tested with Lysozyme and it was shown that the length of side chain added upon acylation affects the rate of hydrolysis [41]. To evaluate a different biomedical property, Hu et. al. prepared two N-acyl chitosan derivatives of which they investigated antibacterial activities n relation with self-aggregation due to hydrophobic groups introduced upon N-acylation. They showed that N-acyl product with a

longer alkyl side chain was more hydrophobic; creating more self-aggregation, and exhibited better antibacterial activity than the N-acyl derivative with shorter alkyl side chain [42]. To examine the mucoadhesive behavior, Shelma & Sharma prepared 3 N-acyl chitosan derivatives (hexanoyl/ lauroyl/oleoyl chitosan) and observed that acyl chitosans exhibited better mucoadhesive properties than untreated chitosan and found non-toxic to human tissue cells [43]. In addition, they conducted release-kinetics experiments and as a result, addressed acyl chitosans as promising carriers for hydrophobic drugs. As a controlled delivery system of antitumor agent atorvastatin, N-acylated chitosan micelles encapsulated this antitumor agent reported as promising in terms of enhanced sustained release and cytotoxic activity compared to non-capsulated agent [44]. This behavior of acyl chitosan was attributed to stability in aqueous solutions. In another study [45], an acylation reaction was developed and N-acyl chitosan derivative was employed as bioactive coating to increase the shelf life of strawberries. Acyl chitosan was reported to have antifungal agent carrier property, thus useful as an edible coating.

2.1.2 Frozen Solutions and Their Use as Reaction Tool

Freezing of an aqueous solution starts with the crystallization of water molecules into solid form. These crystallization events first take place with nucleation of solvent molecules and as the temperature decreases solvent molecules have been removed from the solution as in the form of pure ice. Thus the solute molecules are concentrated in the remaining solution and this increase in concentration continues 'till the eutectic point. This phenomenon is called as freeze concentration (FC) and has been practiced for decades [46], especially for water separation applications and in food industry [47]. When applied to a reaction mixture, water content in the reactor decreases due to crystallization. This gives rise to a dramatic increase in both concentration and viscosity of reactants and thus higher reaction rates become possible even at low temperatures. In other words, the increase in concentration and viscosity may compensate the drawbacks of low temperature and allows chemical reactions to take place at sub-zero degrees.

Frozen solutions can be considered as systems that take the advantage of increased concentration due to freeze-concentration effect. One of the first reported proofs of this effect is the dramatic difference between the rates of super cooled and frozen solutions ethylene chlorohydrin reaction

with sodium hydroxide. The rate of this frozen solution reaction was reported as 1000 times faster than that of super cooled liquid [48]. Freeze concentration (FC) has recently been experimentally verified in a study by Sodeau et. al. [49] in which an interhalide formation in polar regions arising from FC of dilute solutions was investigated and freezing was shown to enhance the formation of IBr_2^- and explained the chemistry behind ozone depletion events in polar troposphere.

So far, several FC reactions have been carried out and verified in the literature, both for small organic reactions [50] and at macromolecular level, especially in terms of cryogel synthesis [51]. Cryogel formation, or in other words, cryotropic gelation is a unique gelation process that occurs upon cryogenic treatment of the reaction components. Chitosan cryogels have also been received widespread attention of the researchers with their improved swelling properties [52].

The purpose of this study is to verify the validity of FC method on organic reactions of biomacromolecules. To achieve this, Michael addition of chitosan with acrylic acid proposed by Sashiwa *et al.* [53] was selected as the model system and expanded with several organic acids including citraconic, maleic and itaconic acids. To verify the validity of the FC reaction, an ^{13}C-labeled methylation reaction was carried out based on the conclusive fact that ^{13}C-iodomethane can only be reacted with available primary amino side groups that remained unchanged after Michael addition reaction. Results showed that FC reactions were performed successfully, and the products obtained by FC effect showed better pH solubility ranges and several morphological differences than those obtained by conventional method.

2.2 Materials & Methods

Chitosan and ^{13}C-iodomethane were purchased from Sigma Aldrich, Germany. Chitosan, from crab shells, was in practical grade with degree of deacetylation $\geq$ 85 and viscosity > 200. ^{13}C-iodomethane was 99 atom % in [13]C. All the solvents, organic reagents and crosslinking agents were in practical grade.

^{1}H- and ^{13}C-NMR spectra were recorded on Varian Inova 500MHZ NMR Spectrometer. FTIR spectra were recorded on Thermo Scientific Nicolet IS10 ATR-FTIR Spectrometer equipped with diamond Smart ATR Attenuated Total Reflectance sampling accessory. The minimum and

maximum range limits were 550 to 4000 cm^{-1} with a resolution of 0.5 cm^{-1}. X-Ray diffraction patterns were collected using Bruker AXS D8 Advance XRD (Cu-Kα radiation). Zeiss LEO Supra 35VP Field Emission Scanning Electron Microscope was used to study the morphology of chitosan derivatives with SEI detector.

D$_2$O/CH$_3$COOH and D$_2$O/HCl solutions (10:1 v/v) were used to acquire ^{1}H- and ^{13}C-NMR spectra, respectively. Analyte concentrations in NMR measurements were 10mg/mL ^{1}H- and 60mg/mL for ^{13}C-NMR. XRD and ATR-FTIR spectra were collected using freeze-dried chitosan powders.

2.2.1 Preparation of N-Carboxy- Derivatized Chitosan

Michael addition was carried out according to the study [53], except the temperature was fixed at -5°C. Briefly, 2 g of chitosan was dissolved in 100 mL of 1% acetic acid by stirring overnight and filtered. After the filtration, a solution of each reactant (10% wt.) was added into chitosan solutions. The resulting solutions were divided into two parts. First part of each chitosan reaction mixtures were stirred at 50°C overnight, whereas second parts were stirred at -5°C. Details of reaction conditions and mixtures are found in Table 1 and Table 2. After the reactions were completed, 0.5 M NaOH were added into mixture to adjust the pH at 6.0. The mixtures were then dialyzed using a dialysis membrane (MW cutoff= 3.5K) 2 times against 0.1 M NaCl and 3 times against d-H$_2$O, respectively. Products were freeze dried to obtain dry N-carboxy derivatized chitosan powders/ lyophilizates.
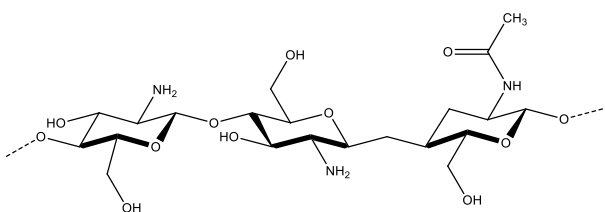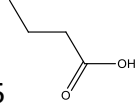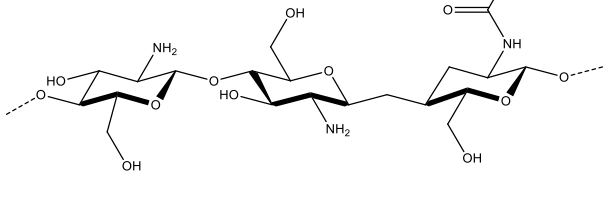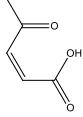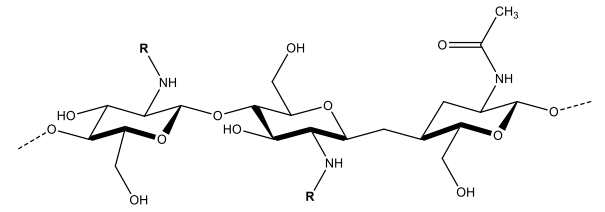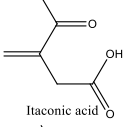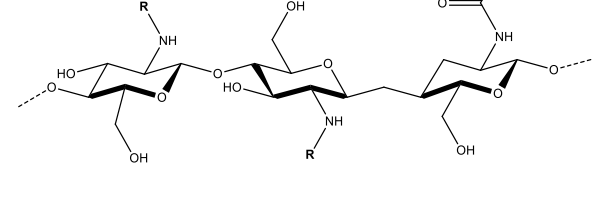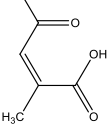
2.2.2 Verification of FC reactions

In order to assess the success of N-carboxy derivatization, Chitosan derivatives prepared by freeze concetration were methylated through the procedure [54]: 1 g of chitosan was suspended in a mixture containing 40 mL N-methyl-2-pyrrolidone, 5.5 mL of 15 wt.% NaOH, 5.7 mL of ^{13}C-iodomethane and 2.4 g of NaI. Reaction was carried out at room temperature by constantly stirring for 24 h. Solutions were ion-exchanged using a dialysis membrane (MW cutoff=3.5K) against d-H$_2$O, 0.1 M NaCl and d-H$_2$O, respectively. The products were then freeze-dried to obtain methylated chitosan lyophilizates.

Table 1 Summary of all sample names, reactants used and reaction temperatures for reactions.

Sample Name	Reactant (10%, 1:1)	Reaction Temperature (°C)
A-5	Acrylic acid	-5
A50	Acrylic acid	50
C-5	Citraconic acid	-5
C50	Citraconic acid	50
M-5	Maleic acid	-5
M50	Maleic acid	50
I-5	Itaconic acid	-5
I50	Itaconic acid	50

Table 2 Michael addition reaction and reactants used

2.2.3 Ninhydrin Test and Color Quantification

Cd-ninhydrin test [55] was employed to quantify and to compare the solubilities of Chitosan derivatives with native form. This test is a direct method to detect the amine residues resulting with a red and pale orange/yellow color for primary and secondary amines, respectively. 1mg/mL solutions of Chitosan samples were dropped on a Whatmann 3MM paper; freshly prepared Cd-ninhydrin reagent was sprayed on sample spots and air-dried. Cd-ninhydrin test yielded a range of colors from red to yellow allowing us to quantify the amount of primary and secondary amines depending on the red color intensities.

A color intensity analysis method similar to Western blot quantification described by Gassmann *et. al.* [56] was employed to assess ninhydrin yields. Freshly prepared Cd-ninhydrin sprayed Whatman papers prepared as described above were scanned and processed with ImageJ software [57]. Once the background color was subtracted, the color scheme of the images was inverted to better quantify higher concentration samples. By this means, higher concentration bands, which appeared dark on the image, were assured to have high numerical values upon measuring. The mean color intensities were then measured by selecting the Cd-ninhydrin added bands.

2.3 Results

2.3.1 Evidence Supporting Michael Type Addition in Frozen Solutions

Figure 3 (top) shows the attenuated total reflectance (ATR) FTIR spectrum of native chitosan. The one band at 1151 cm^{-1} and two bands in the range of 1069–1028 cm^{-1} have been attributed, respectively, to asymmetric C-O vibrations resulting from deacetylation and C-OH and C-O-C vibrations of the β-(1-4)-linked D-glucosamine (deacetylated unit) and N-acetyl-D-glucosamine (acetylated unit) rings. Moreover, the absorption bands at 1381 and 1422 cm^{-1} have been attributed to -CH2 and -CH bending vibrations, respectively. Overlapping peaks within the range of 1589-1650 cm^{-1} correspond to the bending mode of primary amino groups and carbonyl stretching of native N-acetamido groups, respectively. The composite absorbance band in the region of about 2872-2920 cm^{-1} corresponded to symmetric and asymmetric stretchings of the aliphatic -CH2 and -CH3 groups. The broad peak centered on 3362 cm^{-1} originated from H-bonded hydroxyl and amino groups.
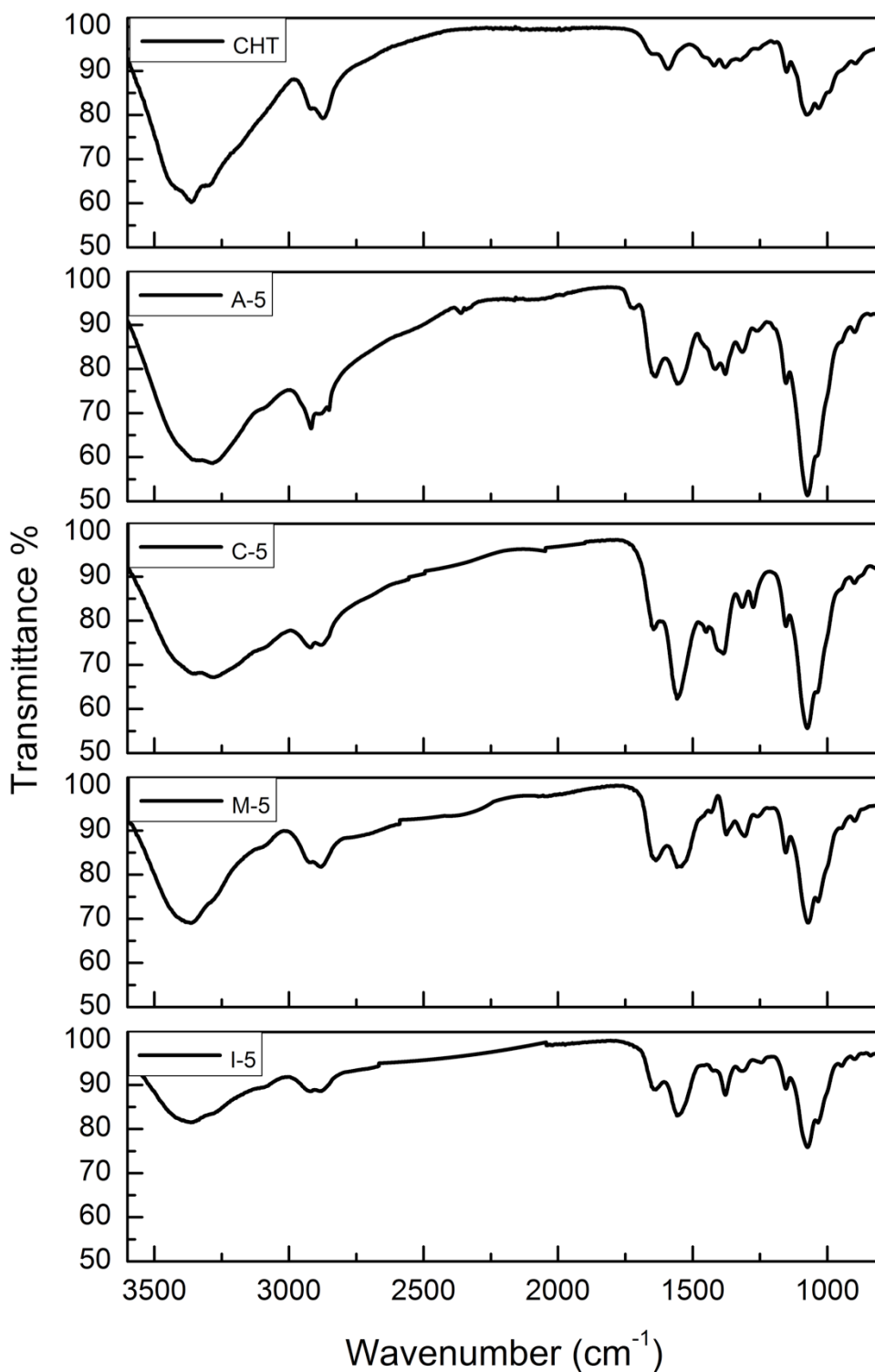
Figure 3 FTIR spectra of native chitosan (CHT) and Michael adducts with acrylic acid (A-5), citraconic acid (C-5), maleic acid (M-5), and itaconic acid (I-5).

Once incubated with acrylic, citraconic, maleic, and itaconic acids under freeze concentrated conditions, chitosan displayed additional bands in the IR spectra (Figure 3). The primary amine N-H bending signal at 1589 cm^{-1} in native chitosan was shrouded and unavailable for assessment, but a new band appearing around 1550 cm^{-1} lay in the region corresponding to the N–H bending of secondary amines.

Figure 4 and 5 shows ^{1}H-NMR spectra of native, FC-derivatized and 50 ^{0}C-derivatized chitosans. Specific to chitosan, all the spectra exhibited a chemical shift around 2.0-ppm; corresponds to N-acetamido hydrogens of chitosan backbone. In addition, the broad peaks centered on 5.0 ppm were attributed to glucosamine and N-acetyl glucosamine rings of chitosan. On the other hand, ^{1}H-NMR study of native and N-carboxy dervatized chitosans showed several fundamental differences. For instance, the newly appeared chemical shift around 2.5-3.0 ppm aroused from N-alkylation of glucosamine rings; while chemical shifts around 3.6-4.1 ppm were due to mono and dimethylation in N- alkyl chitosan. These peaks stood as a solid proof of Michael addition. It should be mentioned that all ^{1}H-NMR spectra contains some sharp peaks due to solvents used in measurement.
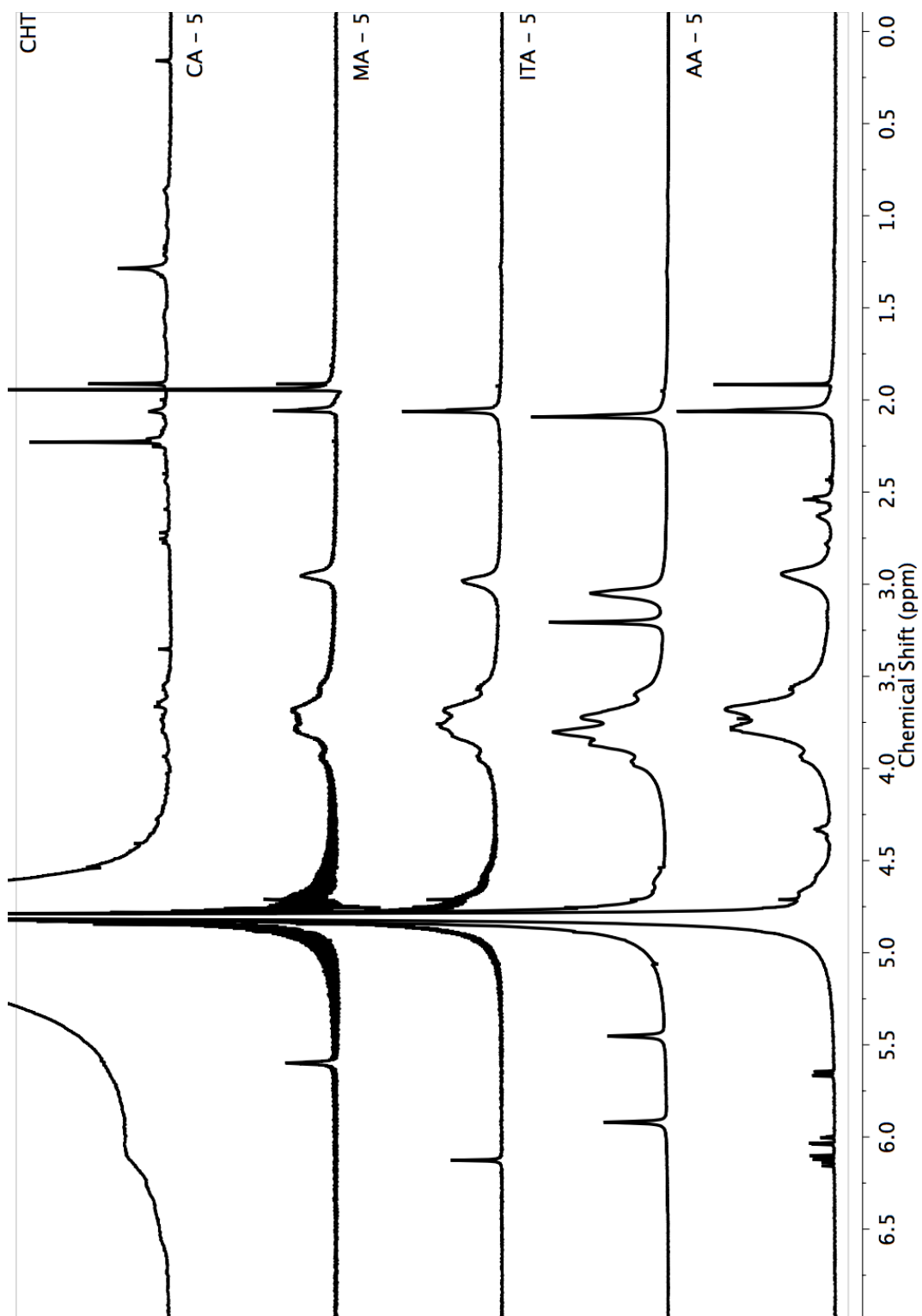
Figure 4 ^{1}H-NMR spectra of native (top) and FC-derivatized chitosan products.
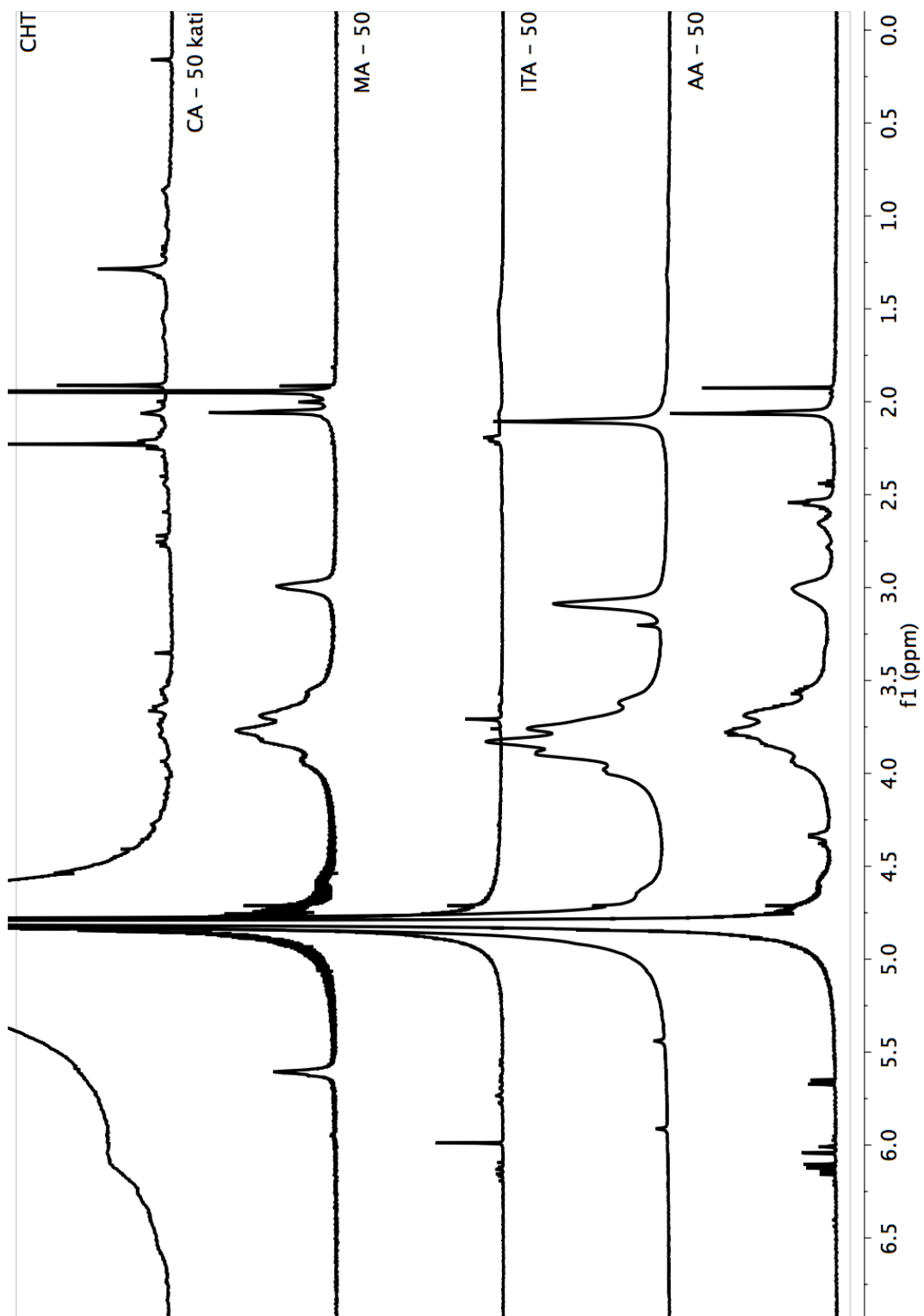
Figure 5 ^{1}H-NMR spectra of native (top) and 50 [0]C-derivatized chitosan products.

For ^{13}C-NMR study, equal amounts of freeze-concentration treated and native chitosan were alkylated using ^{13}C-labeled iodomethane under identical homogenous phase conditions. The samples were purified identically and subjected to ^{13}C-NMR analysis. Both showed three bands around 30, 41 and 52 ppm. The respective values reflected mono-, di- and trimethylation of primary amines by 13C-iodomethane [58] (Figure 6). More importantly, however, the two spectra differed substantially in their signal-to-noise (S/N) ratio. Given that long interpulse delays were applied, and equivalent amounts of sample were dissolved in the NMR tube, the only factor remaining, which could explain the approximate 3-fold loss of S/N in the freeze-concentration treated sample, was a substantial drop in the total methyl group signal. Hence, the availability of reactive amino groups, for instance primary amines, must have been limited in the freeze-concentrated sample, indicating blocked, deactivated or otherwise sterically challenged nitrogen nucleophiles. While it is true that secondary amines are also reactive towards iodomethane, reactions yielding N-^{13}C-methylated and N,N-^{13}C-dimethylated Michael type adducts would give rise to a relative loss of signal at 30 ppm, which was not the case. Moreover, Michael type adducts between chitosan and olefinic acids would presumably afford exceptionally unreactive secondary amines in the sense that a carboxyethyl inner ammonium salt would have been formed. For stereoelectronic reasons, such a β-amino acid derivative would likely twart the ability of the new secondary amine center to engage in reaction with iodomethane. Firstly, the nitrogen atom would acquire a near-persistent positive charge. Secondly, it would reside near a bulky carboxyl group.
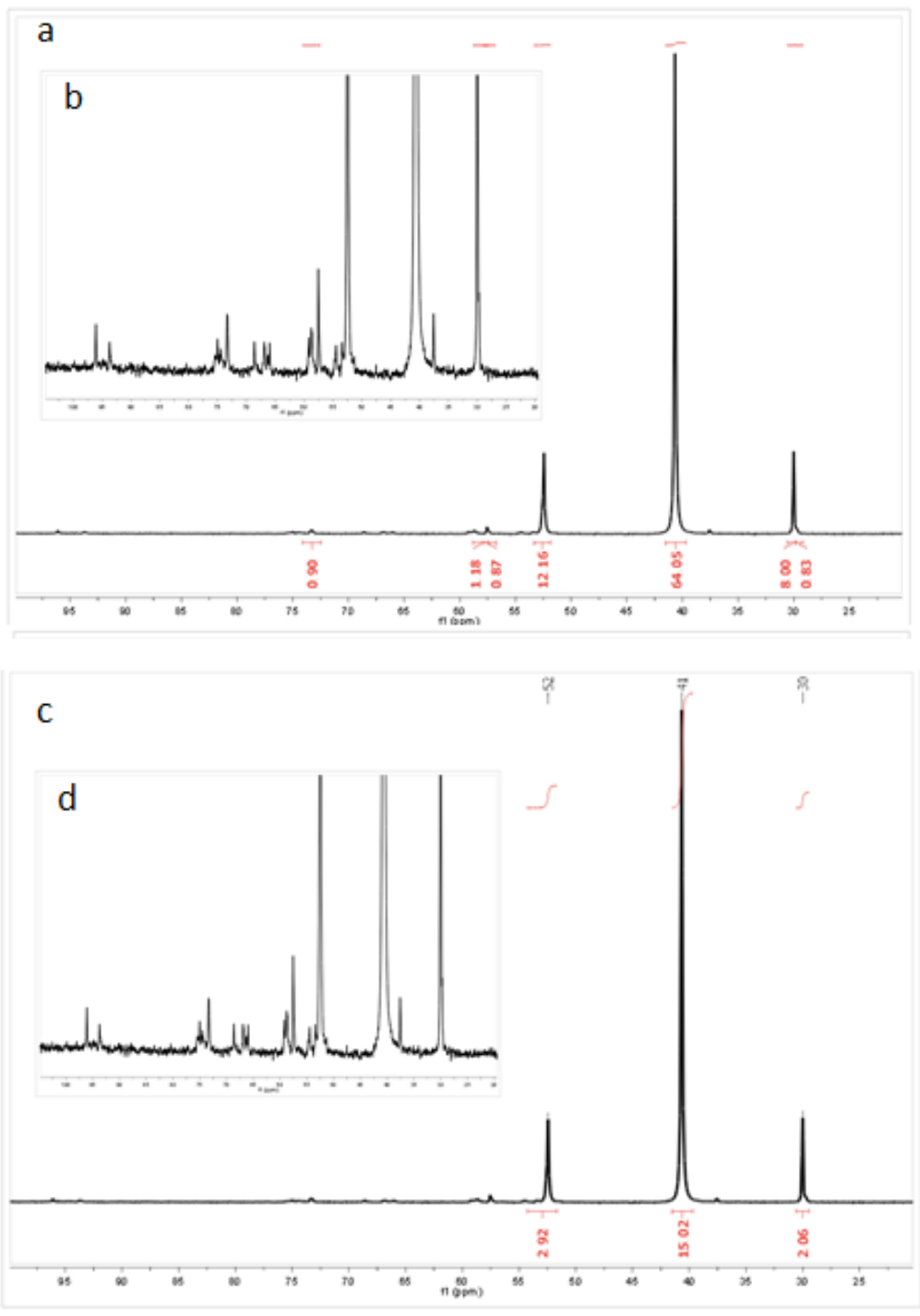
Figure 6 ^{13}C-NMR spectrum of ^{13}C-methylated N-carboxyethyl chitosan (a), overall view (b); ^{13}C-NMR spectrum of ^{13}C-methylated native chitosan (c), overall view (d).
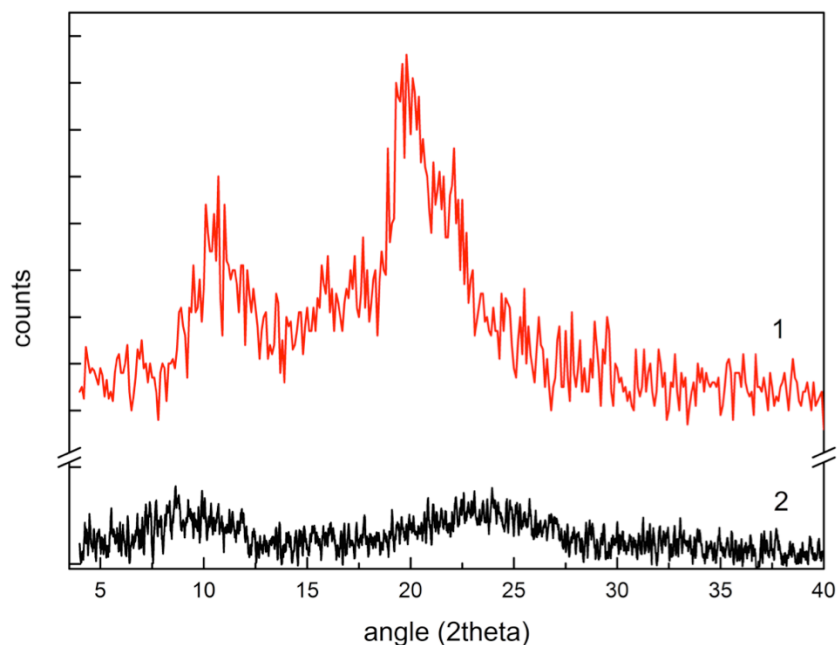
Figure 7 X-Ray diffraction (XRD) patterns of native (1) and FC-treated chitosan (2).

Shown in Figure 7; the X-Ray diffraction pattern of native chitosan showed two broad peaks with 2θ values centered at 10.7° and 19.8°. Chitosan incubated together with acrylic acid under freeze concentrated conditions (2) displayed the same peaks at a much reduced intensity, whereas chitosan incubated without reagent or with the near-isosteric propionic acid in place of acrylic acid (data not presented) showed no loss of signal. Given that all measurements reflected the same initial mass of chitosan, a comparative loss of overall crystallinity was apparent in proceeding from native to freeze concentrated chitosan, but only when acrylic acid was present in the medium.

Figure 8 highlights the Cd-ninhydrin color yields of equal amounts of native and freeze-concentration derivatized chitosan spotted onto chromatography paper. All test and control samples clearly lied within the linear range of the standard curve (inset). The results showed a significant loss of color yield in freeze-concentration treated compared to native chitosan. As the intrinsic color yield of secondary amines is much lower than primary amines, and as there were

no other foreseeable sources of artifacts, the observable color yields reflected reaction with only primary aliphatic amines. Assuming that all derivatizable amino groups were accessible to ninhydrin reagent under the staining conditions, it followed to reason that freeze-concentration treated chitosan samples had experienced an approximate 2/3 loss of primary amino groups following their incubation in the presence of any of the olefinic acids (A-5, C-5, M-5 and I-5). This finding was also noteworthy in the sense that it correlated well with the 13C-NMR analyses, which implied an approximate 3-fold reduction of methylatable amino groups following treatment with acrylic acid under freeze concentration conditions. To ascertain if any global changes to the chitosan structure under freeze concentration conditions might have inadvertently influenced the color yield, native chitosan was also incubated under freeze concentration conditions and worked-up using propionic acid in place of acrylic acid. The freeze concentration negative control afforded a color yield similar to native chitosan (not shown). Chitosan treated with acrylic acid at 50 °C (A50) also showed a drop in amino group content.

While chitosan dissolution might appear to be a problem of intrinsic solubility, it should be emphasized that chemical treatment had not been employed herein to improve the interaction between chitosan and water. Chitosan is rich in H-bonding groups, so the dissolution of isolated chitosan molecules in water presumably should be thermodynamically spontaneous at all pH values. Rather, chemical treatment was used herein as a means to limit chitosan-chitosan interactions, thus weakening other favorable competing pathways such as crystallization. This claim was supported by XRD, which showed a notable loss of overall crystallinity, and visual inspection, which showed a dramatic loss of solution viscosity, indicating less inter-chain interaction. When considering the highly polar chemical composition of chitosan, it would stand to reason that native chitosan does not dissolve in alkaline media for kinetic as opposed to thermodynamic reasons. Indeed, native and Michael type adducts of chitosan would be expected to differ little in terms of polar group content. Thus, from a Gibbs energy viewpoints, any changes experienced during treatment with acrylic acid under freeze concentrated conditions had likely served to reduce kinetic barriers leading to dissolution. While it is true that secondary amines can normally H-bond via donor and acceptor modes, a N-carboxyethyl derivative, which presumably formed after freeze concentration treatment, likely existed as the inner salt. Operating

under such a scenario, the substantial steric bulk about nitrogen and the zwitterionic character of the N-carboxylethyl moiety implied a looser-packed structure in which the secondary amino derivatives in chitosan could not effectively H-bond. While likely improving the kinetics of dissolution, it is not known to what extent these stereoelectronic changes had notably altered the absolute solubility of freeze-concentration-treated versus native chitosan. Absolute solubility clearly depends on derivatization, but as more detailed solubility tests were not conducted, further insight was unavailable.
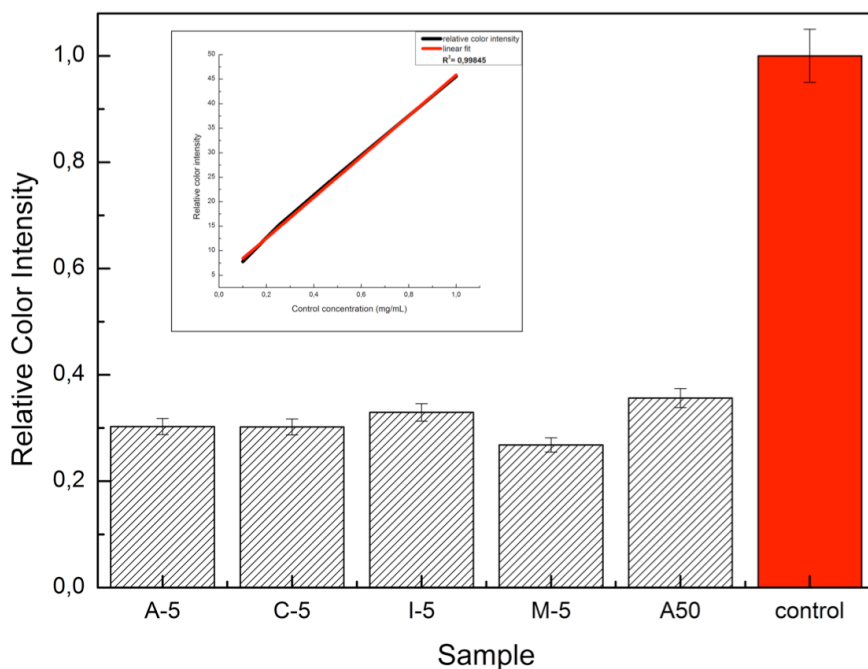
Figure 8 Ninhydrin color yields of freeze concentration treated products (A-5, C-5, I-5, M-5), a 50 °C control (A50), and untreated native chitosan (Control) (1 mg/mL), with relative intensities being reported (Inset – Standard curve utilizing native chitosan dissolved in acetic acid (10%) in the concentration range 0-1 mg/mL). The volume used to spot samples onto paper was fixed (200 µL).

Figures 9 and 10 illustrate the SEM imagery analysis of native and freeze concentrated treated, 50 °C treated chitosan, respectively. Native chitosan displayed smooth surfaces with no fibrillar structure, whereas freeze concentration treated chitosan displayed a porous structure comprising of clustered microporous fibrils. Compared to chitosan treated with acrylic acid at 50 °C, the freeze concentration treated chitosan displayed finer fibril structures and a notably improved, regular pore structure. As all samples had been dialyzed at the onset of the work-up procedure, and the perfectly soluble solutions obtained were freeze-dried, it followed to conclude that the observed morphological differences had manifested only during the lyophilization process. Porosity and pore structure following lyophilization is known to be a function of ice crystal templating during sample freezing at the onset of lyophilization; as the pre- lyophilization water and salt content of each sample was equivalent, the only distinguishing feature remaining could be chitosan. It necessarily followed that physico-chemical changes had occurred in chitosan following incubation with acrylic acid, and these distinguishing changes had influenced the formation of ice at the onset and possibly over the course of freeze-drying. Assuming this cause-and-effect relation applied herein, it also followed to reason that the physicochemical traits of freeze concentration and 50 °C-treated chitosans differed substantially. This claim was supported by the different ninhydrin color yields of the two samples (Figure 8; A-5 vs. A50), indicative of physicochemical difference.
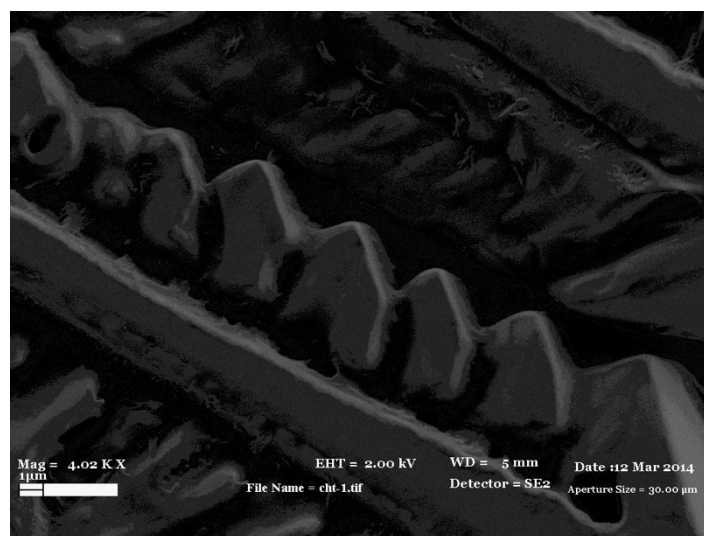
Figure 9 SEM image of native chitosan
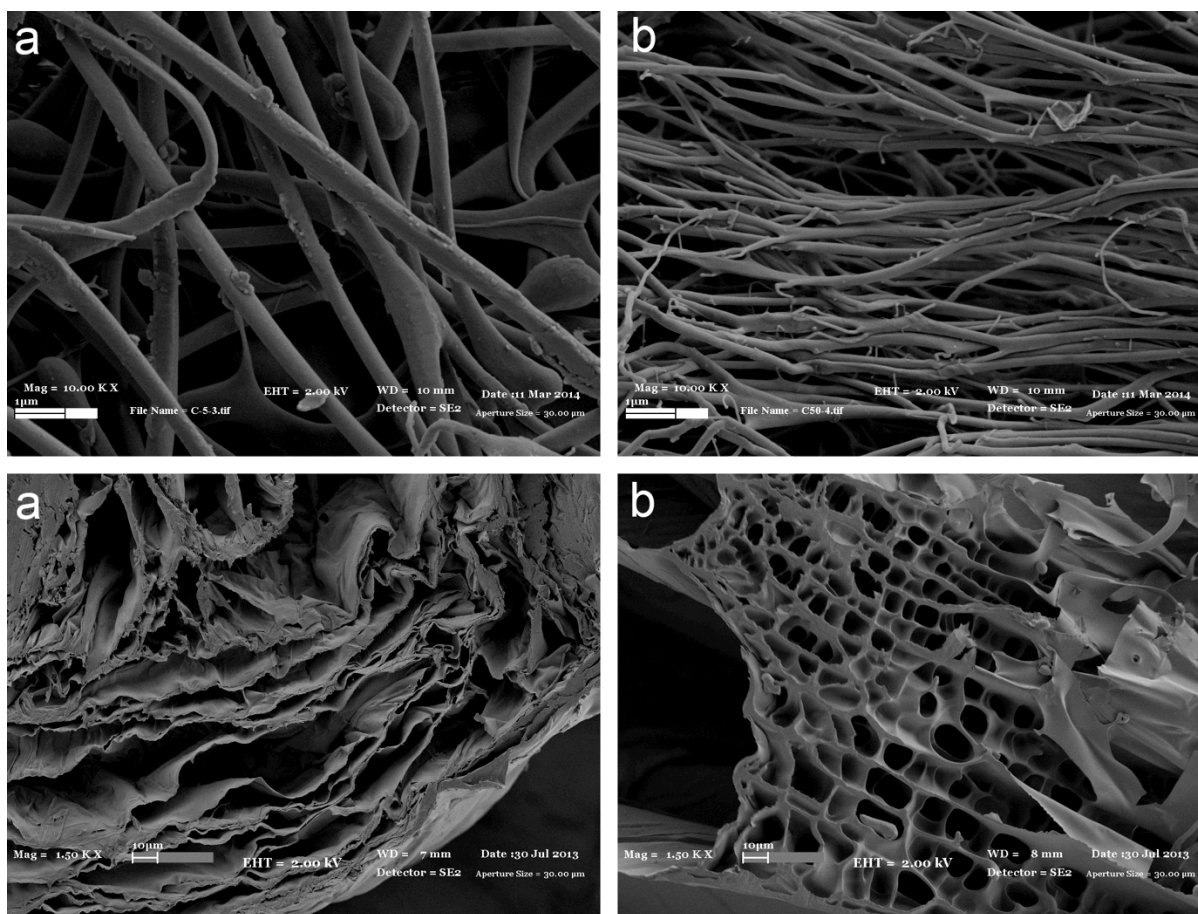
Figure 10 SEM micrographs of (a) 50 °C and (b) freeze concentration derivatized products at several magnifications.

Figure 11 demonstrates thermogravimetric analysis curves of untreated chitosan (a), and Michael addition products obtained in 50 °C (b) and -5 °C (c). Thermogravimetric curves were recorded between 25-500 °C with a heating rate of 10 °C/min. All three thermal curves demonstrate a weight loss between 25-140 °C, which can be attributed to initial dehydration of polymers. Comparing untreated chitosan to Michael adducts, the thermal stability of chitosan was slightly decreased upon modification. This can be understood from the difference in thermogravimetric curves, i.e. untreated chitosan decomposes around 295 °C whereas N-carboxyethyl derivatives decompose around 239 °C. The decrease can be attributed to weakened secondary interactions upon modification. On the other hand, there is no difference observed between Michael addition

products prepared in 50 °C and FC. This shows that freeze concentration does not lower thermal stability.
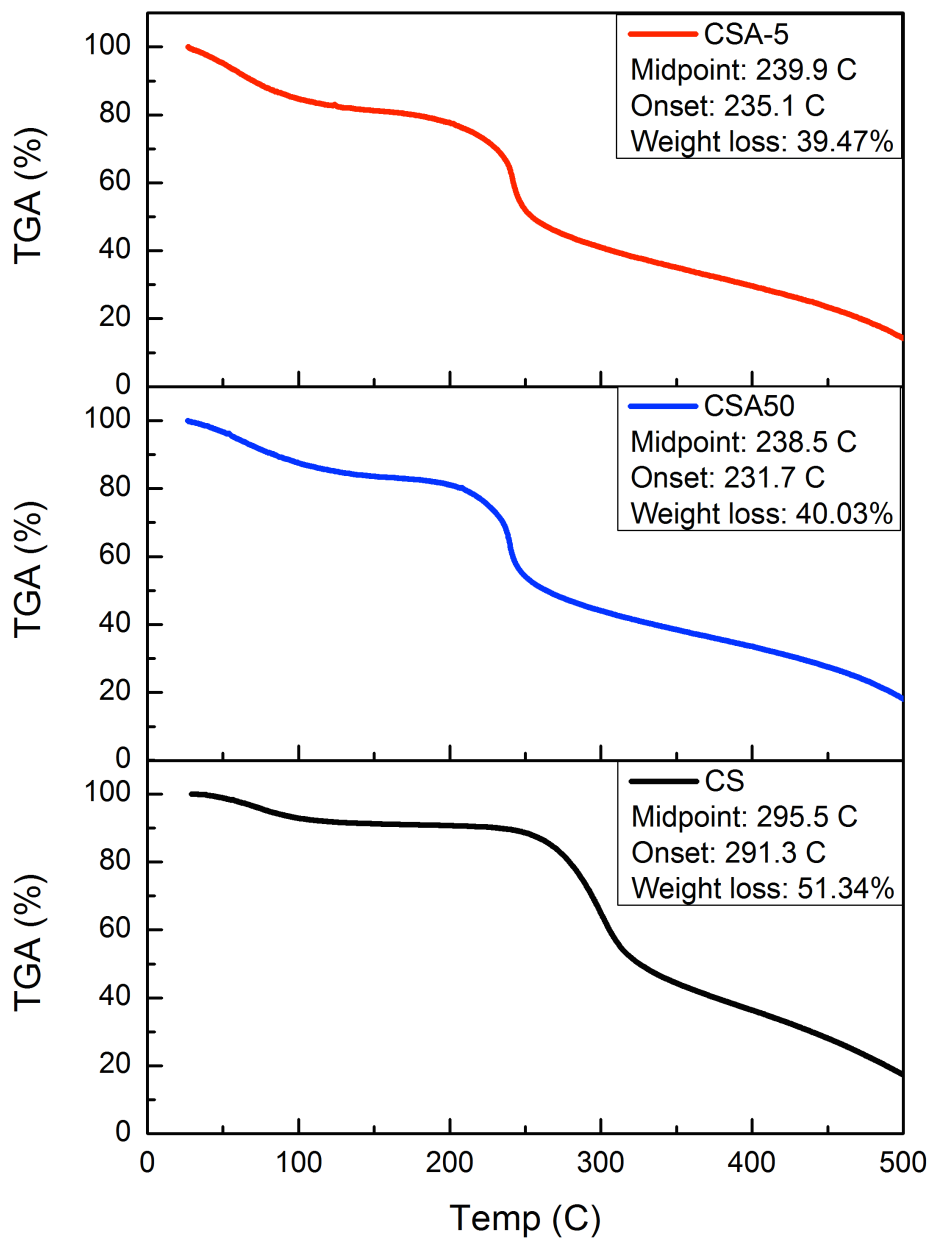
Figure 11 TGA curves of untreated chitosan (black), Michael addition derivatives in 50 °C (blue) and freeze-concentration (red) of chitosan with a heating rate of 10 °C/min. The calculated total weight loss were placed in top-right.

2.4 Discussion

Compared to the N-acetamido internal reference of untreated chitosan at about 1650 cm^{-1}, in FTIR spectra of N-carboxyethyl derivatives, the emergence of higher frequency, non-amide carbonyl stretching bands in freeze-concentrated chitosan samples supported the formation of Michael adducts. The possibility of wrongly assigning carbonyl bands due to the inadvertent presence of trace salts formed between amino group and olefinic acid was readily discounted in view of the numerous dialyses performed, the ease of diffusion of acid groups away from the heavily hydrated samples, the presence of excess sodium chloride in the dialysis medium to prompt ion exchange, and the propensity of weak salt-acid systems to dissociate and volatilize during subsequent lyophilization. In any case, bands consistent with primary amino-olefinic carboxylate salts would be expected to the right of 1640 cm^{-1}, which was not the case herein. Following IR analysis, ^{13}C-NMR was used to definitively confirm the formation of Michael type adducts during freeze concentration. In spite of its diagnostic strengths, ^{13}C-NMR appears to have escaped any attention in analyzing chitosan. While low sensitivity may have discouraged previous attempts, this study clearly affirmed the utility of ^{13}C-NMR, and implied its continued use on chitosan-based systems.

An increased amorphous content after the freeze-concentration treatment of chitosan with acrylic acid confirmed a lost propensity to crystallize. In keeping with this argument, groups mediating intermolecular packing of chitosan in solution appeared to have undergone stereoelectronic changes, which disrupted the ability of individual chitosan chains to regularly re-pack. Such a scenario could have reflected the formation of Michael type 1,4-adducts, as lost primary amino groups and newly introduced carboxyethyl moieties along the backbone would heterogenize individual chitosan molecules, reduce H-bonding possibilities, loosen the packing structure, and thereby prompt a loss of overall crystallinity. The possibility of having undergone chemical change was further supported given the established reactivity between primary amines and α,β-unsaturated carbonyl groups, and the fact that a control experiment substituting acrylic by the near-isosteric propionic acid had not altered the post-treatment crystallinity of chitosan.

In summary, various self-consistent physical and chemical analyses discussed above indicated that the Michael type addition products between chitosan and unsaturated acids were kinetically permitted under freeze concentrated conditions. This argument was further supported in view of the established ability of amino groups to add across a,b-unsaturated carbonyl groups, and the notion that high concentrations and reduced entropy per unit time can off-set the cold temperature effect. In light of the great importance of biomaterials, it is hoped that this initial study will attest to the merit and potential of derivatizing protein and other intrinsically labile biological substances under freeze-concentrated conditions, particularly materials, which are deemed thermally unstable.

The visual inspections of solubility also showed remarkable changes following freeze concentration treatment (Figure 12). As solubility and speed of dissolution varies according to the chitin source and degree of N-deacetylation, all solubility tests were performed using chitosan from the same stock. Amongst the noteworthy findings, native chitosan (10 mg/mL) dissolved only within the pH range of 1.0-5.0 whereas freeze-concentration treated chitosan dissolved throughout the pH range of 1.0-10.0. Solubility differences visually highlights changes in reconstitutability of lyophilized chitosan samples. Each sample was previously treated under freeze concentration conditions with either acrylic or propionic acids, and worked-up following incubation. Chitosan treated with acrylic acid formed clear solutions at pH 7 and 10, whereas chitosan treated with propionic acid remained in suspension. In passing, the same images were obtained following a year's incubation at room temperature under non-aseptic conditions, attesting to the long-term stability of chitosan and its derivatives.

The analyses were noteworthy in view that all spectroscopic and colorimetric changes had supported one another and the theme of chemical transformation under freeze concentrated conditions. Physical analyses such as XRD, and dissolution tests provided vivid evidence that the network structure of chitosan had been substantially altered. Tests identifying aspects of chemical change, such as ninhydrin yields, NMR, and FTIR, highlighted evidence that samples differed in composition following incubation with olefinic acids under freeze concentrated conditions.
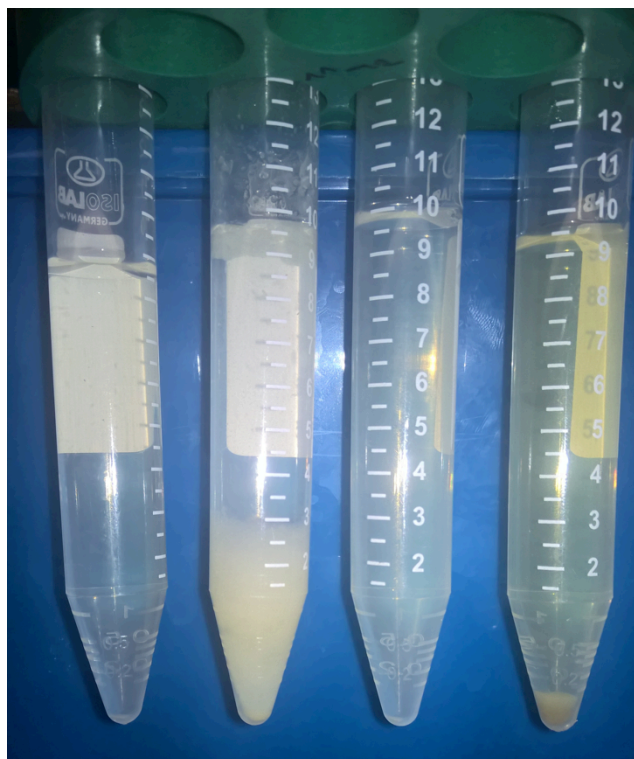
Figure 12 Dissolution traits of chitosan (100mg) incubated with aqueous acrylic or propionic acid (10%) under FC conditions (-5°C, 16h) followed by dialysis and lyophilization. Reconstitution conditions (right to left): Acrylic acid-treated, pH 7; propionic acid-treated, pH 7; acrylic acid-treated, pH 10; and propionic acid treated, pH 10.

Also worthy of emphasis is that control solutions, identically prepared but left to incubate at room temperature for the same period, showed no changes of amino group content. A last control, namely, aqueous chitosan frozen together with unreactive propionic acid in place of acrylic acid, also showed no change of amino group content compared to untreated native chitosan.

2.5 Conclusions

This study aimed to improve the dissolution traits and working pH range of chitosan by using a unique reaction technique. So far, several synthetic routes have been developed to obtain chemically modified soluble chitosan derivatives, with varied results. A seldom-used and radically different chemical approach was adopted herein to modify the stereoelectronic attributes of accessible amino groups, thereby disrupting the regular network structure of chitosan. Various

analyses suggested that chitosan modification took place under freeze concentrated conditions. Overall, the facilitated dissolution and broadened pH solubility range of derivatized chitosan was consistent with a decrease of chitosan-chitosan interactions, and associated kinetic barriers to dissolution. From a physicochemical viewpoint, the reduction of crystallinity was attributed to stereoelectronic changes following the replacement of approximately two thirds of all primary amines by secondary amines. While not directly observed, heterogeneities amongst individual chitosan molecules necessarily existed following derivatization. Such heterogeneity also would have discouraged chitosan-chitosan re-association as well as high kinetic barriers to dissolution. On the other hand, this work is novel in the sense that Michael adducts of chitosan and ester or amides must be processed further to re-generate the free carboxylic acid. In our work, we obtained the acid directly under mild conditions different than esters and, to our knowledge; this is the first attempt to have the acid directly under free conditions.

This study is also unique in that it employs the concept of freeze concentration in order to chemically transform macromolecules and tailor their traits. In that sense, the method herein showed substantial potential, affording chitosan derivatives with a finer structure and more regular morphology compared to conventional reactions carried out at higher temperatures. A logical extension of the freeze concentration method could be to facilitate the chemical functionalization and tailoring of biomolecules, which are intrinsically prone to thermal degradation, particularly in aqueous media.

CHAPTER 3 Molecularly Imprinted Chitosan-Graphene Based Nanosensor for Aqueous Phase Detection of Nitroaromatics

3.1 Introduction

Chemical sensors have found considerable applications in fast detection of explosives for mining, environmental, forensic and criminal research and in improvement of explosives production [59, 60]. There are several approaches to detection of nitroaromatic compounds from low precision indirect determination of metal covered explosives to high sensitive spectroscopic determination of trace amounts. Low precision methods are useful to detect traditional landmines and arms, but are inadequate in further applications such as airport scanning and flight safety. On the other hand, high sensitive methods require sophisticated instrumentation including gas chromatography-mass spectroscopy [61], Raman spectroscopy [62], energy dispersive X-Ray diffraction [63] and cyclic voltammetry [64], therefore incompatible with field applications. Along with its sensitivity in pico- to nanogram levels, ion mobility spectroscopy is a frequently used technique in airport safety with high cost, requiring frequent calibration and may give false positives liable to operator [65].

Considering the ecological effects along with determination and location nitroaromatics [65, 66], analyte interferences during sampling from water and soil poses a problem for detection systems. As a result, determination of trace amounts of chemicals in soil samples is limited to their volatile components and/or side products of material [67]. Polymeric absorbers are employed to help increase the signal strength since the vapor pressures of explosives are relatively low. In these systems, volatile component is condensed on detection system and physically/chemically adsorbed on the polymeric material's pores. Therefore, vapor pressure of volatile component is the dominant factor in determining response time of the sensor, while detection limit requires volatile component amount enough to be detected by the system. Along with United States Environmental Protection agency (USEPA) criteria for environmental health and safety [68], taking difficult sampling conditions, and necessity of bulk amount of analyte of vapor pressure-based methods into consideration, it is of utmost importance to develop high-sensitivity methods

to detect trace amount of nitroaromatics. Although the toxicity tests resulted in low toxicity values for nitroaromatic compound of nitrotriazolone (NTO), the lowest observed adverse effect level values of 2,4,6-trinitrotoluene (TNT) and NTO are 0.5 mg/kg/day and 30mg/kg/day, respectively [69]. Along with USEPA criteria for explosives [70], taking environmental factors into consideration, efficient methods are required to detect these type of chemicals.

Nano-scale systems provide numerous alternatives to develop detection systems with the limits mentioned above. Here, the prefix "nano-" defines systems with high sensitivities that they are able to do detection below the limits of macro-sized materials. Therefore nanosensors enhance the observability of chemical and physical properties. In addition, well-developed fabrication techniques enable smaller fabrication sizes and an improvement in signal-transforming performances was observed as the fabrication size becomes smaller [71]. There are various nano-sized detection elements/platforms available in the literature including quantum dots [72], nano-wires [73], and nanotubes [74].

Utilization of graphene in nanosensor systems in nitroaromatics detection was first reported in 2010 [75]. As a 2D carbon material, graphene has superior electrical properties [76] arising from effective π-π interactions and homogenous distribution of electrochemically active sites [77, 78]. In addition to this, extraordinary electronic band structure enables graphene to behave as a zero-band gap semi-conductor [79] and the considerable surface area allows adsorbent materials to significantly change its electrical properties by altering carrier density. The high sensitivity of graphene also arises from low electrical signal noise due to its 2D crystal network structure [80]. All those findings indicate graphene to be available to respond electrically, even in very low concentrations of analyte and therefore suitable for nanosensor applications.

Detection of nitroaromatics using graphene was first carried out by coating graphene on a glassy electrode [81], and followed by many others [77, 81, 82]. Majority of the studies employing graphene as transistor were based on electrochemical measurements. Although fabrication and measurement technique is relatively simple, selectivity is rather limited in electrochemical systems [71].

Several polymeric systems were employed in detection of nitroaromatics using physical, structural and electronic interactions between analyte and polymeric material [83, 84]. Primary concern in developing new sensors is to collect adequate amount of recognition/binding element in the sensor probe. In this aspect, molecularly imprinted polymers possess various advantages such as varying selectivity and low cost. General approach in sensor design is to utilize sensor probes with high specifity against analyte. Yet, in ecological samples, analyte is notably in very low concentrations and mostly surrounded by a matrix composes of similar molecules. Therefore, even systems employing high selectivity enzymes as sensor probes are prone to cross-reactivity and false positives [85]. As a solution to this, molecularly imprinted polymers offer specific and selective cavities of analyte within the polymer surface stabilized by inter-molecular crosslinking thus ensure several physical or chemical interactions with analyte [86-88]. In addition, molecularly imprinted polymers are also superior to traditional polymers in terms of high thermal, chemical and mechanical stability [89], therefore it is considerably reasonable to employ molecularly imprinted polymers as sensor probes. As a natural poly amino saccharide with available amino and hydroxyl functional groups chitosan is convenient to crosslinking, hence molecular imprinting. In addition, crosslinked chitosan act as supporting matrix due its superior film forming ability [90] and increased mechanical properties arising from crosslinking [91]. Vast amount of available amino and hydroxyl groups also provide strong secondary interactions with nitroaromatics and thus ensure adsorption. These advantages of chitosan make it a promising candidate for nanosensor applications for nitroaromatics [92] with no further need of additional film component.

An approach to increase the selectivity in nanosensors is to use hybrid systems and thus to obtain orthogonal or enhanced signal by gathering different sensing mechanisms [91]. Hybrid systems comprising graphene are usually composed of a graphene layer and a polymer. Recently, several examples of such systems used for explosive detection are found in literature [93-95] but they mostly target TNT and use sophisticated instrumentation for signal transduction.

Molecular imprinting creates binding sites in polymeric film surface that is specific to template molecules. In a standard molecular imprinting process, template molecules are introduced to polymer during crosslinking. In the meantime, crosslinked polymer assembles around template

molecule to create specific binding sites. These binding sites interact with the analyte both through lock-key mechanism and via secondary interactions. This way, highly selective polymeric films/matrices are obtained. When exposed to the analyte, polymeric film reversibly adsorbs analyte molecules. This adsorption results in increasing the charge of the polymeric film, thus altering the resistance of bottom layer (graphene). The sensing mechanism via molecular imprinting is explained in Figure 13.

The purpose of this study is to develop a hybrid nanosensor to detect NTO by adsorbing nitroaromatic compound on molecularly imprinted chitosan film and to determine the amount of adsorbed species via the change in resistivity of monolayer graphene sheet. To do this, monolayer graphene was transferred onto SiO_2 substrate, and coated with molecularly imprinted polymer film. Metallic electrodes were embedded into substrate by lithography prior to graphene transfer. Here, NTO was chosen as the target molecule since it is a new generation insensitive explosive, thus a possible replacement for TNT. Selectivity and sensitivity of the fabricated nanosensor was tested against analyte and a chemical compound that is similar to NTO in molecular structure (histidine). Real sample measurements were also carried out to test the effect of other possible interfering chemicals present in water and soil samples. Although it has been widely used in nitroaromatics detection as film substrate, molecularly imprinted chitosan was used as a direct sensor probe for the first time without needing any further component to increase the signal strength or to ensure interaction. In addition, a unique micro fabrication technique was applied where the electrodes to measure the change in sheet resistance of graphene due to molecularly imprinted polymer-analyte attractions were embedded in sensor substrate. To our knowledge this is the first time where such a technique has been used, unlike other methods where electrodes were usually fabricated on graphene for transfer length measurements (TLM). By this process, contamination of graphene or other interfering species during fabrication and measurements were eliminated.
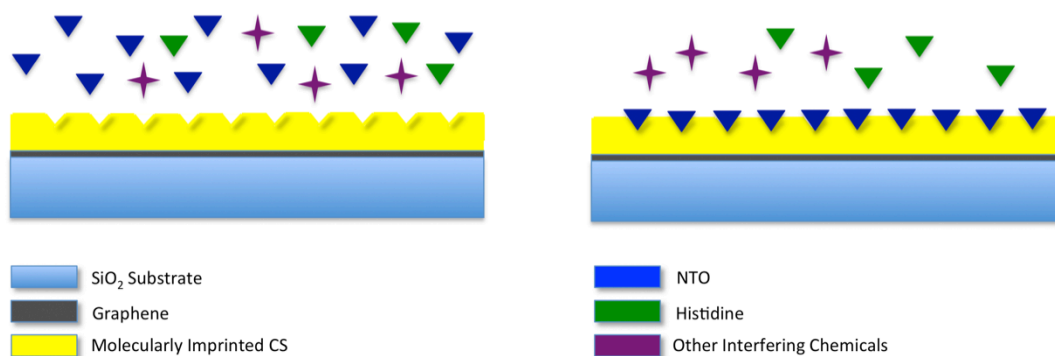
Figure 13 Schematic representation of molecular imprinting and recognition mechanism employed in nanosensor.

3.2 Materials & Methods

3.2.1 Preparation of Molecularly Imprinted Chitosan Films

Molecular imprinting was carried out to ensure non-covalent interactions between polymeric film and NTO molecules. For this purpose, acetic acid solution (1%) of chitosan (CS) and NTO was introduced with glutaraldehyde (GA) and stirred for 5 minutes. The mixture was then spin-coated onto a CVD graphene substrate. As a negative control, non-imprinted films were prepared in the absence of NTO. Amount of NTO and glutaraldehyde added were explained in Table 3. Resulting films were characterized by ATR-FTIR spectroscopy. Swelling kinetics of the films was studied in detail along with its effect on NTO adsorption capacity.

3.2.2 ATR-FTIR Spectroscopy

ATR-FTIR spectra of crosslinked films were collected on a Bruker Equinox 55 ATR-FTIR spectrometer from 550 to 4000 cm^{-1}, with a resolution of 0.5 cm^{-1}. A total of 32 scans were gathered and baseline-corrected.

3.2.3 UV-Vis Spectroscopy

Capacities of NTO adsorption of molecularly imprinted films were measured in terms of the decrease in visible light absorption of NTO solutions exposed to molecularly imprinted chitosan films, compared to that of non-imprinted films. Spectra were collected using Schimadzu UV3600

Plus Ultraviolet, visible and near-IR spectrometer. Selectivity studies, along with desorption kinetics were carried out using UV-Visible spectroscopy.

Table 3 Summary of samples, crosslinker agent and amounts of NTO used in imprinting

Code	NTO/CS ratio (m/m)	CS/GA ratio (m/V)
CSNIP1	-	0.02
CSNIP2	-	0.04
CSNIP3	-	0.08
CSNIP4	-	0.16
CSNTO-N1	0.20	0.02
CSNTO-N2	0.40	0.02
CSNTO-N3	0.60	0.02
CSNTO-N4	0.80	0.02
CSNTO1	0.40	0.02
CSNTO2	0.40	0.04
CSNTO3	0.40	0.08
CSNTO4	0.40	0.16

3.2.4 Fabrication of Metallic Contact Lines

Micro fabrication of nanosensor starts with development of metallic contact lines. For this purpose we developed two strategies, one of them involves a hard mask of TLM lines, and the other involves photolithography with soft mask. In the first method, an aluminum mask with TLM lines prepared beforehand was placed on Si/SiO_2 substrate and substrate was etched. Gold electrodes were then placed into the etched holes by gold evaporation. In the second method, substrate is first spin-coated with a photoresist material. Following to coating, a soft mask carrying the inverse of TLM images was aligned on substrate (negative resist). The substrate was then exposed to UV radiation to develop negative image of the mask on substrate. Here, UV radiation causes negative resist to polymerize and more difficult to dissolve. This way, negative

resist remains on the substrate and a developer solution cleans the coating on unexposed regions (TLM pattern). Once the TLM pattern was prepared, electrodes were placed on substrate by gold evaporation.

Since graphene monolayers are sensitive to minute mechanical strain, it is absolutely necessary to make the substrate surface as flat as possible after patterning the metallic contact lines. A simple micro-fabrication process where metallic structures can be embedded inside a substrate is adapted for the currently used thermally oxidized silicon substrate (1 micron oxide layer). A mask (Figure 14 (e)) with TLM contact line patterns was aligned on the sample wafer and was etched with silicon hexafluoride based DRIE recipe, depicted in Table 4.

In the next step, e-beam evaporator (NanoVak NVTE4-01 Thermal Evaporator) was used to deposit a Cr adhesion layer of 20 nm thicknesses, followed by the deposition of a 100 nm thick thermally evaporated Au electrode, without removing the mask. This resulted in a perfectly flat substrate with embedded metallic TLM lines. In order to see the effect of employing photolithography on flatness, soft mask prepared for photolithography was replaced with a hard mask. Figure 14 (a, b, c, d) depicts the fabrication steps, while Figure 14 (e,-g) shows the top and cross-sectional views of the sample after the deposition of graphene and polymer films. An actual image of the nanosensor is presented in Figure 14 (h).

Table 4 DRIE Recipe for Silicon nitride etchings (Oxford Plasma Lab)

SF6 flow rate	45 sccm
Pressure	7.5×10^{-9} Torr
DC forward power	50 Watts
ICP forward power	2000 Watts
Table temperature	10 °C
Silicon Di Oxide etch rate	~2.2 nm/sec
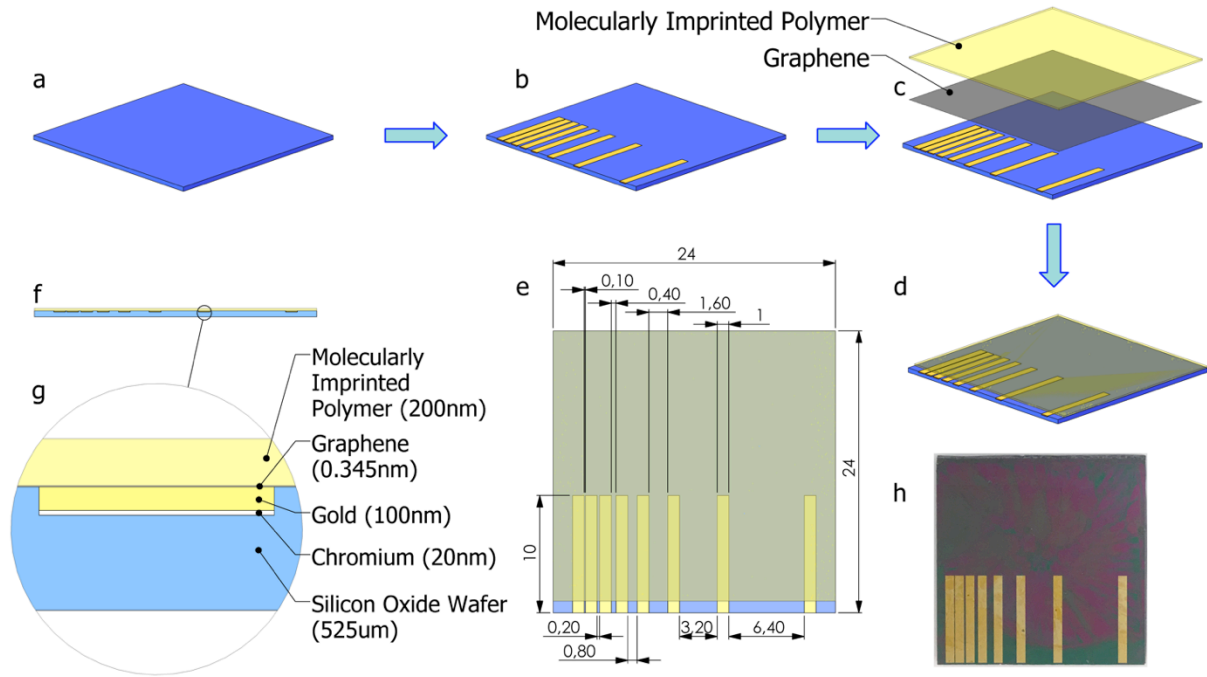
Figure 14 Schematic representation of fabrication steps and details of fabricated nanosensor; Si/SiO$_2$ substrate (a); etched and Cr/Au deposited substrate (b); monolayer graphene transfer and molecularly imprinted polymer spin-coating (c); layer-wise sensor view (d); top-view with TLM pattern length details (e), side-view (f), and details of side view (g); fabricated nanosensor (h). All dimensions in (e) are in mm.

3.2.5 Monolayer Graphene Transfer onto Si/SiO$_2$ Substrate

We transferred single layer graphene from copper substrate to Si/SiO$_2$ substrate prepared both by hard mask and photolithography. For this purpose, we first prepared graphene samples in desired shape and dimensions and then spin coat them using PMMA (5000 rpm, 50s) and dried (60°C, 2min; 180°C, 5min). The reason behind PMMA coating was to prevent any breakage of graphene since graphene is a very delicate material. Spin coating was carried out twice since our PMMA was very thin. Once the coating was done, we etched the backsides of graphene samples using plasma asher (CTorr, O$_2$ etching, P=100kW, 10 s). We then put the samples in ammonium persulfate solution (0.7%, overnight; or 7% 1 h) to etch the Cu substrate. Once the Copper is completely oxidized and the APS solution turned to blue, we removed the graphene layers into d-Water and washed overnight. We then collected graphenes on glass substrate and dried on hot
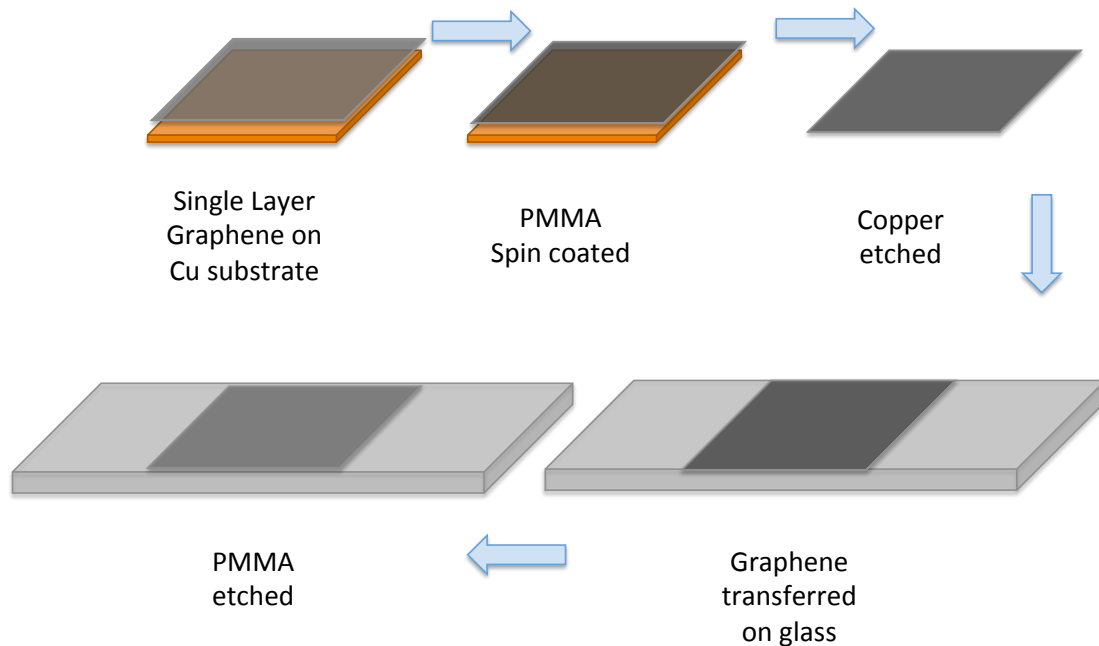
Figure 15 Graphene transfer process

plate (60 °C, 45min; 180 °C, 1h). To Finally, to remove PMMA, we put the graphene-coated substrate in acetone overnight and washed the samples with IPA and distilled water. Monolayer graphene was characterized by Raman Spectroscopy. Figure 15 demonstrates graphene transfer process onto Si/SiO_2 substrate.

3.2.6 Scanning Electron Microscopy

The surface of the substrate with metallic contact lines and graphene was investigated by Scanning Electron Microscopy. For this purpose, samples were sputter coated with a thin layer of Pt/Pd. Images were acquired by SEI detector, using an electron gun voltage of 2 kV.

3.2.7 Raman Spectroscopy

Raman spectra of graphene samples transferred onto glass substrate were obtained at 532 nm visible excitation using Renishaw InVia Reflex Raman Spectrometer attached to a microscope.

3.2.8 Electrical Measurements

The change in resistance of monolayer graphene due to NTO adsorption onto molecularly imprinted chitosan was measured by two-probe setup (Cascade MicroTech PM5 Probe Station). Sheet resistance of graphene was calculated by linear fit of Equation 1. Details of sheet resistance calculations by TLM are found in Appendix A.

$$\textbf{Equation 1}$$
$$R_{Total} = (R_{sheet}/W_{channel})\, d + 2R_{contact}$$

3.3 Results and Discussion

3.3.1 Chemical Characterization of Molecularly Imprinted Films

Figure 16-a shows the attenuated total reflectance (ATR)-FTIR spectrum of native CS. The band at 1149.94 cm^{-1} and overlapped bands round 1022 cm^{-1} are attributed to asymmetric C-O vibrations resulting from deacetylation and C-OH and C-O-C vibrations of the β-(1-4)-linked D-glucosamine (deacetylated unit) and N-acetyl-D-glucosamine (acetylated unit) rings, respectively. In addition, the absorption bands at 1314.56 cm^{-1} are attributed to C-H bending of -CH$_2$ groups, while the one at 1373.56 corresponds to C-O stretching mode of -CH$_2$-OH groups. The peaks within the range of 1589.79-1651.34 cm^{-1} correspond to the bending mode of primary amino groups and carbonyl stretching, respectively. The broad absorbance band in the region of 2862.72 cm^{-1} corresponds to symmetric and asymmetric stretching of the aliphatic -CH$_2$ and -CH$_3$ groups. The wide peak centered at 3287.05 cm^{-1} originated from -OH groups along with H-bonding.

Crosslinked CS samples showed similar FTIR bands to CS, with slight shifts, within the range of 800-1200 cm^{-1} that corresponds to main saccharide ring. Different than native CS, crosslinked non-imprinted (Figure 16-b) and NTO-imprinted (Figure 16-c) CS spectra showed some additional vibrations. For instance, the newly formed bands around 1550 cm^{-1} in crosslinked species revealed the existence of quaternary amino groups.[96] Moreover, the sharp band around 1636 cm^{-1} of C=N vibrations proved the formation of Schiff's base upon crosslinking.
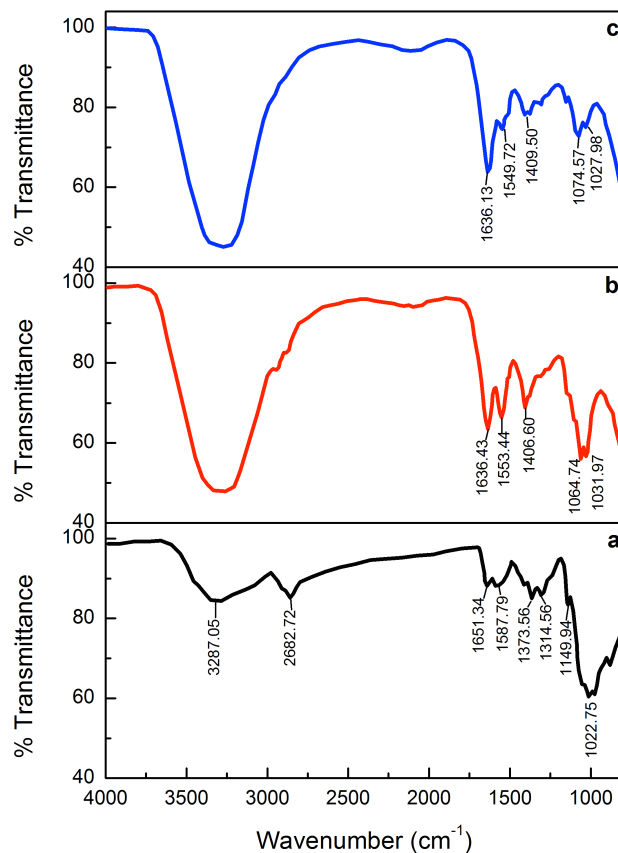
Figure 16 FTIR spectra of native (a), crosslinked, non-imprinted (b) and NTO imprinted chitosan (c).

3.3.2 Adsorption Studies

To track the adsorption capacities of non-imprinted and imprinted chitosan samples, we first introduce the gels into a 10 mg/mL NTO solution and allow NTO's to be adsorbed onto gel surfaces overnight. Then we carried out UV-Vis spectroscopy in order to detect the decrease in the amount of NTO in the solution and compared them to the original 10mg/mL NTO solution. Both non-imprinted and NTO imprinted chitosans adsorbed NTO, but imprinted one is slightly better in adsorption. Figure 17 demonstrates the Uv-Vis spectra of NTO adsorbed CSNTO, CSNIP and standard NTO solution (10 mg/mL, 320x diluted).
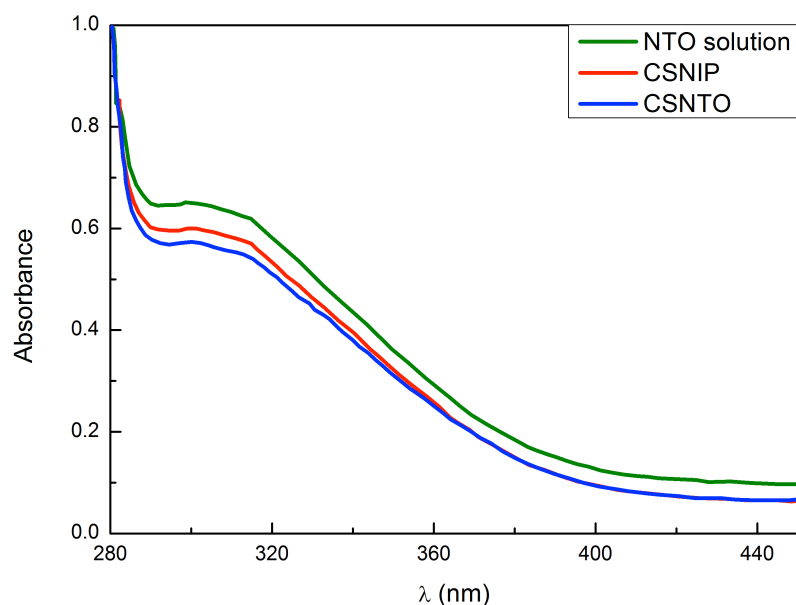
Figure 17 Uv-Vis spectra of NTO adsorbed CSNTO, CSNIP and standard NTO solution.

3.3.3 pH & Swelling Kinetics

To optimize NTO adsorption in CS films, pH and swelling kinetics studies were carried out. Swelling kinetics was investigated by subjecting imprinted and non-imprinted CS gels with different GA amounts to 2% acetic acid solutions. Swelling degree was calculated from the weight ratio between dry and swelled gels. Figure 18-a suggested that a non-usual swelling trend was observed in CSNIP gels due to the presence of free amino- functional groups. On the other hand, an inverse proportion between crosslinker amount and swelling was observed in CSNTO gels implying that the network gets more rigid with increased crosslinker amount. Considering high crosslinking with a low swelling degree of CSNTO films as the selection criteria, the optimum range of crosslinker amount was determined as 8-12%.

Furthermore, it was also observed that films prepared with 12% crosslinker were brittle and easily broken during measurements. Therefore, 8% was chosen as optimum crosslinker concentration.

Once the crosslinker amount was optimized, the effect of pH on swelling (Figure 18-b and NTO adsorption capacities of films (Figure 18-c) were tested by exposing gels to 0.1 mg/mL NTO

44

solutions prepared in different pH buffers. Immersed films were then compared to original solutions in terms of UV-Vis absorption. As seen in Figure 18-b, lowest degree of swelling was observed at pH 6.7 and 12.0 for both gels. Although NTO adsorption capacity of CSNTO was significantly higher between pH 3.7-4.7, a very significant swelling, up to 7x was observed in NTO imprinted CS around these pH values (Figure 18-c). Therefore, this region was omitted. In addition, Figure 18-c also suggested that NTO adsorption of CSNTO was significantly higher than that of CSNIP at pH 6.7. Considering lower swelling and higher NTO adsorption, an optimum pH value of 6.7 was selected and further measurements were carried out at this pH value.

3.3.4 Effect of NTO Amount on Molecular Imprinting

Effect of NTO amount on imprinting was investigated by Uv-Vis spectroscopy. For this purpose, Chitosan-NTO solutions were prepared in different NTO amounts (Table 5). Chitosans were crosslinked by glutaraldehyde (1%) and left to gelate. After washing, gels were exposed to NTO solutions (1 mg/mL) and UV-Vis spectra were recorded and compared to reference NTO solution.

Table 5 Sample names, amount of imprinted NTO (g) and CS solution (12mg/mL) used in NTO optimization.

Sample Name	Imprinted NTO amount (g)	Amount CS (mL)
CSNTON1	0.05	50
CSNTON2	0.10	50
CSNTON3	0.30	50
CSNTON4	0.60	50
CSNTON5	0.90	50

Uv-Vis spectroscopy revealed that NTO adsorption was minimum around 12-18 mg/mL NTO concentrations (Figure 18 (d), while it enhances significantly with the reduction in NTO in gel preparation medium. In addition, it was observed that high concentrations of NTO increase the
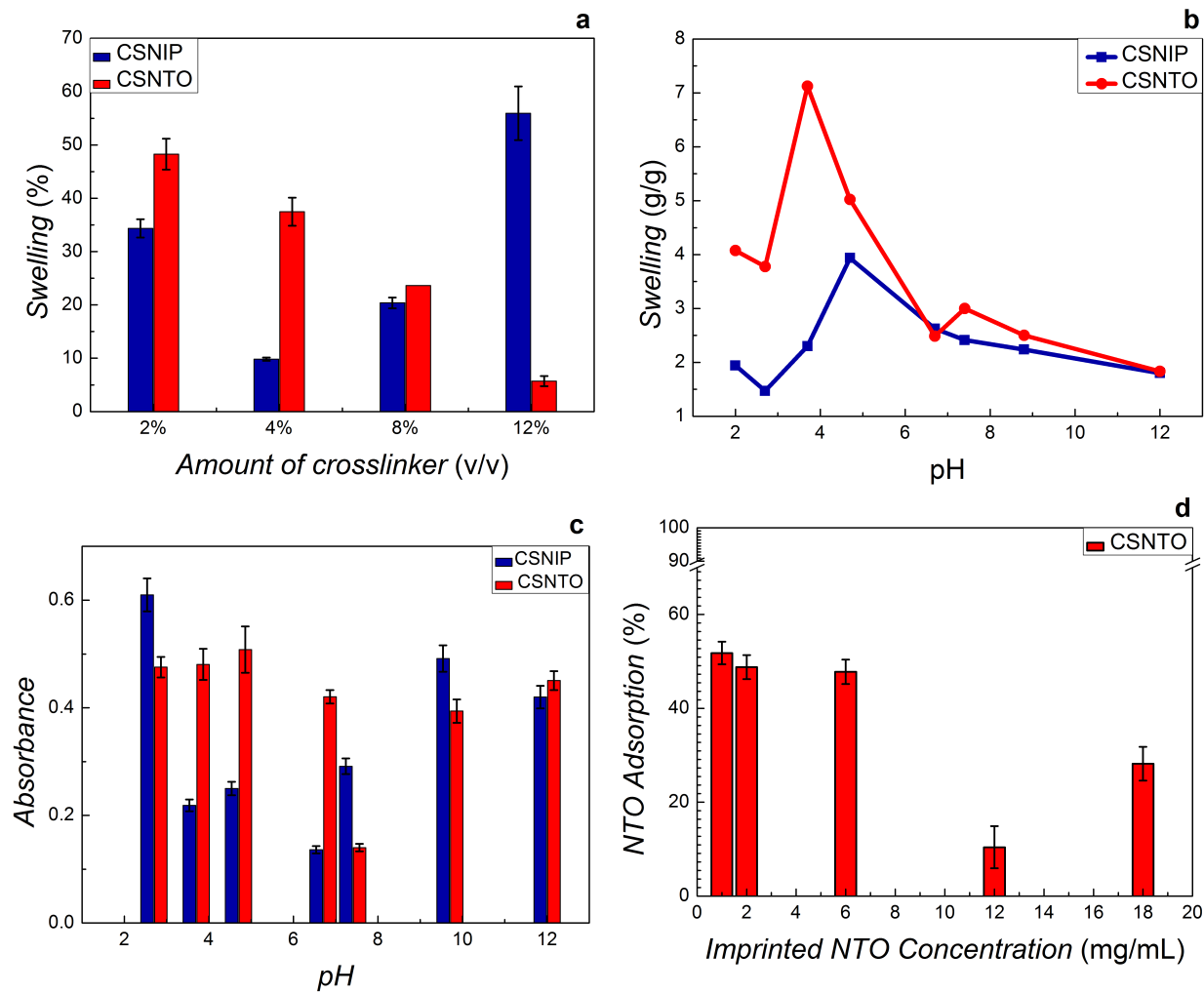
Figure 18 Effect of pH on swelling (a) and on NTO adsorption (b) with respect to crosslinker amount; effect of crosslinker amount on swelling (c); and amount of imprinted NTO on NTO adsorption of molecularly imprinted films (d). Non-imprinted films are shown in blue and imprinted films are shown in red.

crosslinking time (crosslinking resulted in viscous liquids rather than a rigid gel). We presume that high amounts of NTO aggregate and block the crosslinking regions of polymer chains. Taking these parameters into consideration, optimum amount of NTO in imprinting was determined as 1-2%.

3.3.5 Elution Studies

One of the important aspects with molecularly imprinted films is that the interaction with the analyte should be reversible. To test the reversibility of NTO adsorption on molecularly
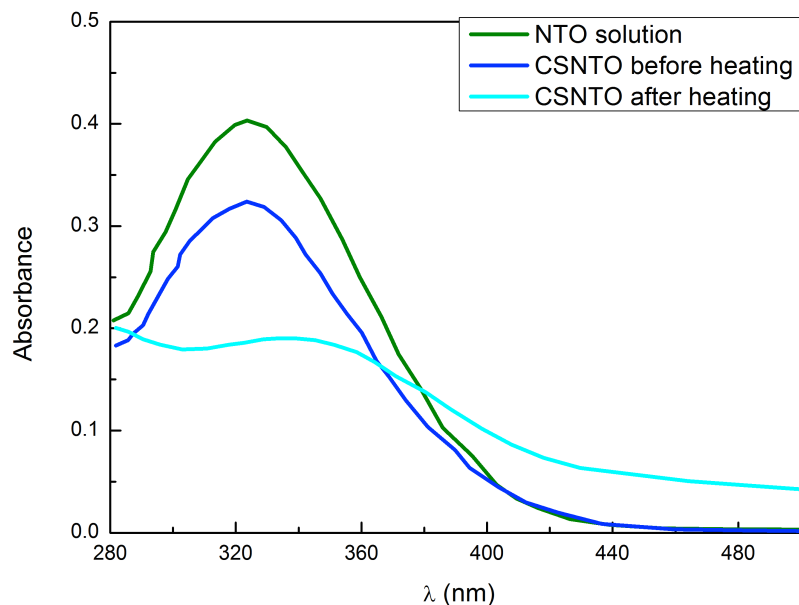
Figure 19 Uv-Vis spectroscopy results of washed CS films with and without heating, and standard NTO solution.

imprinted CSNTO films, elution studies were carried out. For this purpose, molecularly imprinted CSNTO films were immersed into NTO solutions (10 mg/mL) and washed back. NTO molecules eluted by CSNTO films were tracked by Uv-Vis spectroscopy of the washings. Figure 19 shows the Uv-Vis results of the immersed CSNTO films following washing.

Uv-Vis spectra of NTO solution against dialysis washings of CSNTO film suggested that NTO solution demonstrated a sharp peak in the near UV region, which was also found in dialysis washings before heating. Dialysis sample before heating showed an absorption that has same λ_{max} with NTO, indicating that NTO's were washed off during dialysis. On the other hand, heating caused to a blue shift in the λ_{max} of the dialysis sample, which might have aroused from chitosan removal from the surface during heated dialysis, since chitosan had a wide absorption peak at farther UV region. Therefore, heating was omitted from elution process.

3.3.6 Durability

Another important aspect of the prepared CS films is the durability and integrity of the film. This is particularly important since all the analyte measurements are carried out in aqueous solutions of NTO. Therefore, prepared CS films should be durable in solution. In that case, integrity of the film is related with hydrophobicity since disintegration of films from substrate surface is only possible if the films are hydrophilic. To examine the hydrophillicity of molecularly imprinted CS films, contact angle measurements were carried out. Figure 20 demonstrates contact angle measurements of non-imprinted and NTO imprinted CS films.

Contact angle measurements showed that hydrophillicity of CS films decreased upon NTO imprinting. This might have aroused from the decrease in solvent accessible area since NTO molecules occupy the binding pockets created within the CS film surface.
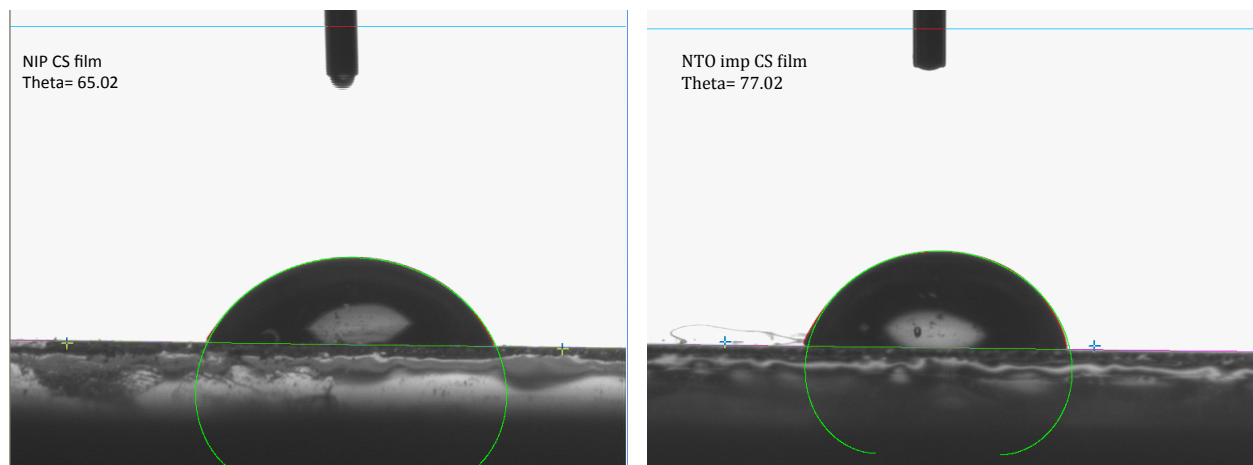
Figure 20 Contact angle measurements of non-imprinted and NTO imprinted CS films.

3.3.7 Micro Fabrication

Figure 21 shows microscopic images of leveled (flat) (a) and unlevelled (b) gold electrodes before graphene transfer; SEM images of unlevelled (c) and leveled (d) after graphene transfer. It was observed from optical microscopy and SEM images that after graphene transfer (Figure 21 a-b) leveling by photolithography, instead of using hard mask is a crucial step in micro fabrication. SEM images of graphene on an unlevelled gold-Si/SiO$_2$ (Figure 21-c) substrate revealed that graphene was scratched when transferred on unlevelled substrate. Therefore, height

profiles should be carefully investigated following each gold deposition. On the other hand, Figure 21-e-f demonstrates optical microscopic images of sensor following photolithography. Comparing the optical microscopic images of sensors fabricated with a hard mask (a) and a soft mask (b) with same TLM patterns, it was observed that the edge groove and unevenness is considerably cured when a soft mask was employed.
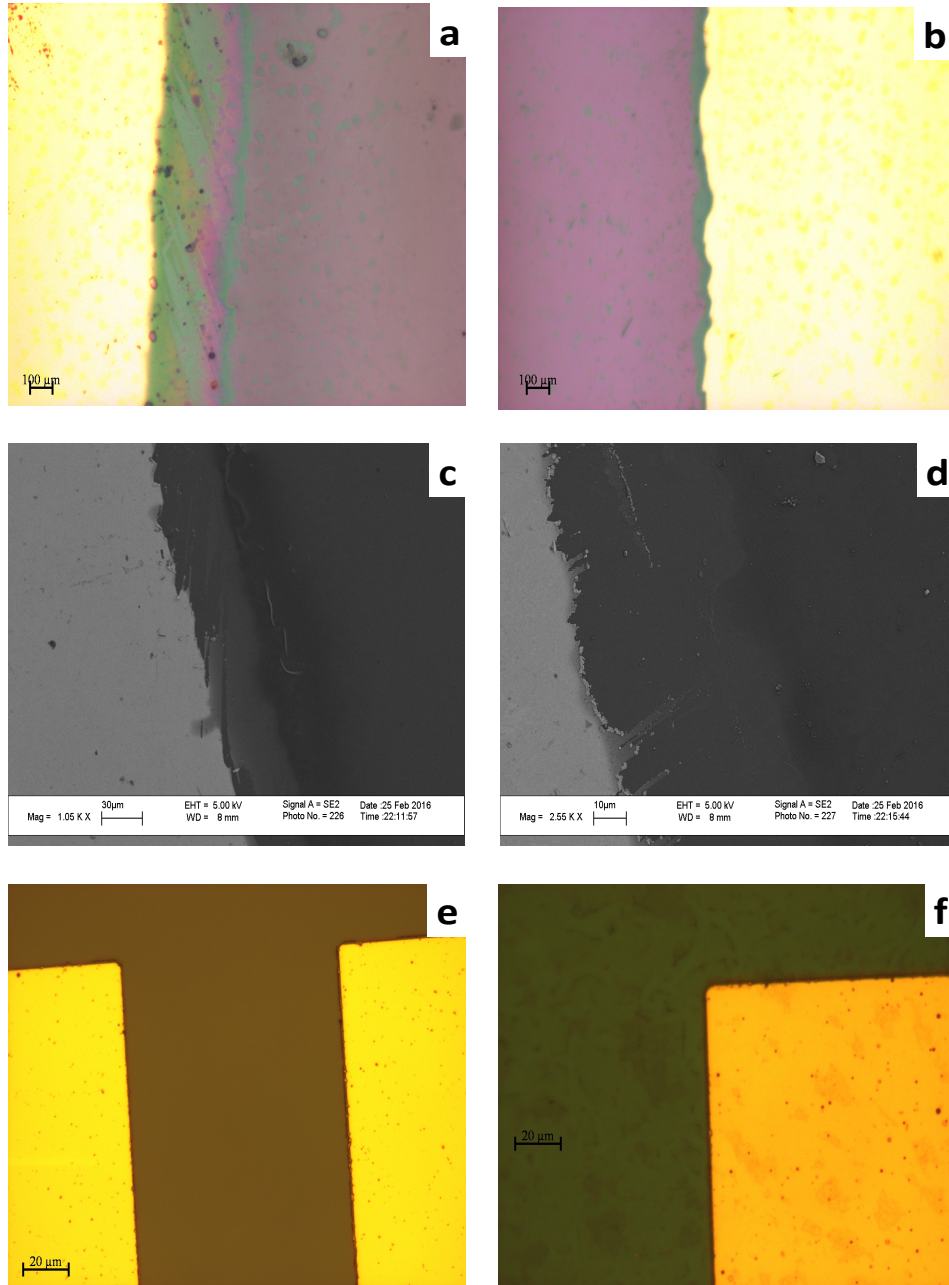
Figure 21 Optical microscopic images of graphene on unlevelled (a) and levelled (b) gold electrodes; SEM images of graphene on unlevelled (c) and levelled (d) gold electrodes. Optical microscopy images of levelled gold electrodes (yellow) on SiO2 substrate (brown) fabricated by photolithography without (e) and with (f) graphene.

3.3.8 Monolayer Graphene Characterization

Raman Spectroscopy was employed to confirm monolayer graphene. For graphene samples, two characteristic Raman peaks were observed due to a Stokes phonon energy arising from laser excitation. The first one, G band observed at 1593 cm^{-1}, corresponds to primary in-plane

vibrations, whereas the second one, 2D band observed at 2689 cm^{-1}, accounts for a second order two-phonon process exhibited by all sp^2 carbon materials. 2D is the highest intensity peak in a single layer graphene spectrum and along with G band; it can be used to determine the number of layers of a graphene sample. In multi-layer graphene 2D peak is split into four and reduces in intensity. As seen in Figure 22, our sample showed 2D>G behavior in band intensity from different regions, therefore monolayer graphene was confirmed.
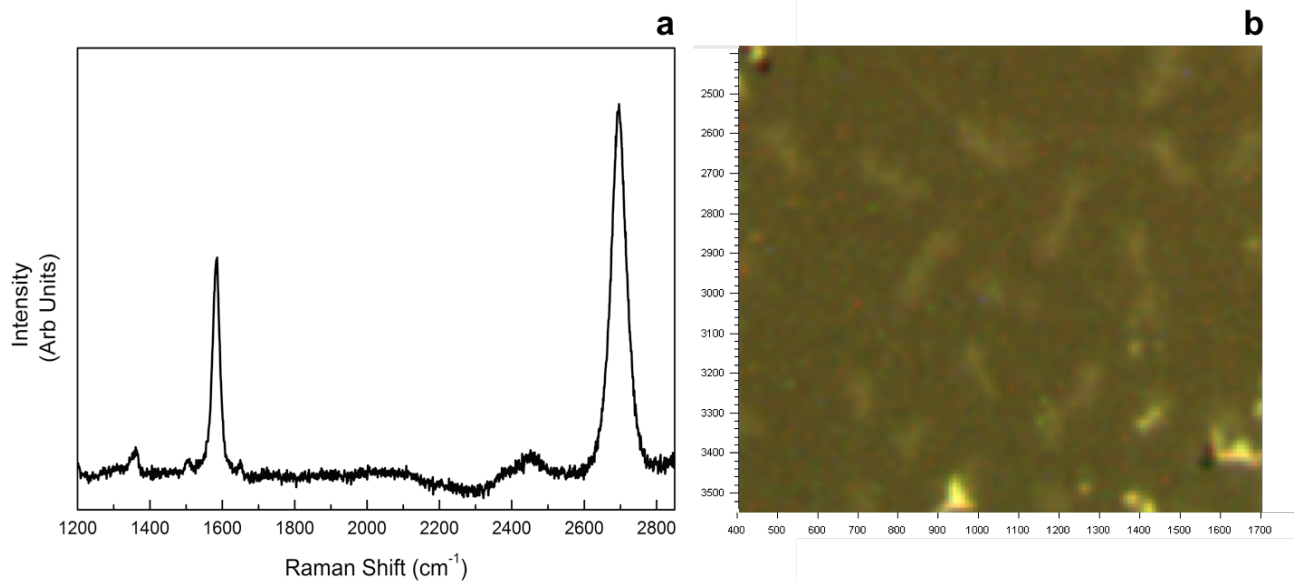
Figure 22 Raman Spectrum of monolayer graphene (a), and microscopy image of the area Raman data was gathered (b).

3.3.9 TLM Measurements and Sensitivity Studies

Prior to polymer coating, sheet resistance of graphene on SiO$_2$ was measured by TLM and determined as 418,2 ohm/sq which correlated well with the literature data.[97] With 160 nm polymer coating, this value was increased to 832,0 ohm/sq due to the introduction of low-conducting layer (0.25 ± 0.09 S/m) [98] when compared to monolayer graphene (2.62 × 10^2 S/m).[99]

A series of TLM measurements were carried out to determine the sensitivity of fabricated nanosensor by exposing sensors to NTO solutions in different concentrations. Subjecting to

51

increasing current, I-V measurements were carried out and sheet resistances were calculated by the slope of resistance curves at increased contact pair distances. Details of sheet resistance calculations were explained in Appendix A. Sensor fabricated using NTO imprinted CS was treated with NTO solutions and TLM measurements were carried out following air-drying. TLM measurements were carried out in concentration and current range of 0.01-0.1 mg/mL and 0.01-0.1 mA, respectively. This way, a standard curve was obtained for each NTO concentration value. Sheet resistances were obtained from slopes of standard curves and plotted against corresponding NTO concentration. Results show that sensor fabricated using NTO imprinted CS gave linear response to increased NTO concentration in the range of 0.01-0.1 mg/mL. Therefore, measurement limits were determined as 0.01 and 0.1 mg/mL. Therefore, measurement limits were determined as 0.01 and 0.1 mg/mL. This detection limit is acceptable considering that the sensor probe is composed of a polymeric thin film. Table 6 summarizes high performance nitroaromatic sensors found in the literature, their type of measurement, detection limits and response times. Comparing literature examples to our sensor[45-57], one can conclude that there are sensor studies available in the literature with better response times and low detection limits, nevertheless most of these methods rely on vapor-phase detection of nitroaromatics. This type of detection can be challenging due to the low vapor pressure of these nitroaromatics. In addition, most of the measurements require sophisticated instrumentation. In our case, fabricated nanosensor is advantageous in terms of ease of measurement (a simple I-V test) with wide linear range.

Table 6 Comparison of sensing performances of selected nitroaromatics sensors found in literature.

Sensing Material	Measurement Type	Detection Limit	Response Time (min)	References
Molecularly imprinted polymer thin film-graphene	Electrical	10-100 ppm	<5	*This work*
Electrochemical gas sensor	Electrochemical VP*	50-500 ppm	10-20	[100]
Siloxane	SAW**-VP	235 ppt	0.84	[101]
Carbowax-silica	SAW-VP	300 ppb	1	[102]
Molecularly imprinted cyclodextrin	SAW-VP	600 ppb	5	[103]
Dye embedded copolymer	Colorimetric	0.2 ng	*N/A*	[104]
Polyacetylene thin film	Fluorescence quenching	ppb level	<20	[105]
SiO$_2$ modified electrode	Cathodic voltammetry	1.8 nM	*N/A*	[106]
Fluorescent paper	UV	0.5 ppm	0.5	[107]
Pervoskite-reduced graphene oxide	GCE***-cyclic voltammetry	0.3-0.8 μM	*N/A*	[108]
PVA membrane	Fluorescent-optical	5.0×10^{-6} M	1	[109]
Graphene film	GCE-differential pulse voltammetry	1-200 ppb	1	[75]
Reduced graphene oxide	GCE-stripping voltammetry	5.49×10^{-7} M	*N/A*	[110]
Polystyrene-gelatin double film	Fluorescence quenching-VP	*N/A*	20	[111]

* Vapor pressure, ** Surface acoustic resonance, *** Glassy carbon electrode
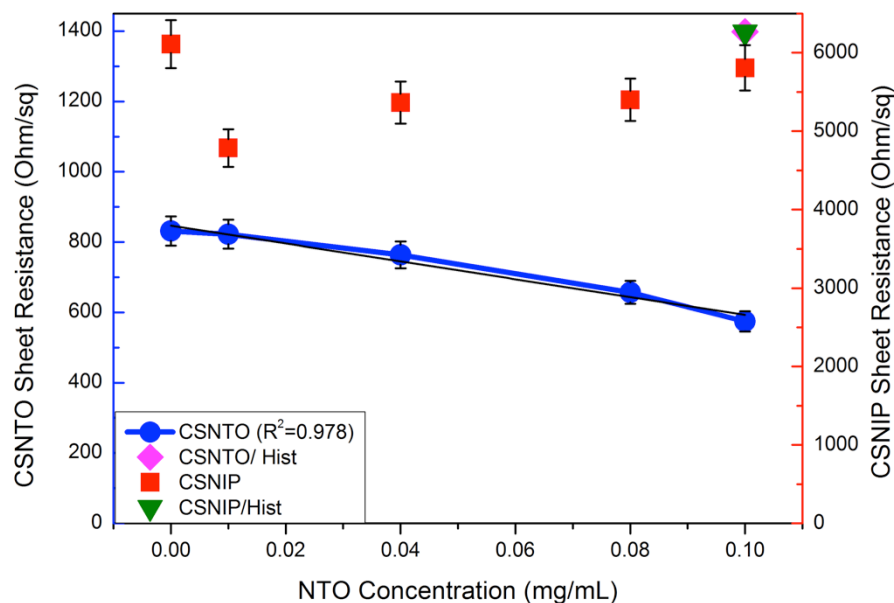
Figure 23 Selectivity comparison of non-imprinted (CSNIP) sensor to imprinted (CSNTO) against NTO and histidine (blue scale is also valid for histidine values).

3.3.10 Selectivity Studies

Selectivity studies were carried out by comparing the TLM results obtained from NTO imprinted and non-imprinted sensors. It was found out that non-imprinted sensor was insensitive to any change in NTO concentration. It was also observed that sheet resistance values obtained from non-imprinted polymer were relatively higher compared to the imprinted ones. This may be due to the fact that non-imprinted polymer non-selectively adsorbs different species present in the solution. Comparison of sheet resistance results obtained from NTO-imprinted and non-imprinted sensor are shown in Figure 23.

Selectivity studies also include the response of molecularly imprinted sensor to another chemical compound that is similar to NTO in molecular shape. To evaluate this, CSNIP and CSNTO sensors were exposed to 0.1 mg/mL histidine solutions and TLM sheet resistance values were re-calculated. It was observed that CSNTO sensor resulted in significantly higher sheet resistance values when treated with histidine, whereas non-imprinted sensor gave a sheet resistance value that was in the same order with the ones exposed to NTO. In other words, CSNIP failed to

distinguish analyte from other chemicals, and did not to respond selectively against different concentrations of NTO. On the other hand, CSNTO sensor is selective against NTO analyte, and does not respond to other species, even when a structurally similar chemical is introduced. Sheet resistance values obtained from NTO and histidine treatment of same concentrations are also shown in Figure 23.

3.3.11 Response Time & Noise Measurements

Noise and response time measurements were carried out by immersing CSNTO sensor into 0.1 mg/mL NTO solution. Sheet resistance was recorded with respect to time. Results revealed that the response time of CSNTO sensor was less than 5 minutes (Figure 24-a). In addition, it was observed that the data converged to a sheet resistance value of 574,2 ohm sq^{-1}, which correlated well with previous sheet resistance value for 0.1 mg/mL NTO (shown in Figure 23). This also implies that CSNTO sensor read reproducible sheet resistance values for same concentrations of analyte. In addition, noise level of the sensor determined as ±0.5 mV (Figure 24-b).
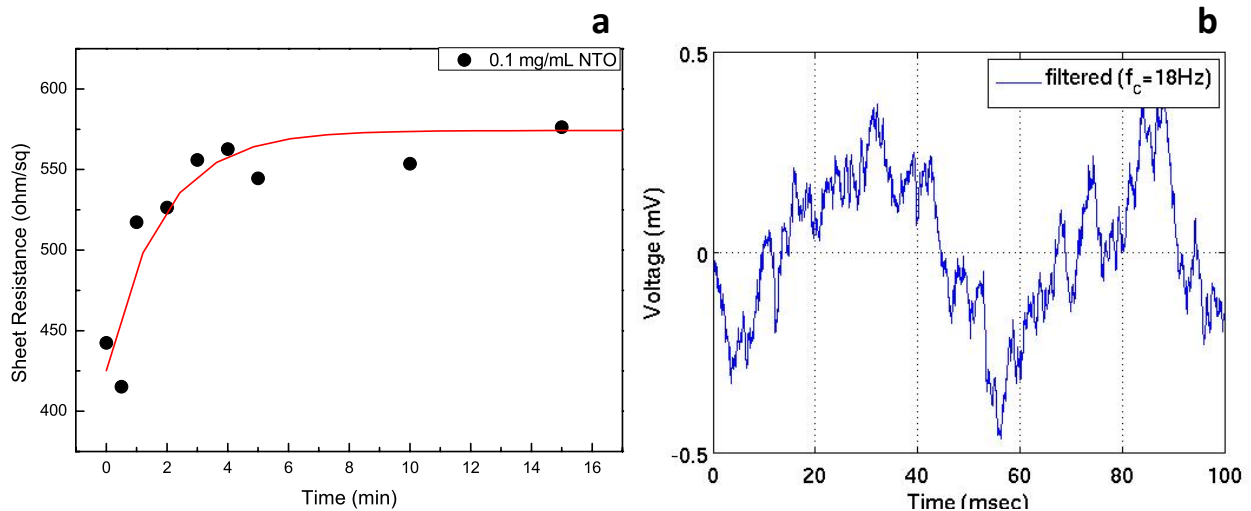
Figure 24 Response time measurements of CSNTO sensor for 0.1 mg/mL NTO solution (a) and noise measurement during a (b).

3.4 Conclusions

We have successfully fabricated molecularly imprinted chitosan-graphene nanosensor and linearly detected explosive NTO molecules in the range of 0.01-01 mg/mL analyte concentrations. Fabrication started with embedding electrodes into a non-conducting substrate, which is, to our knowledge, a unique technique in TLM pattern formation, followed by graphene transfer and polymeric film coating. It was noted that leveling of metallic electrodes with substrate, in other words, creating a flat surface after electrode embedding is a crucial step in sensor fabrication, since graphene was prone to breakage when transferred on unlevelled substrates. Following graphene transfer, monolayer graphene was verified by Raman spectroscopy and it was observed that graphene was successfully transferred and was continuous without any breakage. The performance of molecularly imprinted polymeric film was investigated and the amounts of NTO and crosslinker required for imprinting were determined along with optimum pH range and swelling. TLM measurements were carried out successfully, and was observed that imprinted film responded linearly to increased NTO concentration in the targeted range, which covers the lowest observed adverse effect, level value of NTO determined by USEPA. Therefore, toxic levels of NTO are within the detectible limits of the developed sensor. In addition, employing molecularly imprinted polymeric films as sensor probe is advantageous in detecting analytes in a linear fashion since non-imprinted polymer failed to give a linear response region. In addition to this, a chemical compound with a similar molecular shape was tested with the fabricated sensor in order to verify the lock-key model between molecularly imprinted film and analyte. It was concluded that sensor with molecularly imprinted polymeric film was insensitive against this compound, whereas sensor with non-imprinted produced false positives with chemical compounds in similar shapes. In other words, molecular imprinting was not only important in terms of giving a linear response region for analyte, but it also served to increase the selectivity of polymeric film in the range of linear response.

To sum up, a molecularly imprinted polymer-graphene based nanosensor was developed to selectively detect NTO from ecological water samples. Fabrication technique used to prepare this sensor combined micro fabrication and polymer technologies and is unique in terms of embedding electrodes into sensor substrate, as most of the studies in this field were based on

fabricating metallic electrodes on top of graphene sheet. Sensors fabricated using this method are re-usable, respond linearly with the analyte within the targeted region of analyte concentration and selective against the analyte molecules. Although there are other methods available in the literature to measure nitroaromatics in lower concentrations, these methods usually require sophisticated instrumentations such as XPS and Raman. Unlike the others, sensor developed in this study provides easy measurement techniques applicable to field studies with less effort.

CHAPTER 4 Soft Segment Length Controls Morphology Of Poly(Ethylene Oxide) Based Segmented Poly(Urethane-Urea) Copolymers In a Binary Solvent

4.1 Introduction

Urethane-urea chemistry is a powerful tool in synthesis of elastomers used in different industrial processes such as biomaterials, coating materials and textiles. [112-118] These type of polymers are usually composed of two segments, in which physically crosslinked, densely hydrogen bonded urethane-urea groups serve as stiff domains (hard segments, HS) and soft segments (SS) form into the bulk of the material that endows the high extensibility. Here, HS are obtained by diisocyanate reactions where diols or diamines act as chain extenders. On the other hand, SS are usually selected as difunctionally terminated telechelic oligomers. Thus, thermal and mechanical properties of these two domains are significantly different from eachother. HS domains are designed to have a T_g or T_m significantly higher than the service temperature range, whereas SS domains are selected as having very low T_g. [119] The choice of segments' composition lead to thermodynamic incompatibility between segments and effect several properties such as the packing behavior and morphology. This leads to different morphological traits in the segmented polyurethane-urea copolymers such as phase-separation or self-assembly of basic building blocks. [115] Therefore, control of structure and morphology enables fine-tuning of properties, giving rise to final materials with various functions. [118]

In thermoplastic polyurethanes (TPUs) the structure-property and morphology relationship is determined by several parameters. These parameters can be categorized into four groups. First group may be addressed as the chemical structure, secondary interactions and chain size / length properties. Second group is defined by the context of soft segment, *i.e.* chemical nature, molecular weight and Hildebrand solubility parameter of the soft segment. The third group of parameters determining structure-property-morphology relationship is the type and extent of

intermolecular interactions in between hard and soft segments. The fourth and final group is the polymerization procedure and reaction conditions. [115]

Here, design of the reaction conditions; particularly selection of the solvents is of high importance.

Selection of reaction conditions and the polarity of solvent are particularly important among the parameters in synthesis of segmented poly(urethane-urea) copolymers. Their effect become more significant especially in the case of high molecular weight, high hard segment content and/or polyether based soft segments. [120] Commonly used solvents in preparation of segmented poly(urethane-urea(copolymers are THF, DMF and their mixture. Experimental studies on these parameters have been conducted during the last decades including different synthesis approaches, [121-124] mechanical properties,[125-128] structure-property relationship[129-131] including morphology,[132-134] and micro-phase separation[135]. On the contrary, limited amount of computational studies are found on investigation of critical parameters that determine structure-morphology-property relations in segmented poly(urethane), poly(urea) and/or poly(urethane-urea) copolymers. [136-140] For this reason, theoretical investigations on the behavior of copolymer's hard and soft segment building blocks in the presence of these solvents are crucial to help raise the knowledge on structure-morphology-property relations in multiple length scales.

Poly(ethylene oxide) is a promising candidate as soft segment in preparation of polyurethanes due to the several factors. For instance, macromolecular PEO can form into various physical states because it has high conformational freedom. Secondly, due to its amphiphilic nature, PEO can form multiple hydrogen bonds. In addition to these, vast amount of literature on characteristic parameters and folding properties as a function of chain length giving rise to fine-tuned morphologies in varying molecular weights, biocompatibility and water solubility. The ease of synthesis and availability of various commercial products are other important aspects of PEO. [141-148] The use of PEO is also important for targeted applications based on PEO:urea host-guest complexes as they can be considered as model systems for supramolecular polymeric materials.

In parallel to the increase in computational power in the last decades,[149] multi-scale modeling has enabled researchers support experimental results *in silico*, to help explain events taking place on the atomistic scales where experimentally accessible information do not suffice. While molecular dynamics (MD) simulations have the potential to provide this information, applications to multi-chain systems usually require massive computing resources since they numerically solve Newton's equation of motion for each atom in the system that also incorporates many solvent molecules. On the other hand, dissipative particle dynamics (DPD) simulations use coarse-grained beads into which sets of atoms are clustered. [150, 151] It then becomes possible to build a connection between the atomistic and macroscopic scales. Studies have been published on multi-scale modeling of polymeric systems to explain various mechanisms ranging from self-assembly of light harvesting systems[152], polymer adsorption on silica surfaces[153], solvent effect on morphology of electrosprayed surfaces[154], self-assembly of copolymers[155], molecular chain conformations below and above critical temperature[156], to name a few.

Coarse grained and multi-scale simulation studies of segmented poly(urethane urea) copolymers found in the literature provide crucial information on the structure-morphology-property relationship. For instance, molecular and mesoscale simulations of a segmented silicone-urea copolymer suggest that the copolymer demonstrates a very distinctive phase separation even for the smallest HS content.[157] Using coarse-grained models, it was also demonstrated that morphology of the copolymer mainly depends on SS selection in which hydrophobic SS blocks favor microphase separation.[140] In addition, morphologies of poly(tetramethylene oxide) based segmented poly(urethane-urea) copolymers investigated by coarse-grained model suggest that intermolecular interactions play an important role in strain hardening of the material.[158] This study, on the other hand, deals with the effect of SS chain length on the morphological behavior of the poly(ethylene oxide) based segmented poly(urethane-urea) copolymers in a complex solvent system of THF:DMF (1:6.25). For this purpose, an atomistic model of the soft segment was first built and single chain properties of poly(ethylene oxide) (PEO; SS) with increasing chain length was investigated. This was then compared to DPD studies of the same chain length set to test the reliability of DPD model employed. HS molecules were then incorporated into the chains, and DPD simulations were carried out for three different copolymers with varying HS and

SS chain length to obtain the final morphologies. Secondary interactions established between urethane and PEO molecules are found to be mainly responsible for morphology differences observed in segmented copolymer with varying HS and SS chain length, a finding that is supported by monitoring interactions of reverse mapped structures of the copolymer where full atomistic detail has been recovered. Density fields obtained from DPD simulations are also in good agreement with atomic force microscopy (AFM) images of the corresponding systems.

4.1.1 Classical Molecular Dynamics Theory

Precise simulations of atomic interaction require Quantum Mechanical (QM) calculations. However, these calculations are computationally expensive and time-consuming, considering the fact that QM solves time dependent Schrödinger equation for each and every atom in the system. [159] For this reason, this method can only be applied to the systems containing 10-100 atoms in practical time scales. Even though it was applicable large systems such as polymers, the information of electronic properties provided by QM calculations would mostly be insignificant for macromolecules. In simulations of large systems, the output is usually bulk properties including diffusion coefficient and Young's modulus and these properties depend on locations of atomic sets.

A dynamic simulation can be run once energy optimized structure is established. The basics of a dynamics simulation are equations of motion. Equations of motion can be modified to deal with the effects of temperature and pressure. The output of a dynamics is a trajectory of atomic configurations and velocities over a period of time. Other properties are be derived from trajectory.

4.1.1.1 Equations of Motion

To simply put, MD simulations solve Newton's equation of motion;

$$\textbf{Equation 2}$$
$$\boldsymbol{f_i(t) = m_i a_i(t)}$$

where f_i is the force, m_i is the mass, and a_i is the acceleration of particle i at time t. Here, the force of an atom at a coordinate r_i is calculated from the derivative of potential energy V;

Equation 3

$$-\frac{\partial V}{\partial r_i} = m_i\,\frac{\partial^2 r_i}{\partial t^2}$$

It is important to note that the classical equations of motion are deterministic. In other words, the coordinates and velocity of an atom at time t can be determined using initial coordinates and velocity of the atom. This means that the trajectory of an MD run is sensitive to initial coordinates, therefore different trajectories may be obtained using different simulation tool or computer. In addition, the initial coordinates of a molecule are obtained by previous operations such as energy minimization while initial velocities are generated randomly with respect to desired temperature. This is another rationale of the fact that MD simulations cannot be repeated identically. One approach is to overcome is to employ force fields that allow setting the random number seed the same as the previous runs.

4.1.1.2 Statistical Ensembles

Integration of Newton's equation of motion results in constant-energy surface of a model. However, most of the natural phenomena do not take place under constant temperature and pressure. In contrast, natural events are exposed to pressure and heat exchange and total energy of the system is not conserved. To represent this situation in MD calculations, several approaches were developed by keeping three of the state variables (energy E, enthalpy H (that is, $E + PV$), number of particles N, pressure P, stress S, temperature T, and volume V) constant. Statistical ensembles are listed as follows: [160]

- Constant temperature and pressure (NPT)
- Constant energy volume (NVE)
- Constant pressure, constant enthalpy (NPH)
- Constant temperature, constant volume (NVT)

Note that in all ensembles, number of particles is kept constant. The ensembles NPT and NPH can only be applied to periodic systems since volume is not defined in non-periodic systems.

NVE ensemble: Also known as *microcanonical* ensemble, NVE is obtained by calculation of standard Newton equation without a temperature or pressure control. Here, energy is conserved

when deriving this adiabatic ensemble. This ensemble is not employed in calculation of equilibrium conditions. Since temperature is not controlled in NVE, the desired temperature is usually not achieved.

NVT ensemble: Also known as *canonical* ensemble, NVT is obtained by keeping temperature constant. For this purpose a thermostat coupling is employed. NVT ensemble is useful in calculating conformations of the models in vacuum without periodic boundary conditions since volume, pressure and density are defined by periodic boundary conditions.

NPH ensemble: This ensemble is an analogue of NVE, but in NPH ensemble, size of the unit cell is variable. [161] Since enthalpy (*H*) is the sum of *E* and *PV*, NPH ensemble is obtained by keeping pressure constant without temperature control. The control of pressure in MD simulations is carried out employing a barostat. Specific heat at constant pressure, thermal expansion coefficient and adiabatic compressibility can be calculated using NPH ensemble.

NPT Ensemble: This ensemble enables to control both temperature and pressure simultaneously. Here, temperature and pressure are kept constant by employing thermostat and barostat, respectively. NPT is used when exact values of pressure, volume and density are important in the calculations.

4.1.1.3 Equilibrium Properties

The main objective in MD simulations is to calculate equilibrium thermodynamic properties. A microscopic dynamic variable *A* over a time period *t* can be calculated by;

Equation 4

$$A(t) = \lim_{T \to \infty} \frac{1}{T} \int_0^T A(t)dt$$

This time averaging allows calculating first order properties such as internal energy, kinetic energy and pressure. Microscopic expressions of these first order properties in the form of fluctuations enable calculating thermodynamic properties of a system such as thermal expansion, specific heat and bulk modulus.

4.1.1.4 Temperature

Temperature is a macroscopic property derived from microscopic kinetic energy. In MD simulations, kinetic energy of a system is calculated from atomic velocities. Equation 5 defines the average kinetic energy of a system:

Equation 5
$$\langle K \rangle = \frac{N_f k_B T}{2}$$

where K is the kinetic energy, N_f is the number of degrees of freedom, T is the thermodynamic temperature of the system. The brackets denote the average of ensembles. The Born-Oppenheimer approximation of nuclei and electrons defines the degrees of freedom as

Equation 6
$$N_f = 3N - 6$$

for nonlinear molecules with $N>2$. [162] $3N$ is due to the movement of atoms in 3 dimensions, and 6 degrees of freedom are subtracted because the whole body rotation and translational motion around the center of mass in each 3 axis are ignored. But for periodic systems, only the translational motion of the center of mass can be ignored. Therefore the equation becomes:

Equation 7
$$N_f = 3N - 3$$

In MD simulations,

Equation 8
$$N_f = 3N$$

for an unrestricted system with N atoms, since the vibrational motions are ignored. The resulting degrees of freedom arise from 3 velocity components, v_x, v_y, and v_z, atoms. [163]

Thermodynamic temperature, T, of a system is the average of instantaneous Temperature, $T_{instant}$. Temperature of the system at an instant can be derived from Equation:

Equation 9

$$T_{instant} = \frac{2K}{N_f k_B}$$

Combining Equation 8 with Equation 9;

Equation 10

$$T_{instant} = \frac{2K}{3N k_B}$$

In MD simulations, initial velocities are generated to produce a Maxwell-Boltzmann distribution in the desired temperature. [164] The temperature, however, does not remain constant during the simulation due to the kinetic-potential energy exchanges. Therefore, several thermostat methods have been developed to keep the temperature at the desired value. The most frequently used thermostat methods include Berendsen, Hose-Hoover, NHL and Andersen. [164] In Berendsen method, temperature is kept constant by exchanging the thermal energy of the system with a heat bath. In Nose-Hoover method, an additional degree of freedom that represents the interaction of the system with a bath is introduced into the structure. The extended equations of motion are then solved to generate the ensemble. On the other hand, Andersen method randomizes the initial velocities at a predefined collision period to keep the temperature constant.

4.1.1.5 Pressure

Similar to temperature, pressure is a thermodynamic quantity that is only meaningful at equilibrium. In MD simulations, pressure is calculated by *the virial theorem:* [165]

Equation 11

$$pV = N k_B T + \frac{2}{3} \langle W \rangle$$

where W is the virial. [166]

The thermodynamic pressure, p, is the average of instantaneous pressure, $p_{instant}$, where the instantaneous pressure is defined as:

Equation 12

$$p_{instant} = \frac{Nk_BT_{instant}}{V} + \frac{2W}{3V}$$

Combining Equation 12 with Equation 10, we get

Equation 13

$$p_{instant} = \frac{2}{3V}(K + W)$$

Note that the pressure can only be defined if the system has a definite volume. In real world this is done by restricting the system in a container, whereas in computer simulations the unit cell with a periodic boundary condition is considered as a container. Similar to pressure, volume and density can only be calculated when the structure is bounded and periodic in all directions.

Similar to temperature, pressure needs to be controlled throughout the simulation to produce a correct statistical ensemble. Some of the frequently used pressure barostats include Andersen, Berendsen and Parrinello-Rahman. [166, 167] In Andersen and Berendsen methods, pressure is controlled by keeping the shape of the cell constant while changing the volume. On the other hand, Parrinello-Rahman method changes both volume and shape of the cell to keep the pressure in desired level.

4.1.1.6 Forcefields

The forcefield defines the energy surface on which atoms move. Forcefields are usually prepared to meet specific systems' criteria; therefore, forcefield selection is based on structure type. A forcefield comprises all the necessary information to calculate energy and force. The information include;

- Internal coordinates (Bond distances, bond angles, torsions)
- Partial charges
- Forcefield types
- Forcefield typing rules
- Energy expression functions

These elements are used to fit the potential energy surface. The internal coordinates terms, *i.e.* bond distances, angles, torsions are used to describe the potential energy surface due to the interaction of bonded and non-bonded atoms. Bonded atoms are defined via bond distance, angle torsion, while non-bonded interactions are defined by electrostatic and van der Waals interactions. Partial charges in a molecule are also predefined by forcefield, depending on the forcefield type of the atom. Along with the typing rules specific to forcefield employed, all the elements are created o generate the energy expression functions and the energy surface.

Forcefield types are prepared by a number of varying properties:

- Element (if atom)
- Type of bonds
- Number of bonding
- Hybridization
- Formal charge

Once the forcefield type is set for all the particles in a system, the forcefield uses them to generate the energy expression.

Equation 14
$$E_{total} = E_{valence} + E_{non-bonded} + E_{cross\,term}$$

Here, $E_{valence}$ is the sum of bond, angle, and torsion energies. Similarly, $E_{non-bonded}$ is the sum of van der Waals, Coulomb, and hydrogen bonding energies. Besides, $E_{cross\,term}$ stands for angle distortions caused by nearby atoms.

4.1.2 Dissipative Particle Dynamics Theory

The most significant drawback of MD simulations is that they employ all the atomistic details within a system. This approach is usually too detailed to understand several physical processes such as aggregation and phase separation. In addition to that, current computer processors allow simulating atomistic details up to a few thousand molecules over a few nanoseconds. Therefore,

with the current computer technology it is not possible to atomistically simulate physical processes that take place in microseconds.

In 1993, Koelman et al. introduced Dissipative Particle Dynamics (DPD) that allows computer simulations in mesoscale of length and time. [168] DPD enables to simulate mesoscale molecules is mesoscopic time and length scale due to the coarse graining approach it uses. Similar MD, DPD integrates equation of motion, but instead of atoms, it solves the equation for "beads" in a given mass and size. The bead represents a cluster of atoms and its motion is assumed to obey Newton's laws. However, due to coarse graining of sets of atoms into beads, atomic information is lost in DPD. An important advantage of DPD over MD is that the time steps are much larger; therefore simulation times are significantly shorter. One of the main objectives in DPD is to determine the phase behavior of polymers.

There are different force definitions between bead pairs in DPD; a harmonic conservative interaction, dissipative force and random force. A dissipative force represents a viscous drag between moving beads, while in random force; energy input into the system is maintained. In all force definitions, number of beads and linear momentum is conserved.

Integrating equations of motion for the beads through the phase space of the system generates the trajectory in DPD. The thermodynamic observables such as density fields, order parameters, correlation functions, stress tensor. In order to construct a better understanding on DPD theory, Flory-Huggins theory of polymer solutions [169] is discussed in detail in the following subsection.

3.1.2.1 Flory-Huggins Theory

Flory-Huggins theory is remarkable in the sense that it is able to explain all the phase behavior of polymers using a simple parameter of *Flory-Huggins Interaction Parameter*, χ. This parameter is experimentally obtained, and available in the literature for majority of polymers. DPD theory compares DPD parameter to Flory-Huggins interaction parameter. This way, it is possible to calculate DPD parameter from χ of simple polymer solutions, and the link it to more complex systems.

In Flory-Huggins theory, polymer solutions are considered as polymer is distributed over lattice series N_0 of solvent molecules

Equation 15
$$N_0 = N_s + N_p r$$

where N_s and N_p represents number of solvent molecules and number of polymer molecules with r repeating units. For simplicity, polymer is considered to be composed of two components of A and B. Thus, in polymer lattice N_p, chain A occupies lattice series of N_{pA}, while chain B occupies N_{pB}. The polymer lattice is completely packed with A and B, therefore the volume fractions of A (φ_A) and B (φ_B) adds up to $\varphi_A + \varphi_B = 1$. This way, the free energy of mixing of two components ΔF at constant temperature can be written as

Equation 16
$$\frac{\Delta F}{k_B T} = \frac{\phi_A}{N_A} ln\phi_A + \frac{\phi_B}{N_B} ln\phi_B + \chi\phi_A\phi_B$$

The first two terms in the free energy equation are the entropic terms component in mixing. These two terms makes negative contribution to the equation, indicating that mixing is always entropically favorable. The third term is the energy component. Since the entropy terms are constant, the main factor in determining the favorability of mixing is the χ parameter. Therefore, the large values of χ creates phase mixing of components, while small and negative values of χ favors mixing.

Groot and Warren make the connection between DPD and Flory-Huggins Theory. [170] They have set a range of parameters in DPD and made a connection between these parameters and χ of Flory-Huggins' by using the quadratic equation of free energy density in DPD:

Equation 17
$$\frac{f_V}{k_B T} = \frac{\rho}{N} ln\rho - \frac{\rho}{N} + \frac{\alpha}{k_B T} a\rho^2$$

where ρ is the density, α is the interaction parameter, α is a constant, and N is the chain length (Groot and Warren considered N=1). Comparing this expression with the Flory-Huggins free energy-of-mixing (Equation 16) Groot and Warren made the identity

Equation 18
$$\chi = \frac{\alpha}{k_B T} \rho \Delta a$$

where $\Delta a = a_{AB} - (a_{AA} + a_{BB})/2$, with A and B representing two components in the simulation. Groot and Warren performed several DPD simulations to find the α. For this purpose, they prepared simulation boxes that are phase-separated and with two phases rich in A and B. Assuming all the component have the same compressibility, they confirmed a linear relationship between α and χ at a density of 3.0 and 5.0.

Equation 19
$$\alpha_{(\rho=3)} = 25 + 3.25\,\chi$$

$$\alpha_{(\rho=5)} = 15 + 1.45\,\chi$$

3.1.2.2 Scaling in DPD

Instead of using atomistic information, DPD deals with beads that represent a set of atoms. The beads defined in DPD have the same mass m, velocity v, and the interaction radius r_c. This allows to introduce a reduced set of units where the interaction radius and bead mass are the units of length and mass. In addition to these, since beads share the same velocity at constant temperature, it is logical to use the thermal energy, $k_b T$ as the energy reference, E_{ref}. The rest of the units are derived from these three. For instance;

$$Force = {E_{ref}}/{r_c}$$

$$time = r_c \sqrt{{(m}/{E_{ref}}}$$

$$Pressure = {E_{ref}}/{r_c^3}$$

To compare a DPD result to an atomistic simulation, one needs to convert reduced units into physical units. The reduced length unit in DPD, r', is converted to physical units as follows:

Equation 20
$$r = \frac{r'}{r_c}$$

Similarly, time t_r in reduced units is converted to physical as follows:

Equation 21
$$t = t_r r_c \sqrt{m/E_{ref}}$$

with a time unit of $r_c \sqrt{m/E_{ref}} = 0.005 \, ns$. The typical values used in for reduced units are

$$m = 0.1 \, kgmol^{-1}$$

$$E_{ref} = 2478 \, Jmol^{-1}$$

$$r_c = 0.8 \, nm$$

The DPD forcefield employed in this study uses these values in physical units conversion.

4.2 Materials and Methods

4.2.3 Single Chain All-Atom MD Simulations of PEO

Single chain MD simulations were carried out for varying chain lengths from 10 to 200 repeat units in 1:6.25 THF:DMF mixtures. For this purpose, several boxes were created containing a single chain of PEO and a total of 500 solvent molecules (Table 7). Single chain polymers were obtained using the Homopolymer Building Tool of Materials Studio 6.0 package.[171] Polymer chains were then solvated by creating simulation boxes using the Amorphous Cell construction tool.[172] Fixing the density to 1 g/cc, energy minimization was carried out using *COMPASS27* (Condensed-phase Optimized Molecular Potentials for Atomistic Simulation Studies) Forcefield [173], where long range interactions were calculated using Ewald summation and van der Waals

interactions were truncated with a cutoff distance of 12.5 Å. Systems were initially subjected to 2 ns canonical ensemble (NVT) simulations for energy refinement. Isothermal-isobaric ensemble (NPT) MD simulations were then carried out at a pressure of 1 atm and a temperature of 300 K. Andersen-Berendsen thermostat-barostat was employed[174, 175] to maintain the temperature and pressure at the desired values. All analyses were carried out after discarding the first 2 ns of the NPT simulations. Calculation details are provided in Appendix B.

Table 7 Compositions of single and multi-chain PEO MD and DPD models employed in this study*

| Chain length (m.u)*** | MD | | | DPD | | | | | |
| | Single Chain* | | | Single Chain | | | Multiple Chain | | |
	Cubic Box Edge Length (Å)	Equilibration NVT MD duration (ns)	Projection NPT MD duration (ns)	Number of PEO Beads	Number of Solvent Beads	Cubic Box Edge Length (Å)	Number of PEO Beads	Number of Solvent Beads**	Cubic Box Edge Length (Å)
10	38.27	2	5	5	45	20.40	105	927	56.00
20	38.44	2	5	10	90	26.00	160	1383	56.32
40	38.77	2	5	20	180	32.40	220	1970	70.40
60	39.01	2	7	30	270	37.20	420	3595	80.40
80	39.40	2	7	40	360	40.80	520	4676	88.04
100	39.72	2	7	50	450	44.00	550	4666	94.80
200	41.21	2	10	100	900	56.00	1100	9113	120.0

Number of solvent molecules is 500 in all MD systems. The complex solvent system of THF:DMF 1:6.25 is employed in all the MD calculations.

** *The complex solvent system of THF:DMF 1:6.25 is employed in all the DPD calculations.*

*** *m.u: monomeric units (1 unit of ethylene oxide)*

4.2.4 DPD Parameterization

DPD simulations start with constructing beads and parameterizing bead-bead interactions. For this purpose, PEO chains with varying chain lengths were mapped onto beads. Along with

solvent molecules, polymer chains were partitioned into beads composed of chemically distinct units with similar sizes.

Following the well-established procedure described in previous studies,[155, 176] DPD parameters of beads were derived by calculating Hildebrand solubility parameter (δ) and Flory-Huggins interaction parameter (χ). δ was calculated by, [177]

Equation 22

$$\delta = \sqrt{\frac{E_{coh}}{V}} = \sqrt{CED}$$

where E_{coh} and CED correspond to cohesive energy and cohesive energy density, respectively. Once δ values were obtained, χ parameters of the beads were calculated from, [178]

Equation 23

$$\chi_{ij} = \frac{V_m}{K_B T}\left(\delta_i - \delta_j\right)^2$$

Where V_m Stands for molecular volumes of the beads calculated by ACDLabs/Chemsketch.[179] To calculate δ and χ, successive MD simulations were carried out where a 1 ps equilibration step followed by 100 ps NVT ensemble was applied to simulation boxes containing molecules with 10 beads of the same type. Densities of simulation boxes were fixed at 1.0 g/cc in case of PEO; 0.89 and 0.94 g/cc for THF and DMF, respectively. Cohesive energy densities and solubility parameters were calculated from MD trajectories using CED calculation tool of the Forcite module of the Materials Studio 6.0 package. DPD interaction parameters (a_{ij}) were then calculated using the linear relationship,

Equation 24

$$a_{ij} \approx a_{ii} + 3.25\chi_{ij}$$

where $a_{ii} = 25k_B T$ for a box density of 3 DPD units[170]. Like PEO and solvents, HS was also partitioned into beads of similar sizes with the rest of the beads. Partitioned HS units, along with

PEO beads are shown in Figure 25-a-b. For HS beads B and C, effect of side chains on DPD parameters was also investigated. To do this, four different bead types; B, B', C, C' were prepared and DPD parameters were calculated for each type. Here, B' and C' are chemical derivatives of B and C; *i.e.* B, B', C, C' are cyclohexane, methylcyclohexane, 1,6-hexanediamine and 2-metyhl-1,6-hexanediamine, respectively. Table 8 summarizes the interaction and DPD parameters calculated according to equations 1-3. No significant difference was observed between DPD parameters calculated using C and C' (0.13%), a negligible difference was observed between DPD parameters calculated using B and B' (2.5%). Therefore, further calculations were carried out by removing side chains from the beads.

4.2.5 DPD Simulations

For DPD studies, each cubic box was formed with a density of 3 DPD units. The box size and number of beads varied so that the system contains 10% of polymer and 90% solvent beads. A 20000 steps DPD equilibration followed by 100000 steps of production DPD was produced with a spring constant of 4.0; the temperature was set to unity. DPD simulations were carried out on three different types of systems. The first is comprised of only single chains the soft segment polymer (PEO) of varying chain lengths; these simulations were carried out to directly compare with all-atom (AA) MD simulation results for the corresponding systems. Summary of single chain DPD parameters are listed in Table 7. In the second set, DPD simulations multiple chains of soft segment PEO were carried out, providing the correlation coefficient between single and multiple chain DPD simulations. In the third set, full polymer DPD studies were carried out by adding hard segment beads (shown in Figure 25-b) to the ends of PEO chains of varying length. For PEO chains in three different lengths, 46, 106 and 182, HS beads were added so as to form 30% of the full polymer. Number of hard segment units added to PEO molecules of 46, 106 and 182 in length were 2, 4 and 6, respectively. A summary of the latter systems studied by DPD is listed in Table 9. Details of the DPD parameters are given in Appendix B.

4.2.6 Fine Graining

Fine graining was carried out to bring the molecular information back to the coarse-grained equilibrated morphologies. For this purpose, a template polymer was prepared containing chemical information for each bead type. Motion groups and centroids were added to this

template polymer based on the beads created for the DPD study. Each polymer chain from the last frame of the DPD trajectory was extracted and recorded as isolated polymers. Details of prepared template molecule are displayed in Figure 25-c. A script prepared by *Marrink et al.*[180] was employed to convert bead-modeled system to atomic model. Details of the script are given in Appendix B. This script identifies and matches the beads with atomic information provided in the template molecule, and places each centroid to the corresponding bead's coordinate. Once fine graining was completed, the system was further relaxed by short MD simulations.

Table 8 Calculated Flory-Huggins interaction parameters χ_{ij} (lower diagonal) and DPD parameters a_{ij} (upper diagonal) of the beads.

χ_{ij}		PEO	THF	DMF	A	B	C	B'	C'	a_{ij}
	PEO		29.89	25.17	25.74	31.86	25.28	30.06	25.16	
	THF	1.50		27.95	31.97	25.02	28.69	25.01	28.82	
	DMF	0.05	0.90		26.34	29.33	25.00	28.02	25.00	
	A	0.23	2.13	0.41		35.36	27.05	32.89	26.59	
	B	2.10	0.01	1.32	3.17		30.35	-	30.35	
	C	0.09	1.13	1.03E-3	0.63	1.64		28.62	-	
	B'	1.55	4.14E-3	0.92	2.41	-	1.11		-	
	C'	0.05	1.17	9.62E-4	0.49	1.64	-	-		

Table 9 Compositions of DPD models used in copolymer calculations

SS length (m.u.)	Number of SS Beads	Number of HS beads	Number of Chains	Number of Solvent beads**	Cubic Box Edge Length (Å)
46	230	180	10	3690	70.80
106	530	380	10	8190	116.4
182	910	580	10	13410	135.4

*m.u: monomeric units (1 unit of ethylene oxide), ** Total number of solvent mixture of THF:DMF (1:6.25)*
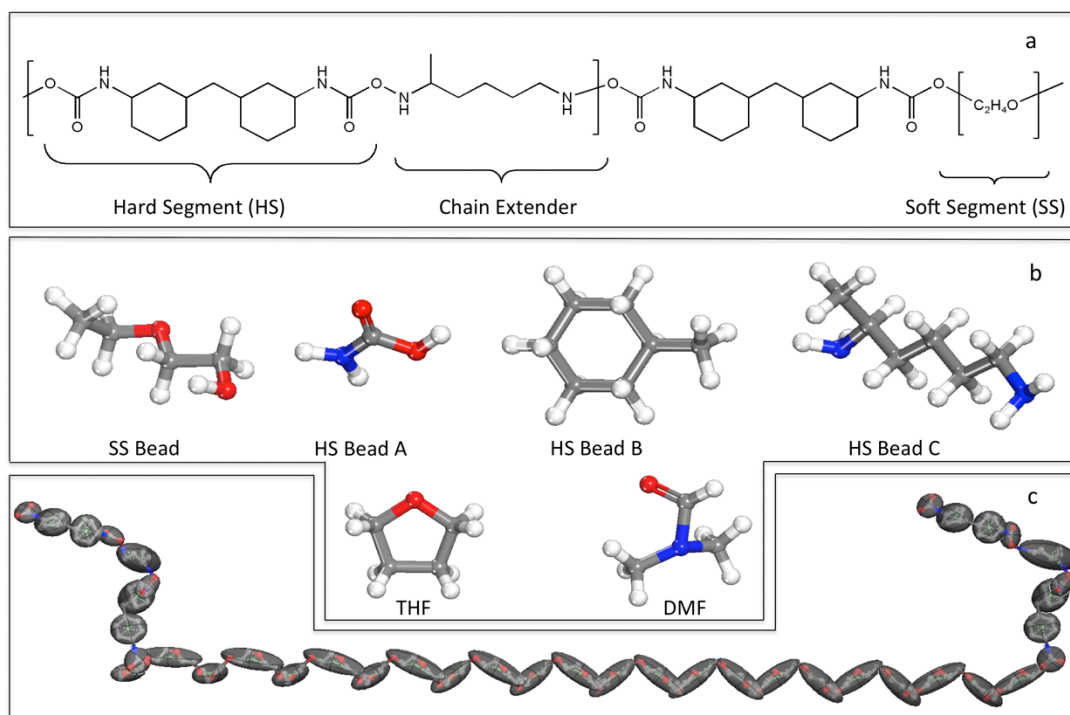
Figure 25 (a) Two dimensional chemical structure of PEO based poly(urethane urea) copolymer. Segments of copolymer are defined as HS, chain extender and SS. (b) Three-dimensional chemical structures of partitioned beads of copolymer for DPD simulations. Carbon, oxygen, nitrogen and hydrogen atoms are represented in gray, red, blue and white, respectively. (c) Template polymer prepared for fine graining. Motion groups and centroids added on template polymer are displayed in gray and green, respectively.

4.2.7 Synthesis of Poly(ethylene oxide) based Poly(urethane-urea) Copolymers

Poly(ethylene oxide) glycol oligomers (PEO) with $<M_n>$ values of 2000, 4600 and 8000 g/mol were purchased from Merck to synthesize PEO46-, 106- and 182-copolymer, respectively. Bis(4-isocyanatocyclohexyl)methane (HMDI) was provided by Bayer and had a purity better than 99.5%. The chain extender 2-methyl-1,5-diaminopentane (MDAP) was supplied by DuPont. Dibutyltin dilaurate (DBTDL) was obtained from Witco and was used as a catalyst by diluting to 1% by weight in tetrahydrofuran. Reagent grade 2-propanol (IPA), tetrahydrofuran (THF) and dimethylformamide (DMF) were obtained from Merck. All chemicals were used as received. The synthesis of segmented polyurethane-ureas followed the general procedures rely on the two-step polymerization technique widely reported in the literature[115].

4.2.8 Atomic Force Microscopy (AFM) Studies

For AFM imaging, atomically smooth silicon wafers were used as substrates. A stock solution of each polymer with a concentration of 10% in THF/DMF as obtained from the synthesis was diluted by a factor of 1:100 using the same binary solvent system. Two different sets of experiments were performed to provide structural insight into the materials with respect to the applied processing conditions. In the first set, a droplet was deposited on the substrate surface from the dilute solution of each polymer to investigate the morphologies developed under low-shear and/or steady state conditions. In this case, great care was shown to avoid shearing of the polymer solutions. Each sample was kept at ambient temperature in a fume hood and subsequently dried in an air oven at 100°C for 24 hours. Then, they were cooled to the room temperature and kept in sealed boxes for 24 hours before measurements. In the second set, we aimed to understand the effect of shear on the morphology developments of the materials. Thus, the samples were prepared by spin coating using the same stock solutions under high-shear conditions. The samples were subjected to the same drying protocol used in the preparation of drop-cast samples as summarized above.

For all set of measurements, height and phase images were captured on a Bruker ScanAsyst enabled Multimode-8 Atomic Force Microscope equipped with a Nanoscope 8.1 controller. All samples were analyzed in standard tapping/non-contact mode by using a Bruker ScanAsyst Air probe with a nominal spring constant of 0.4 N/m, resonance frequency of 70 kHz and a radius of

curvature of 2 nm. Tip specifications and further details of the probes are available at http://www.brukerafmprobes.com/p-3726-scanasyst-air.aspx. All images were recorded at 1 Hz frequency with 512×512 scan and a set point ratio of ~0.6 at ambient temperature and humidity conditions.

4.3 Results and Discussion

4.3.9 All Atom and Coarse-Grained Simulations of PEO Homopolymer Lead to Similar Chain Dimension Scaling

Single chain AA and single-/multi-chain DPD simulations were carried out on a set of PEO oligomers with varying chain length. The $\langle R^2_{end} \rangle^{1/2}$ values obtained from AA and DPD simulations are listed in Table 10 and displayed in Figure 26. We find that $\langle R^2_{end} \rangle^{1/2}$ results obtained from DPD calculations of single PEO chains are in good agreement with those from AA simulations. In addition, a good correlation is observed in $\langle R^2_{end} \rangle^{1/2}$ values (1.07±0.12) of single chain and multiple chain DPD calculations. We note that since equilibration of the AA simulations gets harder as the chain length gets longer, the data points at higher chain lengths have larger uncertainty. The correspondence between the coarse grained and AA results implies that the DPD model used in this study is suitable for studying PEO chains in the complex THF:DMF solvent. Note that, magnitudes of values gathered from MD and DPD results are different from each other due to the fact that DPD calculations use reduced units based on the cutoff distance, bead mass and temperature. Our results are also in conformity with the AA and coarse-grained calculations in previous work.[181, 182]

In characteristic ratio calculations of the mixed solvent systems, we find a decreasing trend in values obtained from both AA and DPD simulations (Table 10), thus displaying a deviation from the usual behavior of C_∞ with an increasing trend that levels off at high enough chain lengths[183]. This decrease is confirmed by Tarazona *et al.*[184] By viscosity measurements in several solvents, it was experimentally observed that a change in Coulombic forces governed by dielectric constant of the solvent gives rise to a change in molecular dimensions of the polymer chains. In that case, we can conclude that both single chain MDs and multi chain DPDs suggested an unusual trend in C_∞, which may be attributed to complex solvent system.
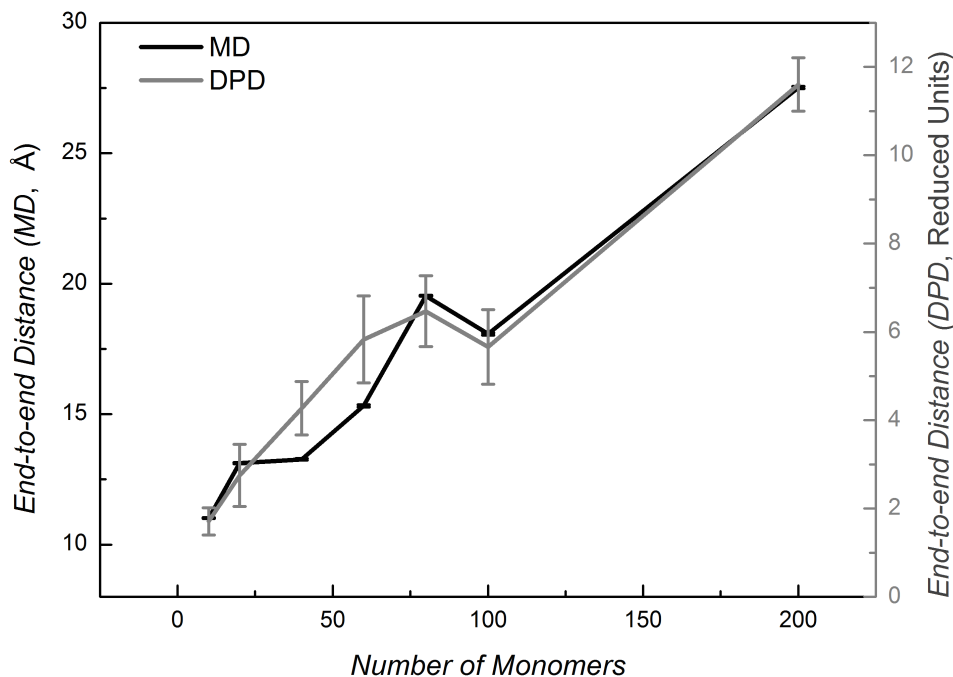
Figure 26 $\langle R^2_{end}\rangle^{1/2}$ comparison of single chain AA and DPD simulations of PEO in chain sizes ranging from 10-200. Data points representing AA and DPD simulations are shown in black and gray, respectively.

4.3.10 PEO Based Segmented Poly(urethane urea) Copolymers Self Organize into Channels at Low SS Lengths

The morphologies obtained from 100000 steps of DPD simulations are displayed in Figure 27. Overall conformations of soft segments of copolymers were obtained using the MesoCite tool. The density fields are those of the ethylene oxide segment only. It is observed that copolymers show different morphological traits in pure DMF, pure THF or in the THF/DMF mixture (Figure 27, red morphologies). Copolymers with longer soft segments, i.e. PEO106- and PEO182-copolymer, tend to form granular structures. On the other hand, isosurfaces around the soft segment of PEO46-copolymer form channels between solvent molecules. In addition, channel formation is only observed when the complex solvent system employed.

Table 10 Overall results of all MD and multi-chain DPD simulations carried out in this study.

		$\langle R^2_{end} \rangle^{1/2}$			C_∞		
		Single Chain		Multi-Chain	Single Chain		Multi-Chain
Number of Monomers		all atom (Å)	DPD (DPD Units)	DPD (DPD Units)	all atom (Å)	DPD (DPD Units)	DPD (DPD Units)
PEO	10	11.02	1.71	1.97	2.75	0.58	0.78
	20	13.13	2.75	2.92	1.95	0.76	0.85
	40	13.27	4.27	4.09	1.00	0.91	0.84
	60	15.32	5.83	5.84	0.89	1.13	1.14
	80	19.54	6.47	6.93	1.08	1.05	1.20
	100	18.08	5.66	7.39	0.74	0.64	1.09
	200	27.52	11.6	11.0	0.86	1.35	1.22
Copolymer	46	-	-	4.91	-	-	1.05
	106	-	-	7.25	-	-	0.99
	182	-	-	11.5	-	-	1.46
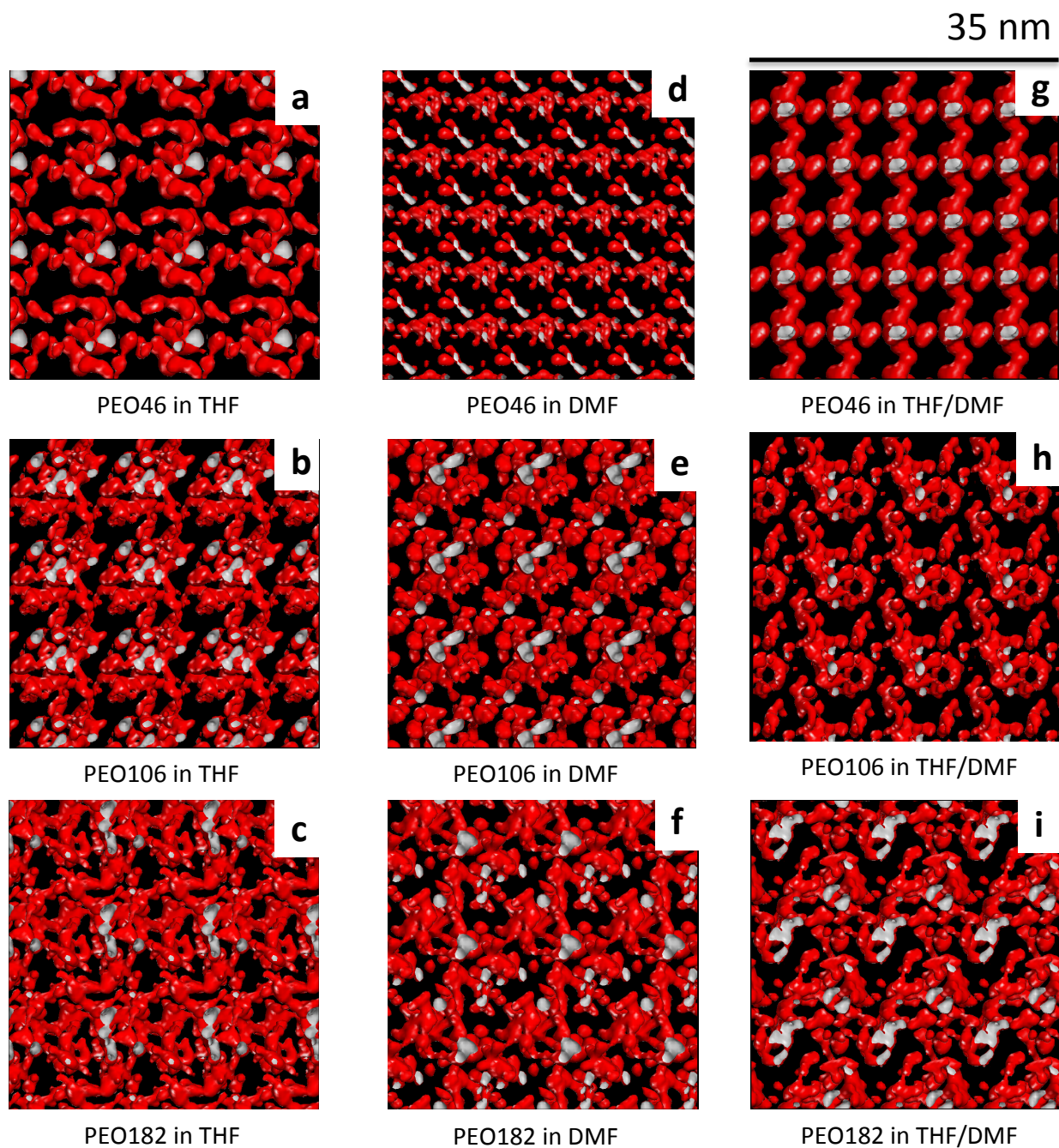
Figure 27 Density field profiles of PEO46-, PEO106- and PEO182-copolymer's soft segments in pure solvents THF (a, b, c), DMF (d, e, f) and solvent mixture of THF:DMF 1:6.25 (g, h, i). Soft segment density fields are demonstrated in red. Density fields are displayed for the soft segments and solvent molecules were turned off for better visualization. Periodic images were expanded to 3.5 nm.

35 nm

PEO46 shear 0.01

PEO46 shear 0.1

PEO106 shear 0.01

PEO106 shear 0.1

PEO182 shear 0.01
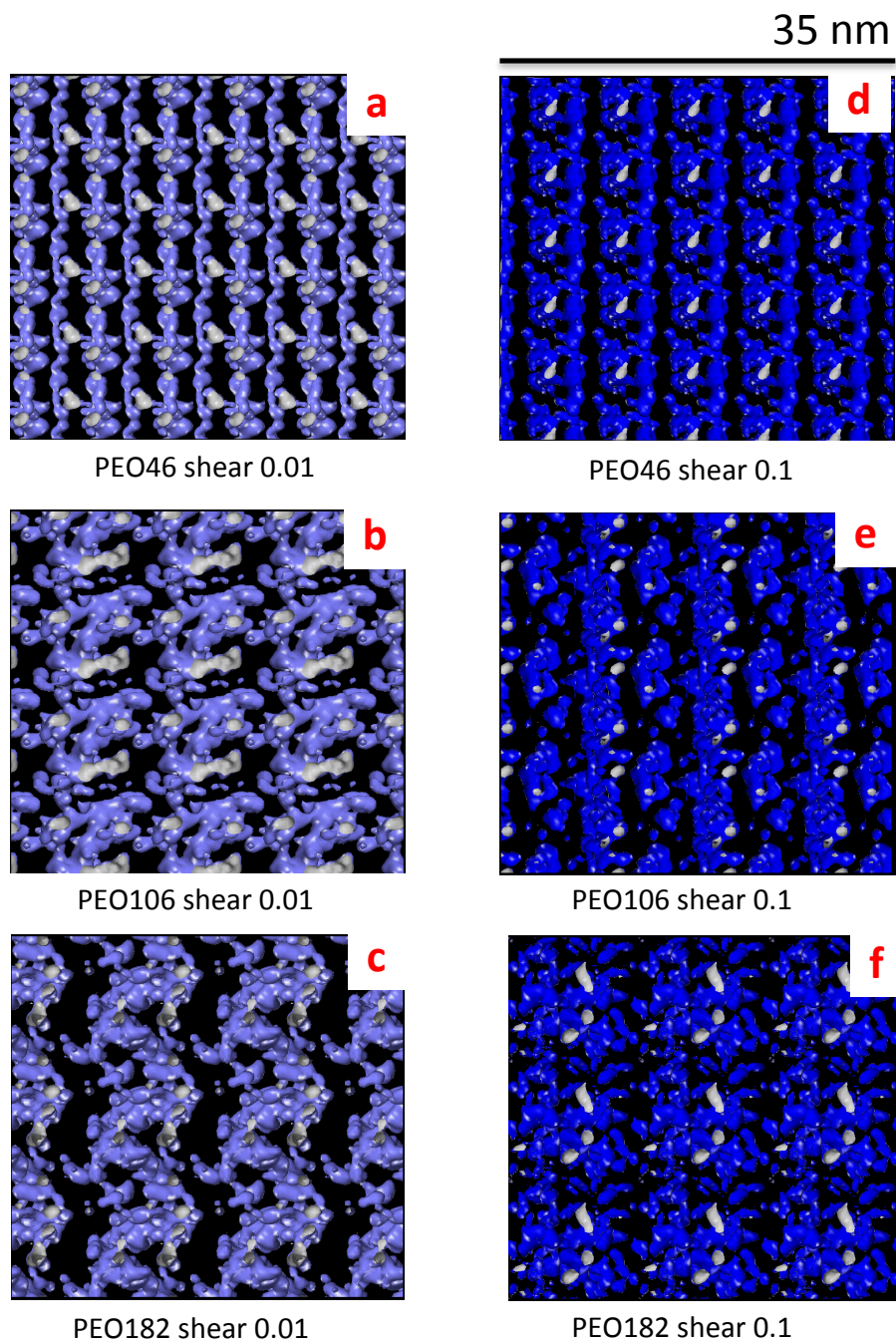
PEO182 shear 0.1

Figure 28 Density field profiles of PEO46-, PEO106- and PEO182-copolymer's soft segments under low shear of 0.01 DPD units (a, b, c) and high shear of 0.1 DPD units (d, e, f). Soft segment density fields are demonstrated in purple (shear 0.01) and blue (shear 0.1). Density fields are displayed for the soft segments and solvent molecules were turned off for better visualization. Periodic images were expanded to 3.5 nm.

To test the stability of the morphologies in the mixed solvents, we have sheared each of these systems at different rates. The modified density fields under stress are displayed in Figure 28. We find that channel formation in the PEO46-copolymer soft segment is stable under both shear rates applied. On the other hand, PEO106- and PEO182-copolymer organize into an ordered structure under different shear rates applied, i.e., the equilibrium structures of PEO106-copolymer and PEO182-copolymer are not stable under shear. These results proposed that PEO46-copolymer should display similar morphological features under both non-sheared and sheared conditions. In contrast, the other two copolymers may exhibit different morphologies with respect to applied processing conditions. As the structure-property behavior of such materials strongly depend on the preparation conditions determining the final morphologies, we believe that experimental validation of our computational results can provide significant insight into the key mechanisms behind the morphology development in these copolymers. For this reason, AFM studies of the copolymers have performed as given in the following section.

4.3.11 AFM Studies of the Corroborate Chain-Length Dependent Morphologies and Stability of the co-Oligomers

AFM is a powerful experimental tool to examine the morphologies of such complex materials. To correlate the results obtained from the DPD simulations under both non-sheared and sheared conditions, we have obtained AFM images of the corresponding systems. In comparing with the DPD morphologies, we note that the edge length of cubic boxes that are in DPD units are converted to ångström multiplying by interaction distance of 8 Å.[185] Representative phase images of the non-sheared and sheared samples are presented in Figures 29 and 30, respectively. As shown in Figure 29, AFM phase morphologies of the non-sheared samples are in accordance with the results obtained from the DPD simulations for all the copolymers under steady-state conditions. PEO46-copolymer (Figure 29-a) preserves similar channel-like structures, which were obtained from the DPD simulations, at a higher length scale. On the other hand, the irregular bead-like structures observed in the DPD simulations of the PEO106- and PEO182-copolymer were recorded as randomly packed bead-like structures at a higher length scale as demonstrated by their AFM studies at equilibrium (Figures 29-b and 29-c, respectively).

The results obtained from the AFM and DPD studies based on the copolymer morphologies are also in good agreement for the sheared samples. As emphasized in DPD section, the PEO46-copolymer preserves the channel-like structure under the applied shear conditions as shown in Figure 30-a. For this copolymer, the AFM phase morphologies observed under non-sheared and sheared conditions are similar to each other (Figures 29-a and 30-a). On the other hand, the randomly packed bead-like structures in the PEO106- and PEO182- copolymer (Figure 29-b and 29-c) turn into oriented "beads on a string" like fibrillar structures under the applied shear conditions as shown in Figures 30-b and 30-c, respectively. These results are also in accord with the shear-induced morphologies obtained from the DPD simulations. Thus, the AFM studies experimentally validate the results obtained from the DPD simulations. As the chain length of PEO106 particularly corresponds to the critical entanglement chain length of PEO,[186] these results also suggest that this value (critical entanglement chain length) should be considered as a significant parameter for the selection of PEO oligomers as soft segments during the synthesis of PEO-based segmented polyurethane-urea copolymers. To the best of our knowledge, the importance of this key parameter has not yet been reported in the extensive polyurethane literature. As demonstrated by DPD and AFM studies, here we report that the copolymers with PEO soft segments having chain lengths higher than the critical value display significantly different structure-morphology-property relationships depending on the preparation conditions. On the contrary, those with PEO soft segment having a chain length lower than the critical value show similar structure-morphology-property behavior, independent of the preparation conditions.

4.3.12 Hydrogen Bond Formation between Urethane-PEO Groups Derives Channel Formation

To understand the reason behind the channel formation observed in copolymer with PEO46, radial distribution functions (RDFs) were plotted for each type of beads in copolymer structure. Figure 31 shows the RDFs of all HS-HS, SS-SS, HS-SS and PEO-solvent interactions.

Investigating the HS-HS interactions (Figure 31-a), no correlation is observed between chain length and HS-HS interaction probability. But since HS-HS interactions are primarily responsible of polymer's hard segment conformation and indirectly affect soft segment, we focused our
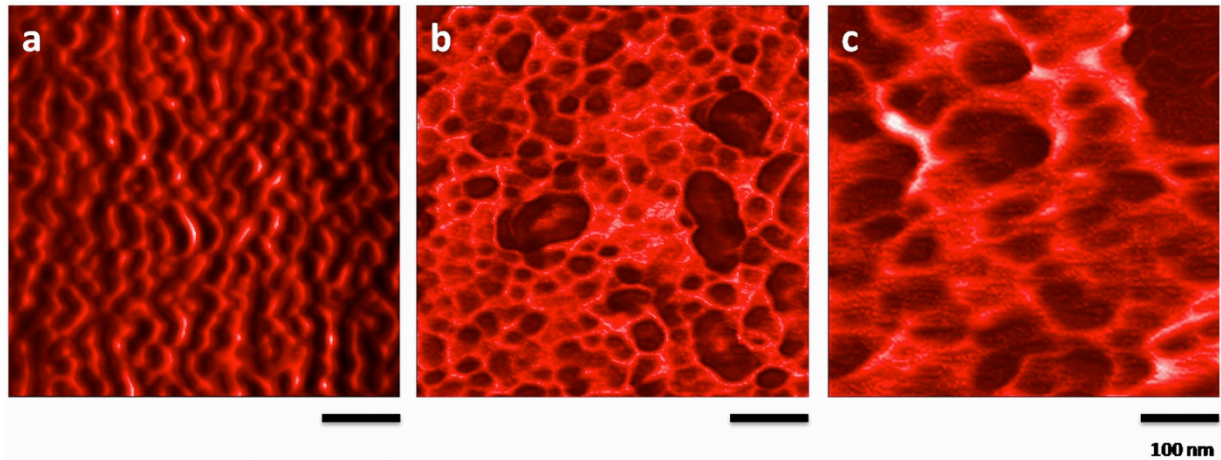
Figure 29 AFM phase images of non-sheared PEO46-copolymer (a), PEO106-copolymer (b) and PEO182-copolymer (c). AFM samples were prepared by polymer casting method.
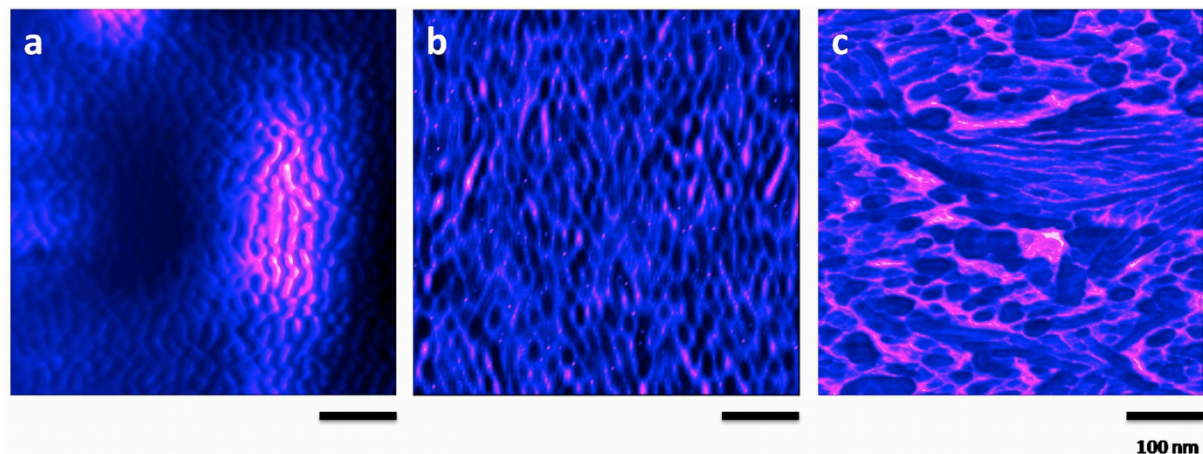
Figure 30 AFM phase images of sheared PEO46-copolymer (a), PEO106-copolymer (b) and PEO182-copolymer (c). AFM samples were prepared by spin-coating method.

investigation on HS-SS and SS-SS interactions. As the copolymer chain length is increased, both SS-SS and HS-SS interactions are weakened (Figure 31-b-c). It is also observed that HS-SS interactions in PEO46 are significantly stronger than PEO106 and PEO182. To understand this difference, we extended our investigation into bead basis.

85
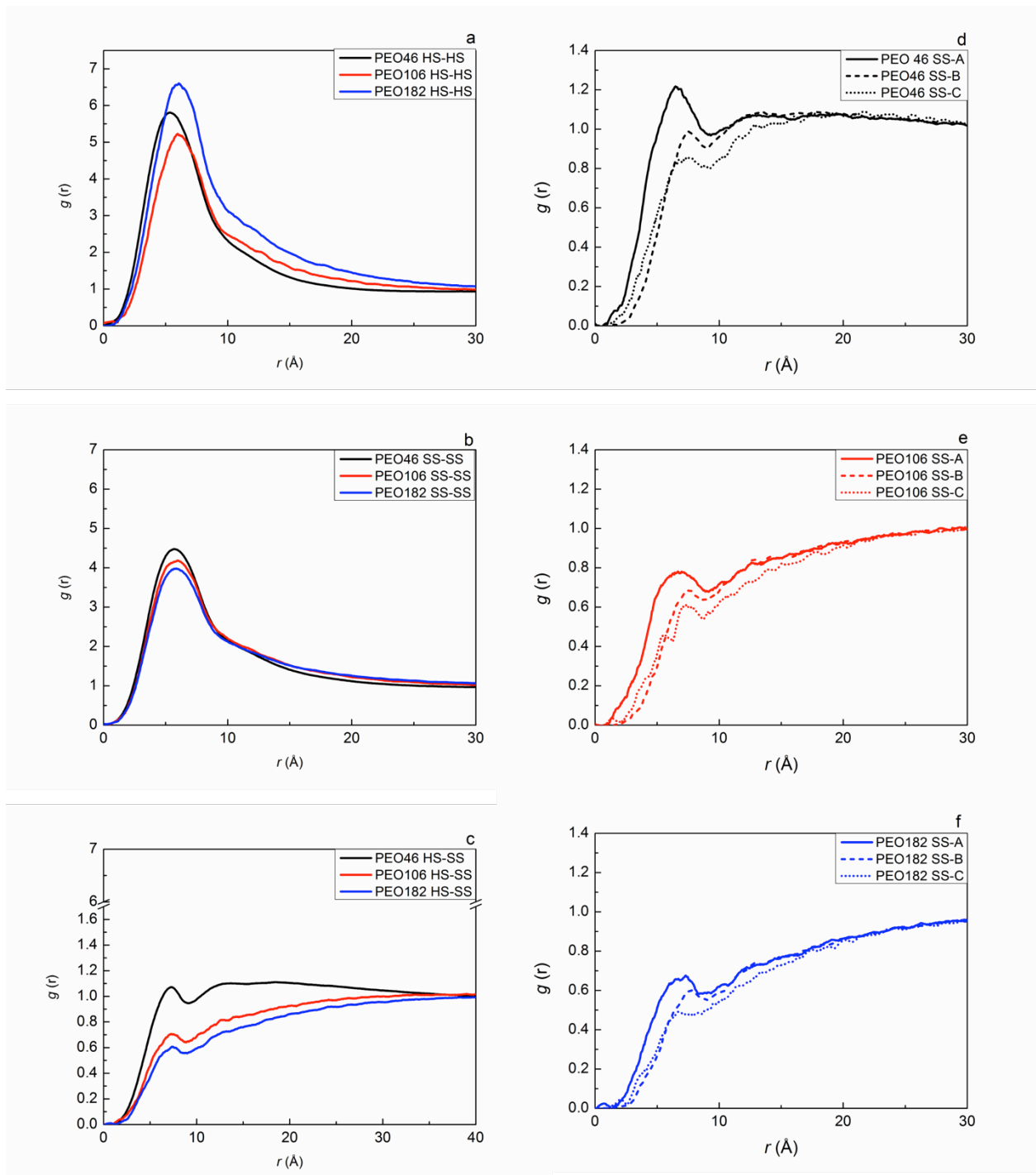
Figure 31 Radial distribution functions (RDFs) plotted for each type of beads in copolymer structure. (a-c) RDFs of HS beads vs. SS of PEO46-, 106- and 182-copolymer are demonstrated in black, red and blue, respectively. (d-f) RDFs of copolymer SS vs. bead A, B, and C are demonstrated in line, dash and dot, respectively.
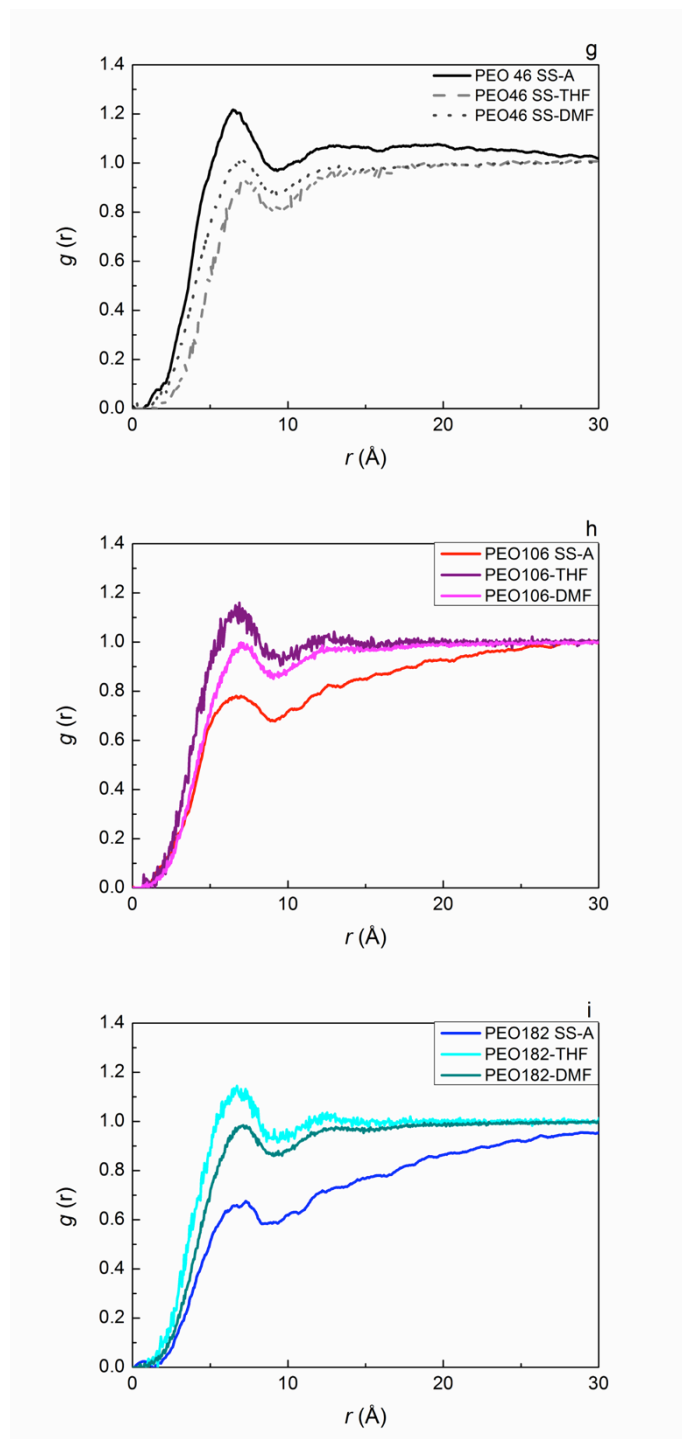
Figure 31 (cont.d) (g) RDFs of PEO46-copolymer SS vs. bead A, THF and DMF are demonstrated in black, dark gray and light gray, respectively. (h) RDFs of PEO106-copolymer SS vs. bead A, THF and DMF are demonstrated in red, purple and magenta, respectively. (i) RDFs of PEO182-copolymer SS vs. bead A, THF and DMF are demonstrated in blue, cyan and green, respectively.

Comparing the HS bead interactions with SS for all copolymers, A-type hard segment beads were found to be closest to soft segment (Figure 31-d-f; black). This directed us to the idea that A-type beads might form secondary interactions with soft segment, thus affecting the conformation of soft segment. Considering the probability of A-type beads to be close to soft segment is the highest in PEO46 (Figure 31-d; black) compared to PEO106 and 182 (Figure 31-e-f; black), it can be concluded that A-type beads regulate the channel-like morphology observed in copolymer with PEO46.

To decide whether PEO-solvent or PEO-urea interactions were more dominant in channel formation, radial distribution functions of soft segment was plotted against hard segment bead A and solvents (Figure 31-g-i). It was observed that, unlike longer copolymers, SS of PEO46 resulted in a higher probability of interaction with A-type bead than that of solvents. In other words, urea/urethane molecules were in higher probability of being around soft segment, rather than solvent molecules. This indicated that interactions between soft segment and urea are the main reason behind channel formation.

4.3.13 Reverse-Mapped Structures Reproduced the Channel-Like Morphology

We have next reverse-mapped the atomistic details on the PEO46-copolymer system to determine which atomistic interactions dominate the channel formation. Reverse mapping[180] was carried out for each polymer molecule and solvent type separately. Polymer chains were then brought together to form the original structure. Once fine graining was successfully completed, the system was further relaxed by energy minimization followed by 120 ps long NVT-MD simulations. The last frame of the DPD trajectory for the PEO46-copolymer, along with the fine-grained model is displayed in Figure 32-a-b. Density field calculations of the reverse mapped structure reproduces the channel-like morphology observed in DPD (the reverse mapped model and density fields generated from it are displayed in Figure 32-c-d). The reverse mapped structures of PEO46-copolymer supports the idea that A-type beads, namely urethane, form hydrogen bonds with soft segments, i.e. between carbonyl groups in the hard segments and ether oxygen groups in the soft segments. Hydrogen bonds formed between urethane and PEO groups are exemplified in

Figure 33. These include those between HS-HS and HS-SS is labeled with cyan and green, respectively. Here, a hydrogen bond is defined if the distance between donor and acceptor heavy atoms is less than 4 Å.
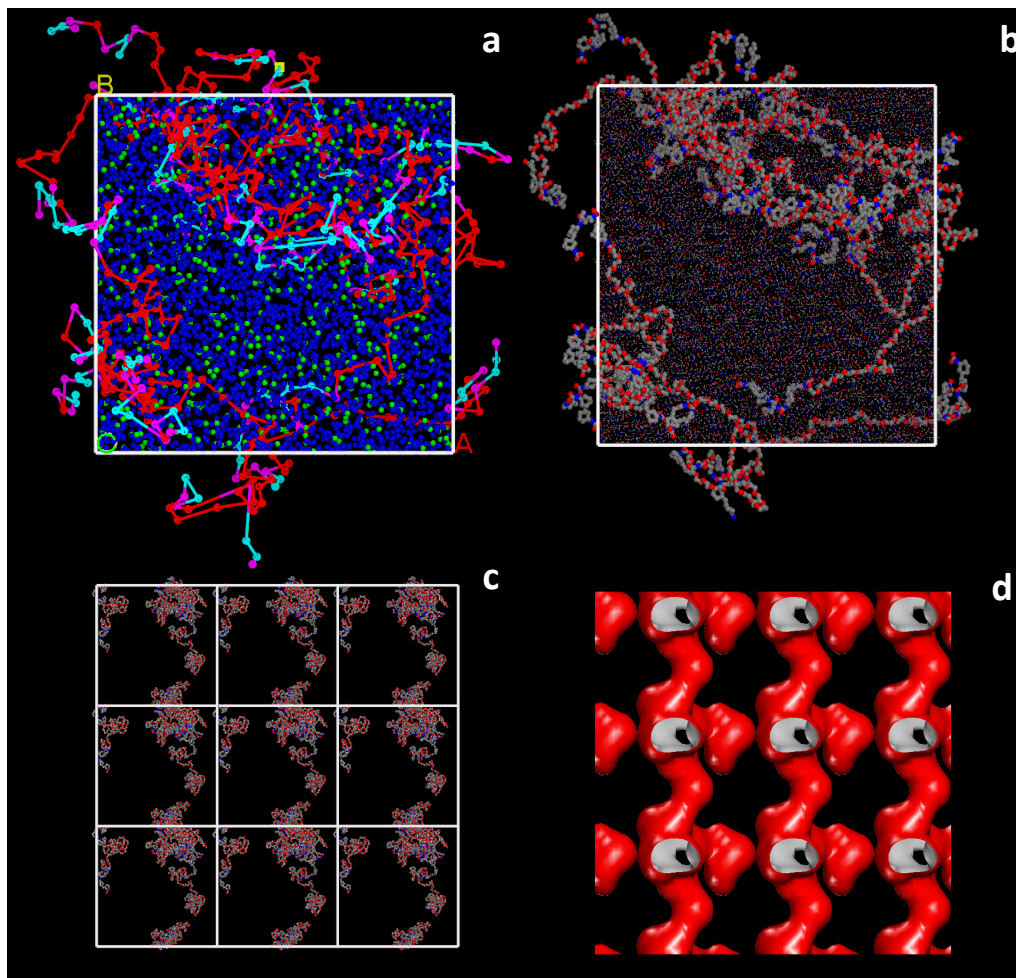
Figure 32 (a) Last snapshot from the DPD trajectory. PEO, HS bead A, B, C THF and DMF beads are represented in red, purple, cyan, pink, green and blue, respectively. (b) Reverse mapped model. (c) 3x3x3 expanded crystal structure of reverse mapped model. Carbon, oxygen, nitrogen and hydrogen atoms are represented in gray, red, blue and white, respectively. (d) 3x3x3 expanded density fields of reverse mapped PEO46 PEO46-copolymer. Density fields were created for soft segments using MesoCite tool. Solvent molecules were turned off for better visualization.
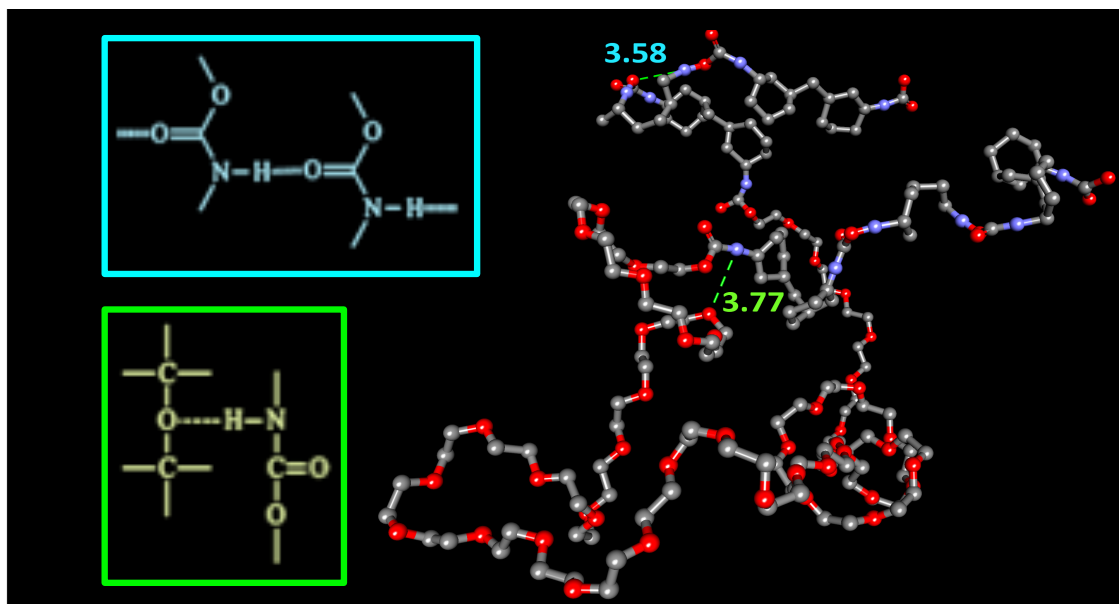
Figure 33 Hydrogen bonds formed between HS-SS molecules of PEO46-copolymer. Inter- and intra-segmental H bonds are labeled in green and cyan, respectively. Carbon, oxygen and nitrogen atoms are represented in gray, red, blue and white, respectively. Hydrogen atoms are turned off for better visualization. 2D representations of inter- and intra-segmental Hydrogen bonds established between HS-SS and HS-HS segments are represented in the inset in green and cyan, respectively.

4.4 Conclusions

This study comprises a multiscale MD & DPD approach to assess the effect of chain length on overall morphology in PEO based segmented poly(urethane urea) copolymers. For this purpose, a three step strategy was employed where in the first step was designed to see the single chain characteristics of the soft segment in a complex solvent system and to test the validity of DPD calculations. Single chain characteristics revealed that $\langle R^2_{end}\rangle^{1/2}$ obtained in MD and DPD are in good agreement and coarse grained DPD model can reproduce conformational preferences of the chains obtained in all atom representation. This result confirms that the properties of much longer and/or multiple chain polymers can be studied with more reasonable computational costs.

Following the single chain soft segment investigations, we have added hard segment beads into PEO soft segment DPD models to examine the effect of chain length on morphology. The models

are prepared as to have soft segment chain lengths of 46, 106 and 182 repeating units that correspond to the oligomers prepared in our labs. Investigating the DPD trajectories of copolymer in terms of density fields, we observe stable channel formations in the PEO46 copolymer in complex solvent system. These channels are neither observed in pure solvents, nor under steady shear, implying that the formations are stable and specific to copolymers with shorter soft segments. Moreover, both AFM and DPD studies suggest that the structure-morphology development, and thus, the properties of PEO46-copolymer, mainly depend on its intrinsic features rather than the preparation conditions. On the other hand, structure-morphology-property relationship is rather dependent on preparation conditions than the intrinsic properties in PEO106- and PEO182-copolymer.

Radial distribution functions of copolymer beads with each other and with solvent reveals that the specific channel formation observed in PEO46 copolymer is not solely depend on polymer-solvent (THF, DMF) interactions, but more on secondary interactions formed between hard segment urethane groups and the soft segment. We showed that there are two competing mechanisms in minimizing the free energy upon quaternary urethane-SS-THF-DMF system. Here, intermolecular interactions between HS and SS regulate the overall morphology in PEO46 copolymer resulting in a phase mixing of homogeneously distributed hard segments in soft segment. On the other hand, intramolecular interactions within SS molecules regulate the morphology in PEO106- and PEO182-copolymers. This leads to phase separation; a cluster formation of soft segments in which hard segment molecules cannot penetrate. This feature is only observed above a critical SS chain length. Conversely, secondary interactions regulate the morphology in copolymers with SS chains below critical lengths. The findings of this study provides significant insight into the fundamental phenomena of microphase separation/mixing in segmented copolymers regulated by thermodynamic control through good/poor solvent duality for the design and synthesis of new materials with diverse functions.

CHAPTER 5 Conclusions

The first hypothesis proposed in this thesis was the validity of freeze concentration method as a useful reaction tool for modification of thermosensitive macromolecules. A model biopolymer was selected to test the method and Michael addition of several organic acids into chitosan backbone was carried out in FC medium. Spectroscopic analysis results revealed solid evidence that Michael addition took place under FC conditions. In addition to that, the solubility of chitosan biopolymer was also increased after Michael addition. Moreover, FC reactions resulted in a decrease in crystallinity of chitosan polymer and this decrease was attributed to the addition of bulkier side chain groups into polymer's backbone. This decrease in crystallinity was also addressed as the reason behind increased solubility since the addition of bulkier side chain groups decreased the regularity of structure by reducing the amount of intermolecular secondary interactions. By a quantitative Cd-ninhydrin test it was shown that the Michael adducts possesses less amount of primary amines in their structure, which is another evidence that the amount of secondary interactions established via H-bonding between amine groups were reduced upon modification. On the other hand, freeze concentration reaction did not have any significant effect on thermal properties of Michael adducts, while morphological properties differ upon freeze concentration reactions. This change can be attributed to the additional stress introduced by ice formation phase during freeze concentration. This study poses the validity of FC method for chemical reactions of macromolecules, especially the thermosensitive materials such as proteins. The effect of modified morphology on mechanical and surface properties can be listed as the future studies on this matter.

The second purpose in this thesis was to develop a chemical nanosensor to detect trace amount of nitroaromatics from environmental samples. To do this, a hybrid nanosensor composed of monolayer graphene and molecularly imprinted polymer was developed and its performance was evaluated. During the fabrication, a novel method of "embedded electrodes" was developed and the metallic contact lines used to measure the change in sheet resistance of graphene were embedded into substrate. TLM measurements revealed that the sensor responds selectively in a

linear region of analyte concentrations between 10-100 ppm, which covers the toxic levels of the nitroaromatic type analyte. In addition, the sensor was sensitive against imprinted analyte, while it did not respond to any other possibly interfering chemicals. Moreover, The noise level of the sensor was very low compared to the signal. Comparing the developed sensor with the literature examples of nitroaromatics sensors, it was concluded that the measurement technique employed is very simple and can be applied to on-field measurements of nitroaromatics while other examples usually require heavy instrumentation and a laboratory environment to read the signal. Further to that, the noise level and the detection limit of developed sensor is acceptable considering the fact that the active layer is a polymeric thin film.

In the third part of the thesis, a multiscale computational approach was employed to investigate the structure-morphology-property relationship of PEO based segmented poly(urethane-urea) copolymers. For this purpose, MD, DPD and reverse mapping methods were employed. Results were compared with experimentally obtained AFM images. In the first step, MD and DPD simulations results were compared in terms of end-to-end distances of single chain PEO (SS) models in varying chain lengths. This was done to assess the validity of DPD model. The comparison of MD DPD models revealed that the trend in end-to-end distances with respect to increasing chain lengths of MD and DPD models were similar, therefore the DPD model is able to produce reliable results. In the second step, HS beads were incorporated into SS chains and copolymer models were prepared in 3 different chain lengths; PEO46-, PEO106- and PEO182-copolymer, respectively. DPD simulations of these copolymers were carried out in pure THF, Pure DMF and a mixture of THF:DMF (1:6.25) solvents and density field maps were generated. It was first observed that the morphology of the copolymers differ with respect to solvent used, and a stable channel formation was observed in PEO46-copolymer only when the complex solvent system is employed, while PEO106- and PEO182-copolymers tend to form granular formations in this solvent system. In addition, density field maps generated from DPD trajectories of copolymers were compared to AFM phase images. AFM images of PEO46-copolymer indicated a phase separation of HS and SS segments in PEO106- and PEO182-copolymers, while a phase mixing is observed in PEO46- with similar channel formations in a larger scale. In this respect, AFM images were similar to DPD density fields. Furthermore, to test the stability of the

specific channel formations in PEO46-copolymer, DPD simulations were also carried out under different steady shear rates. Along with AFM images, shear DPDs revealed that the channel formations observed in PEO46-copolymer are stable even under high rates of shear applied, while the morphologies of PEO106- and PEO182-copolymers are distorted with shear application. This lead us to the idea that the dominant factor under morphology formation observed in PEO46-copolymer is due to its intrinsic properties, whereas the morphologies of copolymers with longer chains are dependent on preparation conditions.

To investigate the intrinsic factors affecting the morphology of PEO46-copolymer, radial distribution functions (RDF) of SS beads of copolymers were plotted against HS and solvent beads. RDF plots revealed that, unlike PEO106- and PEO182-copolymer, SS beads of PEO46-copolymer mostly interact with urethane beads of HS. In addition, solvent molecules are found to be in closer contact with PEO46-copolymer than PEO106- and PEo182-. To explain this behavior, we developed the hypothesis of competition of energy minimization mechanisms that is the root of intrinsic properties. The solvent molecules, urethane groups and SS molecules participate in competition and the winner is case dependent. In the first case scenario, SS molecules minimize their energy by forming secondary interactions with each other and form SS granules in which HS and solvent molecules cannot penetrate. This gives rise to a phase separation and is observed only after a specific SS chain length. In the second case, the SS molecules minimize their energy by forming intersegmental secondary interactions with HS molecules; therefore the solvent molecules can penetrate and interact with SS. This situation gives rise to a phase mixing of HS and SS segments and is observed only when the SS chain is short. To prove the hypothesis, reverse mapped models of DPD were investigated. Monitoring the secondary interactions, intersegmental Hydrogen bonds established between urethane groups and SS are only observed in PEO46-copolymer. The hypothesis is proven to be true, and gives us the solid evidence to conclude that the secondary interactions between urethane and SS regulate the phase mixing and separation of HS and SS segments with respect to critical chain length and soft segment chain length controls the unusual macroscopic properties observed in TPUs.

BIBLIOGRAPHY

1.   Kim, S.-K. and N. Rajapakse, *Enzymatic production and biological activities of chitosan oligosaccharides (COS): A review.* Carbohydrate Polymers, 2005. **62**(4): p. 357-368.
2.   Rinaudo, M., *Chitin and chitosan: Properties and applications.* Progress in Polymer Science, 2006. **31**(7): p. 603-632.
3.   Jayakumar, R., et al., *Biomedical applications of chitin and chitosan based nanomaterials—A short review.* Carbohydrate Polymers, 2010. **82**(2): p. 227-232.
4.   Ravi Kumar, M.N.V., *A review of chitin and chitosan applications.* Reactive and Functional Polymers, 2000. **46**(1): p. 1-27.
5.   Pires, C.T.G.V.M.T., J.A.P. Vilela, and C. Airoldi, *The Effect of Chitin Alkaline Deacetylation at Different Condition on Particle Properties.* Procedia Chemistry, 2014. **9**: p. 220-225.
6.   Kafetzopoulos, D., A. Martinou, and V. Bouriotis, *Bioconversion of chitin to chitosan: purification and characterization of chitin deacetylase from Mucor rouxii.* Proceedings of the National Academy of Sciences, 1993. **90**(7): p. 2564-2568.
7.   Rong Huei, C. and H.-D. Hwa, *Effect of molecular weight of chitosan with the same degree of deacetylation on the thermal, mechanical, and permeability properties of the prepared membrane.* Carbohydrate Polymers, 1996. **29**(4): p. 353-358.
8.   Kumar, B.A., M.C. Varadaraj, and R.N. Tharanathan, *Low molecular weight chitosan--preparation with the aid of pepsin, characterization, and its bactericidal activity.* Biomacromolecules, 2007. **8**(2): p. 566-72.
9.   Mogilevskaya, E.L., et al., *The crystal structure of chitin and chitosan.* Polymer Science Series A, 2006. **48**(2): p. 116-123.
10.   Tømmeraas, K., et al., *Preparation and characterisation of oligosaccharides produced by nitrous acid depolymerisation of chitosans.* Carbohydrate Research, 2001. **333**(2): p. 137-144.
11.   Okuyama, K., et al., *Molecular and Crystal Structure of Hydrated Chitosan.* Macromolecules, 1997. **30**(19): p. 5849-5855.
12.   Kurita, K., et al., *N-Alkylation of chitin and some characteristics of the novel derivatives.* Polymer Bulletin, 2002. **48**(2): p. 159-166.
13.   Harish Prashanth, K.V. and R.N. Tharanathan, *Chitin/chitosan: modifications and their unlimited application potential—an overview.* Trends in Food Science & Technology, 2007. **18**(3): p. 117-131.
14.   Jayakumar, R., et al., *Sulfated chitin and chitosan as novel biomaterials.* International Journal of Biological Macromolecules, 2007. **40**(3): p. 175-181.
15.   Sajomsang, W., *Synthetic methods and applications of chitosan containing pyridylmethyl moiety and its quaternized derivatives: A review.* Carbohydrate Polymers, 2010. **80**(3): p. 631-647.
16.   Sashiwa, H., et al., *Chemical Modification of Chitosan. 13. Synthesis of Organosoluble, Palladium Adsorbable, and Biodegradable Chitosan Derivatives toward the Chemical Plating on Plastics.* Biomacromolecules, 2002. **3**(5): p. 1120-1125.

17. Sashiwa, H., et al., *Chemical Modification of Chitosan. 14: Synthesis of Water-Soluble Chitosan Derivatives by Simple Acetylation.* Biomacromolecules, 2002. **3**(5): p. 1126-1128.

18. Sashiwa, H., et al., *Chemical modification of chitosan: preparation of chitosan-sialic acid branched polysaccharide hybrids.* Chemical Communications, 2000(11): p. 909-910.

19. Kurita, Y. and A. Isogai, *Reductive N-alkylation of chitosan with acetone and levulinic acid in aqueous media.* International Journal of Biological Macromolecules, 2010. **47**(2): p. 184-189.

20. Yang, T.-C., C.-C. Chou, and C.-F. Li, *Preparation, water solubility and rheological property of the N-alkylated mono or disaccharide chitosan derivatives.* Food Research International, 2002. **35**(8): p. 707-713.

21. Yang, T.-C., C.-C. Chou, and C.-F. Li, *Antibacterial activity of N-alkylated disaccharide chitosan derivatives.* International Journal of Food Microbiology, 2005. **97**(3): p. 237-245.

22. Bhattarai, N., et al., *PEG-grafted chitosan as an injectable thermosensitive hydrogel for sustained protein release.* Journal of Controlled Release, 2005. **103**(3): p. 609-624.

23. Bobu, E., et al., *Synthesis and characterization of n-alkyl chitosan for papermaking applications.* Cellulose Chemistry and Technology, 2011. **45**(9): p. 619.

24. Morimoto, M., et al., *Synthesis of novel chitosan with chitosan side chains.* Carbohydrate Polymers, 2011. **84**(2): p. 727-731.

25. Ying, G.-q., et al., *Preparation, water solubility and antioxidant activity of branched-chain chitosan derivatives.* Carbohydrate Polymers, 2011. **83**(4): p. 1787-1796.

26. Buranaboripan, W., et al., *Preparation and characterization of polymeric host molecules, β-cyclodextrin linked chitosan derivatives having different linkers.* International Journal of Biological Macromolecules, 2014. **69**: p. 27-34.

27. Ramos, V.M., et al., *Modified chitosan carrying phosphonic and alkyl groups.* Carbohydrate Polymers, 2003. **51**(4): p. 425-429.

28. Zuñiga, A., et al., *Synthesis and characterization of N-propyl-N-methylene phosphonic chitosan derivative.* Carbohydrate Polymers, 2010. **79**(2): p. 475-480.

29. Ngimhuang, J., et al., *Synthesis of a novel polymeric surfactant by reductive N-alkylation of chitosan with 3-O-dodecyl-d-glucose.* Polymer, 2004. **45**(3): p. 837-841.

30. Benediktsdóttir, B.E., et al., *Synthesis of N,N,N-trimethyl chitosan homopolymer and highly substituted N-alkyl-N,N-dimethyl chitosan derivatives with the aid of di-tert-butyldimethylsilyl chitosan.* Carbohydrate Polymers, 2011. **86**(4): p. 1451-1460.

31. Petit, C., S. Reynaud, and J. Desbrieres, *Amphiphilic derivatives of chitosan using microwave irradiation. Toward an eco-friendly process to chitosan derivatives.* Carbohydrate Polymers, 2015. **116**: p. 26-33.

32. Bangde, P.S., R. Jain, and P. Dandekar, *Alternative Approach to Synthesize Methylated Chitosan Using Deep Eutectic Solvents, Biocatalyst and "Green" Methylating Agents.* ACS Sustainable Chemistry & Engineering, 2016. **4**(6): p. 3552-3557.

33. Badawy, M.E.I., et al., *Synthesis and Fungicidal Activity of New N,O-Acyl Chitosan Derivatives.* Biomacromolecules, 2004. **5**(2): p. 589-595.

34. Lee, M.-Y., et al., *Synthesis of chitosan-based polymeric surfactants and their adsorption properties for heavy metals and fatty acids.* International Journal of Biological Macromolecules, 2005. **36**(3): p. 152-158.

35.   Fujita, S. and N. Sakairi, *Water soluble EDTA-linked chitosan as a zwitterionic flocculant for pH sensitive removal of Cu(ii) ion.* RSC Advances, 2016. **6**(13): p. 10385-10392.

36.   Le Tien, C., et al., *N-acylated chitosan: hydrophobic matrices for controlled drug release.* Journal of Controlled Release, 2003. **93**(1): p. 1-13.

37.   Jiang, G.-B., et al., *Preparation of polymeric micelles based on chitosan bearing a small amount of highly hydrophobic groups.* Carbohydrate Polymers, 2006. **66**(4): p. 514-520.

38.   Lee, K.Y., et al., *Structural Determination and Interior Polarity of Self-Aggregates Prepared from Deoxycholic Acid-Modified Chitosan in Water.* Macromolecules, 1998. **31**(2): p. 378-383.

39.   Bhattarai, S.R., et al., *N-Acylated chitosan stabilized iron oxide nanoparticles as a novel nano-matrix and ceramic modification.* Carbohydrate Polymers, 2007. **69**(3): p. 467-477.

40.   Choi, C.Y., et al., *Effect of N-acylation on structure and properties of chitosan fibers.* Carbohydrate Polymers, 2007. **68**(1): p. 122-127.

41.   Hirano, S., et al., *The N-acylation of chitosan fibre and the N-deacetylation of chitin fibre and chitin–cellulose blended fibre at a solid state.* Carbohydrate Polymers, 2000. **41**(2): p. 175-179.

42.   Hu, Y., et al., *Self-aggregation and antibacterial activity of N-acylated chitosan.* Polymer, 2007. **48**(11): p. 3098-3106.

43.   Shelma, R. and C.P. Sharma, *Acyl modified chitosan derivatives for oral delivery of insulin and curcumin.* Journal of Materials Science: Materials in Medicine, 2010. **21**(7): p. 2133-2140.

44.   Mekhail, G.M., et al., *Anticancer effect of atorvastatin nanostructured polymeric micelles based on stearyl-grafted chitosan.* International Journal of Biological Macromolecules, 2012. **51**(4): p. 351-363.

45.   Vu, K.D., et al., *Development of edible bioactive coating based on modified chitosan for increasing the shelf life of strawberries.* Food Research International, 2011. **44**(1): p. 198-203.

46.   Nebbia, G. and G.N. Menozzi, *Early experiments on water desalination by freezing.* Desalination, 1968. **5**(1): p. 49-54.

47.   Lorain, O., et al., *Potential of freezing in wastewater treatment: soluble pollutant applications.* Water Research, 2001. **35**(2): p. 541-547.

48.   Pincock, R.E. and T.E. Kiovsky, *Reactions in Frozen Solutions. VI.1 The Reaction of Ethylene Chlorohydrin with Hydroxyl Ion in Ice.* Journal of the American Chemical Society, 1966. **88**(19): p. 4455-4459.

49.   O'Sullivan, D. and J.R. Sodeau, *Freeze-Induced Reactions: Formation of Iodine−Bromine Interhalogen Species from Aqueous Halide Ion Solutions.* The Journal of Physical Chemistry A, 2010. **114**(46): p. 12208-12215.

50.   Kurková, R., et al., *Chemistry of Small Organic Molecules on Snow Grains: The Applicability of Artificial Snow for Environmental Studies.* Environmental Science & Technology, 2011. **45**(8): p. 3430-3436.

51.   Vajda, T., *Cryo-bioorganic chemistry: molecular interactions at low temperature.* Cellular and Molecular Life Sciences CMLS, 1999. **56**(5): p. 398-414.

52.   Nikonorov, V.V., et al., *Synthesis and characteristics of cryogels of chitosan crosslinked by glutaric aldehyde.* Polymer Science Series A, 2010. **52**(8): p. 828-834.

53. Sashiwa, H., et al., *Chemical Modification of Chitosan, 17.* Macromolecular Bioscience, 2003. **3**(5): p. 231-233.

54. Curti, E., D. de Britto, and S.P. Campana-Filho, *Methylation of Chitosan with Iodomethane: Effect of Reaction Conditions on Chemoselectivity and Degree of Substitution.* Macromolecular Bioscience, 2003. **3**(10): p. 571-576.

55. Chen, K.C., J.S. Knapp, and K.K. Holmes, *Rapid, inexpensive method for specific detection of microbial beta-lactamases by detection of fluorescent end products.* J Clin Microbiol, 1984. **19**(6): p. 818-25.

56. Gassmann, M., et al., *Quantifying Western blots: pitfalls of densitometry.* Electrophoresis, 2009. **30**(11): p. 1845-55.

57. Abràmoff, M.D., P.J. Magalhães, and S.J. Ram, *Image processing with ImageJ.* Biophotonics international, 2004. **11**(7): p. 36-42.

58. Britto, D.d., S.P. Campana-Filho, and O.B.G.d. Assis, *Mechanical properties of N,N,N-trimethylchitosan chloride films.* Polímeros, 2005. **15**: p. 142-145.

59. Idros, N., et al., *Colorimetric-Based Detection of TNT Explosives Using Functionalized Silica Nanoparticles.* Sensors, 2015. **15**(6): p. 12891.

60. Barshick, S., *Analysis of Accelerants and Fire Debris Using Aroma Detection Technology.* 1998.

61. Hakansson, K., et al., *Low-mass ions observed in plasma desorption mass spectrometry of high explosives.* J Mass Spectrom, 2000. **35**(3): p. 337-46.

62. Anferov, V.P.M., G. V.; Fisher, R., *Pulsed spectrometer for nuclear quadrupole resonance for remote detection of nitrogen in explosives.* Review of Scientific Instruments, 2000. **71**(4): p. 1656-1659.

63. Crespy, C., et al., *Energy dispersive X-ray diffraction to identify explosive substances: Spectra analysis procedure optimization.* Nuclear Instruments and Methods in Physics Research Section A: Accelerators, Spectrometers, Detectors and Associated Equipment, 2010. **623**(3): p. 1050-1060.

64. Krausa, M. and K. Schorb, *Trace detection of 2,4,6-trinitrotoluene in the gaseous phase by cyclic voltammetry1.* Journal of Electroanalytical Chemistry, 1999. **461**(1–2): p. 10-13.

65. Eiceman, G.A. and J.A. Stone, *Peer Reviewed: Ion Mobility Spectrometers in National Defense.* Analytical Chemistry, 2004. **76**(21): p. 390 A-397 A.

66. Lu, J. and Z. Zhang, *A reusable optical sensing layer for picric acid based on the luminescence quenching of the Eu—thenoyltrifluoroacetone complex.* Analytica Chimica Acta, 1996. **318**(2): p. 175-179.

67. Rose, A., et al., *Sensitivity gains in chemosensing by lasing action in organic polymers.* Nature, 2005. **434**(7035): p. 876-879.

68. Agency, U.S.E.P., *Approaches for the remediation of federal facility sites contaminated with explosive or radioactive wastes.* 1993, Washington, D.C.: Office of Research and Development, [68]

69. Stanley, J.K., et al., *Toxicity of the conventional energetics TNT and RDX relative to new insensitive munitions constituents DNAN and NTO in Rana pipiens tadpoles.* Environmental Toxicology and Chemistry, 2015. **34**(4): p. 873-879.

70. Alnaizy, R. and A. Akgerman, *Oxidative treatment of high explosives contaminated wastewater.* Water Research, 1999. **33**(9): p. 2021-2030.

71. Senesac, L. and T.G. Thundat, *Nanosensors for trace explosive detection.* Materials Today, 2008. **11**(3): p. 28-36.

72. Shi, G.H., et al., *Fluorescence quenching of CdSe quantum dots by nitroaromatic explosives and their relative compounds.* Spectrochimica Acta Part A: Molecular and Biomolecular Spectroscopy, 2008. **70**(2): p. 247-252.

73. Engel, Y., et al., *Supersensitive Detection of Explosives by Silicon Nanowire Arrays.* Angewandte Chemie International Edition, 2010. **49**(38): p. 6830-6835.

74. Zhang, Y., et al., *Oligomer-Coated Carbon Nanotube Chemiresistive Sensors for Selective Detection of Nitroaromatic Explosives.* ACS Applied Materials & Interfaces, 2015. **7**(14): p. 7471-7475.

75. Tang, L., et al., *Uniform and rich-wrinkled electrophoretic deposited graphene film: a robust electrochemical platform for TNT sensing.* Chemical Communications, 2010. **46**(32): p. 5882-5884.

76. Balandin, A.A., et al., *Superior Thermal Conductivity of Single-Layer Graphene.* Nano Letters, 2008. **8**(3): p. 902-907.

77. Pumera, M., *Graphene-based nanomaterials and their electrochemistry.* Chemical Society Reviews, 2010. **39**(11): p. 4146-4157.

78. Brownson, D.A. and C.E. Banks, *Graphene electrochemistry: an overview of potential applications.* Analyst, 2010. **135**(11): p. 2768-2778.

79. Zhou, S.Y., et al., *Substrate-induced bandgap opening in epitaxial graphene.* Nat Mater, 2007. **6**(10): p. 770-5.

80. Schedin, F., et al., *Detection of individual gas molecules adsorbed on graphene.* Nat Mater, 2007. **6**(9): p. 652-655.

81. Pumera, M., *Graphene-based nanomaterials for energy storage.* Energy & Environmental Science, 2011. **4**(3): p. 668-674.

82. Pumera, M., *Electrochemistry of graphene: new horizons for sensing and energy storage.* The Chemical Record, 2009. **9**(4): p. 211-223.

83. Holthoff, E.L., D.N. Stratis-Cullum, and M.E. Hankus, *A Nanosensor for TNT Detection Based on Molecularly Imprinted Polymers and Surface Enhanced Raman Scattering.* Sensors, 2011. **11**(3): p. 2700.

84. Saglam, S., et al., *Electrochemical sensor for nitroaromatic type energetic materials using gold nanoparticles/poly(o-phenylenediamine-aniline) film modified glassy carbon electrode.* Talanta, 2015. **139**: p. 181-8.

85. Collins, B.E., A.T. Wright, and E.V. Anslyn, *Combining Molecular Recognition, Optical Detection, and Chemometric Analysis*, in *Creative Chemical Sensor Systems*, T. Schrader, Editor. 2007, Springer Berlin Heidelberg: Berlin, Heidelberg. p. 181-218.

86. Wulff, G., T. Gross, and R. Schönfeld, *Enzyme Models Based on Molecularly Imprinted Polymers with Strong Esterase Activity.* Angewandte Chemie International Edition in English, 1997. **36**(18): p. 1962-1964.

87. Lu, Y., et al., *Molecular recognition through the exact placement of functional groups on non-covalent molecularly imprinted polymers.* Journal of Chromatography A, 2002. **950**(1): p. 89-97.

88. Dhal, P.K. and F.H. Arnold, *Template-mediated synthesis of metal-complexing polymers for molecular recognition.* Journal of the American Chemical Society, 1991. **113**(19): p. 7417-7418.

89.   Svenson, J. and I.A. Nicholls, *On the thermal and chemical stability of molecularly imprinted polymers.* Analytica Chimica Acta, 2001. **435**(1): p. 19-24.

90.   Xu, L., et al., *Chitosan in Molecularly-Imprinted Polymers: Current and Future Prospects.* International Journal of Molecular Sciences, 2015. **16**(8): p. 18328.

91.   Chiou, M.-S., P.-Y. Ho, and H.-Y. Li, *Adsorption of anionic dyes in acid solutions using chemically cross-linked chitosan beads.* Dyes and Pigments, 2004. **60**(1): p. 69-84.

92.   Wang, L., et al., *A novel nitromethane biosensor based on biocompatible conductive redox graphene-chitosan/hemoglobin/graphene/room temperature ionic liquid matrix.* Biosensors and Bioelectronics, 2010. **26**(3): p. 991-995.

93.   Diaz Aguilar, A., et al., *A hybrid nanosensor for TNT vapor detection.* Nano Lett, 2010. **10**(2): p. 380-4.

94.   Liu, M. and W. Chen, *Graphene nanosheets-supported Ag nanoparticles for ultrasensitive detection of TNT by surface-enhanced Raman spectroscopy.* Biosens Bioelectron, 2013. **46**: p. 68-73.

95.   Ko, H. and V.V. Tsukruk, *Nanoparticle-decorated nanocanals for surface-enhanced Raman scattering.* Small, 2008. **4**(11): p. 1980-4.

96.   Zhang, Z., et al., *Antibacterial Properties of Cotton Fabrics Treated with Chitosan.* Textile Research Journal, 2003. **73**(12): p. 1103-1106.

97.   Liao, C.-D., et al., *Chemical Vapor Deposition Synthesis and Raman Spectroscopic Characterization of Large-Area Graphene Sheets.* The Journal of Physical Chemistry A, 2013. **117**(39): p. 9454-9461.

98.   Martins, A.M., et al., *Electrically Conductive Chitosan/Carbon Scaffolds for Cardiac Tissue Engineering.* Biomacromolecules, 2014. **15**(2): p. 635-643.

99.   Marinho, B., et al., *Electrical conductivity of compacts of graphene, multi-wall carbon nanotubes, carbon black, and graphite powder.* Powder Technology, 2012. **221**: p. 351-358.

100.   Garzon, F., E. Brosha, and R. Mukundan, *Explosives detection sensor*. 2006, Google Patents.

101.   McGill, R.A., et al., *The design of functionalized silicone polymers for chemical sensor detection of nitroaromatic compounds.* Sensors and Actuators B: Chemical, 2000. **65**(1–3): p. 5-9.

102.   Kannan, G., et al., *Adsorption studies of carbowax coated surface acoustic wave (SAW) sensor for 2, 4-dinitro toluene (DNT) vapour detection.* Sensors and Actuators B: Chemical, 2004. **101**(3): p. 328-334.

103.   Yang, X., et al., *Molecular recognition and self-assembled polymer films for vapor phase detection of explosives.* Talanta, 2001. **54**(3): p. 439-445.

104.   Dorozhkin, L.M., et al., *Detection of trace amounts of explosives and/or explosive related compounds on various surfaces by a new sensing technique/material.* Sensors and Actuators B: Chemical, 2004. **99**(2–3): p. 568-570.

105.   Liu, Y., et al., *Fluorescent Polyacetylene Thin Film Sensor for Nitroaromatics.* Langmuir, 2001. **17**(24): p. 7452-7455.

106.   Zhang, H.-X., et al., *Electrochemical Sensor for Detecting Ultratrace Nitroaromatic Compounds Using Mesoporous SiO2-Modified Electrode.* Analytical Chemistry, 2006. **78**(6): p. 1967-1971.

107. Ma, Y., et al., *Highly Selective and Sensitive Fluorescent Paper Sensor for Nitroaromatic Explosive Detection.* Analytical Chemistry, 2012. **84**(19): p. 8415-8421.

108. Ahmad, K., et al., *Preparation of SrTiO3 perovskite decorated rGO and electrochemical detection of nitroaromatics.* Electrochimica Acta, 2016. **215**: p. 435-446.

109. Zarei, A.R. and B. Ghazanchayi, *Design and fabrication of optical chemical sensor for detection of nitroaromatic explosives based on fluorescence quenching of phenol red immobilized poly(vinyl alcohol) membrane.* Talanta, 2016. **150**: p. 162-168.

110. Chen, T.-W., et al., *Determination of Explosives Using Electrochemically Reduced Graphene.* Chemistry – An Asian Journal, 2011. **6**(5): p. 1210-1216.

111. Yu, R., et al., *A novel double-layer electrospun nanofibrous membrane sensor for detecting nitroaromatic compounds.* Journal of Materials Science, 2016. **51**(23): p. 10350-10360.

112. Nuyken, O., *Block Copolymers — Overview and Critical Survey. Von A. Noshay und J. E. McGrath. Academic Press. Inc., New York 1977. 1. Aufl., XVI, 516 S., geb. $ 45.00.* Angewandte Chemie, 1978. **90**(1): p. 77-77.

113. Szycher, M., *Szycher's handbook of polyurethanes.* 1999: CRC press.

114. Prisacariu, C., *Polyurethane elastomers: from morphology to mechanical aspects.* 2011: Springer Science & Business Media.

115. Yilgör, I., E. Yilgör, and G.L. Wilkes, *Critical parameters in designing segmented polyurethanes and their effect on morphology and properties: A comprehensive review.* Polymer, 2015. **58**: p. A1-A36.

116. Yilgor, I. and E. Yilgor, *Structure-Morphology-Property Behavior of Segmented Thermoplastic Polyurethanes and Polyureas Prepared without Chain Extenders.* Polymer Reviews, 2007. **47**(4): p. 487-510.

117. Delebecq, E., et al., *On the versatility of urethane/urea bonds: reversibility, blocked isocyanate, and non-isocyanate polyurethane.* Chemical reviews, 2012. **113**(1): p. 80-118.

118. Krol, P., *Synthesis methods, chemical structures and phase structures of linear polyurethanes. Properties and applications of linear polyurethanes in polyurethane elastomers, copolymers and ionomers.* Progress in materials science, 2007. **52**(6): p. 915-1015.

119. Yilgor, I., et al., *Influence of soft segment molecular weight on the mechanical hysteresis and set behavior of silicone-urea copolymers with low hard segment contents.* Polymer, 2011. **52**(2): p. 266-274.

120. Unal, S., et al., *A new generation of highly branched polymers: hyperbranched, segmented poly (urethane urea) elastomers.* Macromolecules, 2004. **37**(19): p. 7081-7084.

121. Yilgor, E., M. Isik, and I. Yilgor, *Novel Synthetic Approach for the Preparation of Poly(urethaneurea) Elastomers.* Macromolecules, 2010. **43**(20): p. 8588-8593.

122. Jewrajka, S.K., et al., *Polyisobutylene-based polyurethanes. II. Polyureas containing mixed PIB/PTMO soft segments.* Journal of Polymer Science Part A: Polymer Chemistry, 2009. **47**(11): p. 2787-2797.

123. Erdodi, G., et al., *Polyisobutylene-based polyurethanes. III. Polyurethanes containing PIB/PTMO soft co-segments.* Journal of Polymer Science Part A: Polymer Chemistry, 2009. **47**(20): p. 5278-5290.

124.   Fernández, C.E., et al., *An overview on 12-polyurethane: Synthesis, structure and crystallization.* European Polymer Journal, 2010. **46**(11): p. 2089-2098.

125.   Kang, J., et al., *PIB-based polyurethanes. IV. The morphology of polyurethanes containing soft co-segments*.* Journal of Polymer Science Part A: Polymer Chemistry, 2009. **47**(22): p. 6180-6190.

126.   Piril Ertem, S., et al., *Effect of soft segment molecular weight on tensile properties of poly(propylene oxide) based polyurethaneureas.* Polymer, 2012. **53**(21): p. 4614-4622.

127.   Yilgor, I., et al., *Contribution of soft segment entanglement on the tensile properties of silicone–urea copolymers with low hard segment contents.* Polymer, 2009. **50**(19): p. 4432-4437.

128.   Korley, L.T.J., et al., *Effect of the degree of soft and hard segment ordering on the morphology and mechanical behavior of semicrystalline segmented polyurethanes.* Polymer, 2006. **47**(9): p. 3073-3082.

129.   Klinedinst, D.B., et al., *The effect of varying soft and hard segment length on the structure–property relationships of segmented polyurethanes based on a linear symmetric diisocyanate, 1,4-butanediol and PTMO soft segments.* Polymer, 2012. **53**(23): p. 5358-5366.

130.   Das, S., et al., *Effect of Symmetry and H-bond Strength of Hard Segments on the Structure-Property Relationships of Segmented, Nonchain Extended Polyurethanes and Polyureas.* Journal of Macromolecular Science, Part B, 2007. **46**(5): p. 853-875.

131.   Das, S., et al., *Structure–property relationships and melt rheology of segmented, non-chain extended polyureas: Effect of soft segment molecular weight.* Polymer, 2007. **48**(1): p. 290-301.

132.   Yilgor, I., et al., *Time-dependent morphology development in segmented polyetherurea copolymers based on aromatic diisocyanates.* Journal of Polymer Science Part B: Polymer Physics, 2009. **47**(5): p. 471-483.

133.   Hood, M.A., et al., *Morphology control of segmented polyurethanes by crystallization of hard and soft segments.* Polymer, 2010. **51**(10): p. 2191-2198.

134.   Sami, S., et al., *Understanding the influence of hydrogen bonding and diisocyanate symmetry on the morphology and properties of segmented polyurethanes and polyureas: Computational and experimental study.* Polymer, 2014. **55**(18): p. 4563-4576.

135.   Kulkarni, A.S., et al., *Micro-phase Separation via Spinodal-like Decomposition in Hexamethylynediisocyanate (HDI)-polyurea.* Journal of Inorganic and Organometallic Polymers and Materials, 2012. **22**(3): p. 624-628.

136.   Unal, S., et al., *Understanding the structure development in hyperbranched polymers prepared by oligomeric A2+B3 approach: comparison of experimental results and simulations.* Polymer, 2005. **46**(13): p. 4533-4543.

137.   Yılgör, İ., E. Yurtsever, and B. Erman, *Conformational Analysis of Model Poly(ether urethane) Chains in the Unperturbed State and under External Forces.* Macromolecules, 2002. **35**(26): p. 9825-9831.

138.   Yilgör, E., E. Yurtsever, and I. Yilgör, *Hydrogen bonding and polyurethane morphology. II. Spectroscopic, thermal and crystallization behavior of polyether blends with 1,3-dimethylurea and a model urethane compound.* Polymer, 2002. **43**(24): p. 6561-6568.

139.   Yılgör, E., İ. Yılgör, and E. Yurtsever, *Hydrogen bonding and polyurethane morphology. I. Quantum mechanical calculations of hydrogen bond energies and vibrational spectroscopy of model compounds.* Polymer, 2002. **43**(24): p. 6551-6559.

140.   Yildirim, E., et al., *Effect of intersegmental interactions on the morphology of segmented polyurethanes with mixed soft segments: A coarse-grained simulation study.* Polymer, 2016. **90**: p. 204-214.

141.   Qiu, W., et al., *Reversibility between glass and melting transitions of poly (oxyethylene).* Macromolecules, 2005. **38**(20): p. 8454-8467.

142.   Matsuura, H. and K. Fukuhara, *Vibrational spectroscopic studies of conformation of poly (oxyethylene). II. Conformation–spectrum correlations.* Journal of Polymer Science Part B: Polymer Physics, 1986. **24**(7): p. 1383-1400.

143.   Uemura, T., et al., *Unveiling thermal transitions of polymers in subnanometre pores.* Nature communications, 2010. **1**: p. 83.

144.   French, A.C., A.L. Thompson, and B.G. Davis, *High-Purity Discrete PEG-Oligomer Crystals Allow Structural Insight.* Angewandte Chemie, 2009. **121**(7): p. 1274-1278.

145.   Kim, S.A. and L.A. Archer, *Hierarchical Structure in Semicrystalline Polymers Tethered to Nanospheres.* Macromolecules, 2014. **47**(2): p. 687-694.

146.   Yoshihara, T., H. Tadokoro, and S. Murahashi, *Normal Vibrations of the Polymer Molecules of Helical Conformation. IV. Polyethylene Oxide and Polyethylene-d4 Oxide.* The Journal of Chemical Physics, 1964. **41**(9): p. 2902-2911.

147.   Chrissopoulou, K., et al., *Crystallinity and chain conformation in PEO/layered silicate nanocomposites.* Macromolecules, 2011. **44**(24): p. 9710-9722.

148.   Kwon, O.-H., V. Ortalan, and A.H. Zewail, *Macromolecular structural dynamics visualized by pulsed dose control in 4D electron microscopy.* Proceedings of the National Academy of Sciences, 2011. **108**(15): p. 6026-6031.

149.   Favino, M., R. Krause, and I. Pivkin, *A survey on stochastic multi-scale modeling in biomechanics: computational challenges.* arXiv preprint arXiv:1609.07719, 2016.

150.   Groot, R.D. and P.B. Warren, *Dissipative particle dynamics: Bridging the gap between atomistic and mesoscopic simulation.* Journal of Chemical Physics, 1997. **107**(11): p. 4423.

151.   Hoogerbrugge, P.J. and J.M.V.A. Koelman, *Simulating Microscopic Hydrodynamic Phenomena with Dissipative Particle Dynamics.* EPL (Europhysics Letters), 1992. **19**(3): p. 155.

152.   Liu, K., et al., *Molecular and mesoscale mechanism for hierarchical self-assembly of dipeptide and porphyrin light-harvesting system.* Physical Chemistry Chemical Physics, 2016. **18**(25): p. 16738-16747.

153.   Maurel, G., et al., *Multiscale Modeling of the Polymer–Silica Surface Interaction: From Atomistic to Mesoscopic Simulations.* The Journal of Physical Chemistry C, 2015. **119**(9): p. 4817-4826.

154.   Ozden-Yenigun, E., et al., *Molecular basis for solvent dependent morphologies observed on electrosprayed surfaces.* Phys Chem Chem Phys, 2013. **15**(41): p. 17862-72.

155.   Kacar, G., C. Atilgan, and A.S. Özen, *Mapping and Reverse-Mapping of the Morphologies for a Molecular Understanding of the Self-Assembly of Fluorinated Block Copolymers.* The Journal of Physical Chemistry C, 2010. **114**(1): p. 370-382.

156. Furuncuoğlu Özaltın, T., et al., *Multiscale modeling of poly(2-isopropyl-2-oxazoline) chains in aqueous solution.* European Polymer Journal.

157. Yildirim, E., et al., *Multiscale Modeling of the Morphology and Properties of Segmented Silicone-Urea Copolymers.* Journal of Inorganic and Organometallic Polymers and Materials, 2012. **22**(3): p. 604-616.

158. Chantawansri, T.L., et al., *Coarse-grained modeling of model poly(urethane urea)s: Microstructure and interface aspects.* Polymer, 2012. **53**(20): p. 4512-4524.

159. Tal-Ezer, H. and R. Kosloff, *An accurate and efficient scheme for propagating the time dependent Schrödinger equation.* The Journal of chemical physics, 1984. **81**(9): p. 3967-3971.

160. Allen, M.P. and D.J. Tildesley, *Computer simulation of liquids.* 1989: Oxford university press.

161. Andersen, H.C., *Molecular dynamics simulations at constant pressure and/or temperature.* The Journal of chemical physics, 1980. **72**(4): p. 2384-2393.

162. Born, M. and J.R. Oppenheimer, *On the quantum theory of molecules.* Сборник статей к мультимедийному электронному учебно-методическому комплексу по дисциплине «физика атома и атомных явлений»/отв. ред. Шундалов МБ; БГУ, Физический факультет, 1927.

163. Tildesley, D. and M. Allen, *Computer simulation of liquids.* Clarendon, Oxford, 1987.

164. Hünenberger, P.H., *Thermostat algorithms for molecular dynamics simulations.* Advanced computer simulation, 2005: p. 130-130.

165. Allen, M. and D. Tildesley, *Molecular Simulation of Liquids.* Clarendon, Oxford, 1987.

166. Tsai, D., *The virial theorem and stress calculation in molecular dynamics.* The Journal of Chemical Physics, 1979. **70**(3): p. 1375-1382.

167. Saito, H., et al., *Molecular collective dynamics in solid para-hydrogen and ortho-deuterium: The Parrinello–Rahman-type path integral centroid molecular dynamics approach.* The Journal of chemical physics, 2003. **119**(2): p. 953-963.

168. Koelman, J. and P. Hoogerbrugge, *Dynamic simulations of hard-sphere suspensions under steady shear.* EPL (Europhysics Letters), 1993. **21**(3): p. 363.

169. Andersson, C., *Flory-Huggins theory.* 2008.

170. Groot, R.D. and P.B. Warren, *Dissipative particle dynamics: Bridging the gap between atomistic and mesoscopic simulation.* The Journal of chemical physics, 1997. **107**(11): p. 4423-4435.

171. MaterialsStudio, *Materials Studio 6.0.* 2002, Dassault Systems: San Diego.

172. Theodorou, D.N. and U.W. Suter, *Detailed molecular structure of a vinyl polymer glass.* Macromolecules, 1985. **18**(7): p. 1467-1478.

173. Sun, H., *COMPASS: An ab Initio Force-Field Optimized for Condensed-Phase ApplicationsOverview with Details on Alkane and Benzene Compounds.* The Journal of Physical Chemistry B, 1998. **102**(38): p. 7338-7364.

174. Andersen, H.C., *Molecular dynamics simulations at constant pressure and/or temperature.* The Journal of Chemical Physics, 1980. **72**: p. 2384-2393.

175. H. J. C. Berendsen, J.P.M.P., W. F. Vangunsteren, and J.R.H. A. Dinola, *Molecular dynamics with coupling to an external bath.* The Journal of Chemical Physics, 1984. **81**: p. 3684-3690.

176.   Ozden-Yenigun, E., et al., *Molecular basis for solvent dependent morphologies observed on electrosprayed surfaces.* Physical Chemistry Chemical Physics, 2013. **15**(41): p. 17862-17872.

177.   Huggins, M.L., *The Solubility of Nonelectrolytes. By Joel H. Hildebrand and Robert S. Scott.* The Journal of Physical Chemistry, 1951. **55**(4): p. 619-620.

178.   Robert D. Groot, T.J.M., *Dynamic simulation of diblock copolymer microphase separation.* The Journal of Chemical Physics, 1998. **108**.

179.   ACD/ChemSketch, *ACD/ChemSketch 5.0.* 2003, Advanced Chemistry Development, Inc.: Toronto, ON, Canada.

180.   Rzepiela, A.J., et al., *Reconstruction of atomistic details from coarse-grained structures.* Journal of Computational Chemistry, 2010. **31**(6): p. 1333-1343.

181.   Lee, H., et al., *Molecular dynamics studies of polyethylene oxide and polyethylene glycol: hydrodynamic radius and shape anisotropy.* Biophysical journal, 2008. **95**(4): p. 1590-1599.

182.   Lee, H., et al., *A coarse-grained model for polyethylene oxide and polyethylene glycol: conformation and hydrodynamics.* The journal of physical chemistry B, 2009. **113**(40): p. 13186-13194.

183.   Mark, J.E. and P.J. Flory, *The Configuration of the Polyoxyethylene Chain.* Journal of the American Chemical Society, 1965. **87**(7): p. 1415-1423.

184.   Tarazona, M.P., et al., *Conformational characteristics of poly(vinylpyrrolidone). solvent-dependence of the chain dimensions.* Macromolecular Theory and Simulations, 1993. **2**(5): p. 697-710.

185.   Marrink, S.J., et al., *The MARTINI Force Field: Coarse Grained Model for Biomolecular Simulations.* The Journal of Physical Chemistry B, 2007. **111**(27): p. 7812-7824.

186.   Wool, R.P., *Polymer Interfaces, Structure and Strength.* 1993, New York: Hanser Publishers.

APPENDIX A

This appendix describes TLM calculations and the derivation of sheet resistance from TLM measurements. To determine the sheet resistance of the sensor, we use two-probe (1 for current, 1 for voltage) electrical measurements. The two contacts are located at the end of electrodes with a contact area of A_c.

Equation A 1
$$R_T = 2R_m + 2R_c + R_s$$

where R_m is the resistance arising from metallic contact lines, R_c is the resistance due to metal and graphene interface, and R_s is the sheet resistance of the semiconductor. Since $R_c \gg R_m$ in most cases, R_m is usually ignored. Therefore, two terms are regarded to calculate the total resistance

Equation A 2
$$R_T = \frac{R_s}{W_{ch}}d + 2R_c$$

This relation provides calculation of sheet resistance from TLM measurement of a set of identical resistor pairs in varying distance.
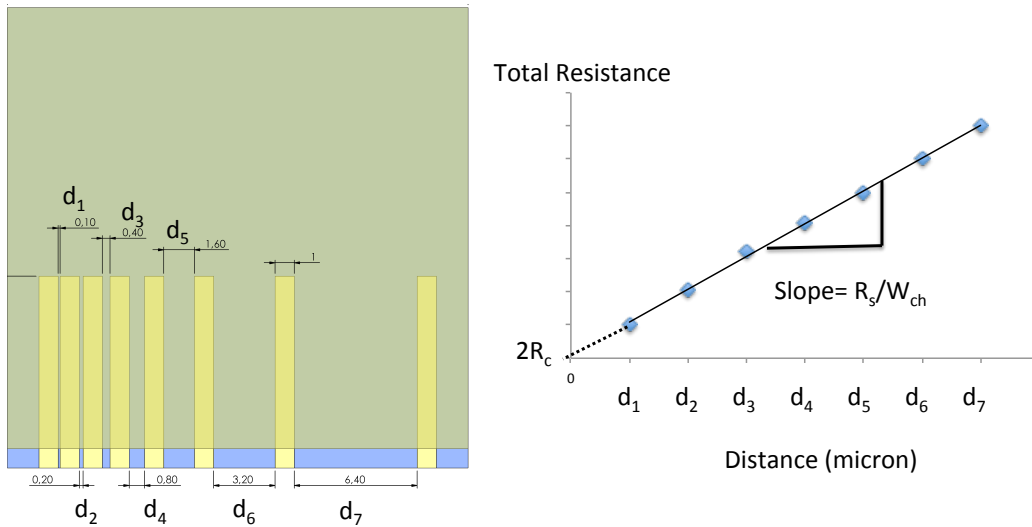

Figure A 1 Sheet resistance calculation from TLM patterns. Distance values are given in mm.

In our study, sheet resistances of graphene sheets in the presence of varying amounts of NTO were calculated by TLM measurements of gold contacts. Once we construct the distance vs. total resistance curves from I-V measurements, we derived the sheet resistance as follows:
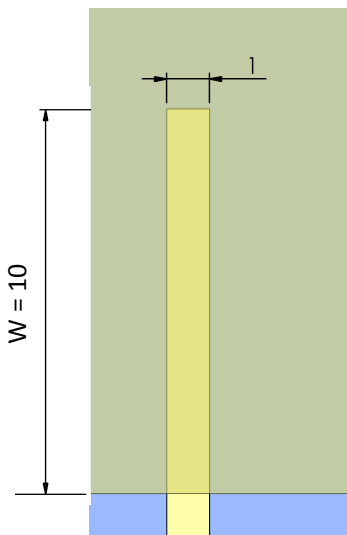

Figure A 2 Dimensions of metallic contact lines. Length valeus are given in mm.

Equation A 3

$$R_s = slope\ x\ W$$

All the sheet resistance values described in Chapter 2 were calculated using this procedure. Moreover, resistance values were derived from 5 different calculations in each data point. Figure A-3 demonstrates an example calculation of sheet resistance employed in this study.

| CSNTO washed	
Distance (micron)	Resistance (Ohm)
100	15,86
200	28,73
400	44,79
800	92,26
1600	178,7
3200	354,1
6400	524,1
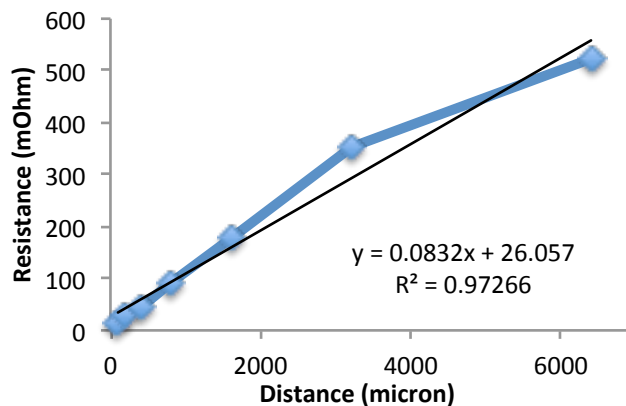
Figure A 3 TLM Calculations for CSNTO sensor in the absence of NTO (pure water).

Putting the slope of distance vs. resistance curve in Figure A-3 (bottom) into Equation A-3, the sheet resistance of graphene in the absence of NTO is;

$$R_S = 0.0832 \; \frac{Ohm}{\mu m} \; x \; 10000 \mu m$$

$$R_S = 832 \; ohm/sq$$

Sheet resistances of graphenes in the presence of varying NTO concentration were also calculated using the same strategy.

CSNTO in 0,01 mg/mL NTO	
Distance (micron)	Resistance (leveled)
100	19,36
200	35,93
400	53,3
800	96,62
1600	166,5
3200	300,3
6400	540,7

R_s = 822 ohm/sq

y = 0.0822x + 24.085
R^2 = 0.99706
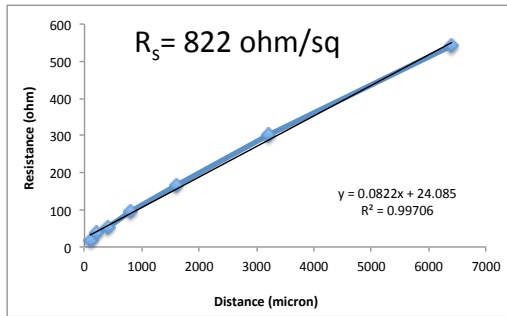
CSNTO in 0,04 mg/mL NTO	
Distance (micron)	Resistance (leveled)
100	18,27
200	35,43
400	59,47
800	120,2
1600	206,0
3200	304,8
6400	507,8

R_s = 764 ohm/sq

y = 0.0764x + 40.233
R^2 = 0.97606
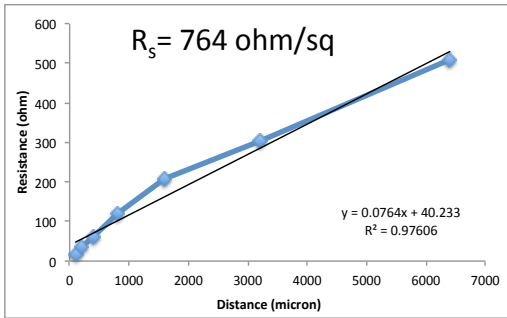
CSNTO in 0,08 mg/mL NTO	
Distance (micron)	Resistance (Ohm)
100	20,67
200	52,72
400	79,37
800	134,6
1600	190,5
3200	284,2
6400	456

R_s = 657 ohm/sq

y = 0.0657x + 54.769
R^2 = 0.96938
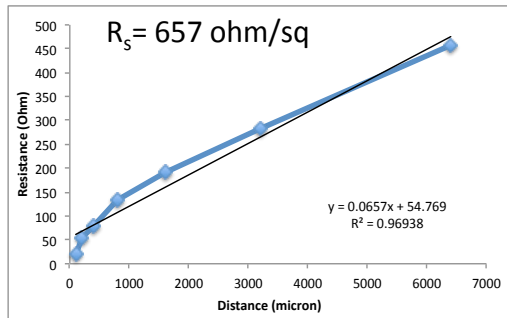
CSNTO in 0,1 mg/mL NTO	
Distance (micron)	Resistance (Ohm)
100	17,36
200	29,76
400	52,34
800	93,01
1600	159,4
3200	242,2
6400	383,3

R_s = 574 ohm/sq

y = 0.0574x + 35.429
R^2 = 0.97219
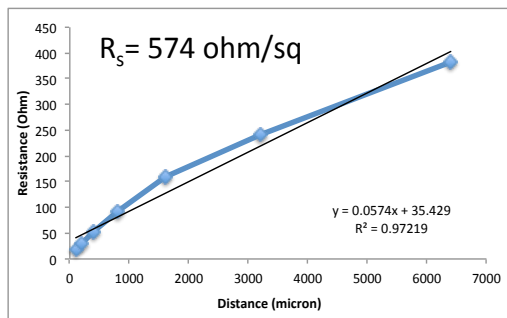
Figure A 4 TLM results of CSNTO sensor within the linear region.

Sheet resistance values of CSNTO were linear up to an NTO concentration of 0.1 mg/mL. After this NTO concentration, TLM results started to deviate from linearity.

CSNTO in 0,4 mg/mL NTO	
Distance (micron)	Resistance (Ohm)
100	21,88
200	50,12
400	88,3
800	177,2
1600	352,3
3200	396,5
6400	513,4

R_s= 762 ohm/sq

$y = 0.0762x + 90.298$
$R^2 = 0.82727$

CSNTO in 0,8 mg/mL NTO	
Distance (micron)	Resistance (Ohm)
100	24,77
200	42,68
400	80
800	164,7
1600	-
3200	-
6400	542,1

R_s= 782 ohm/sq

$y = 0.0782x + 47.238$
$R^2 = 0.97622$

CSNTO in 1.0 mg/mL NTO	
Distance (micron)	Resistance (Ohm)
100	298,7
200	-
400	333,6
800	318,3
1600	-
3200	495,7
6400	788

R_s= 771 ohm/sq

$y = 0.0771x + 278.88$
$R^2 = 0.98617$

Figure A 5 TLM results of CSNTO sensor within the linear region.

The deviation from linearity is demonstrated in Figure A-6.
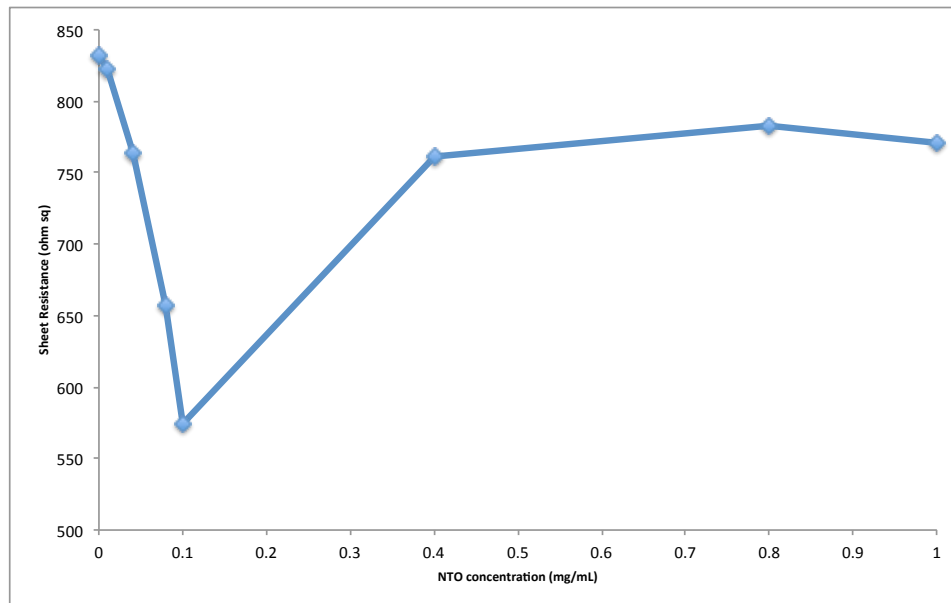
Figure A 6 Sheet resistances with respect to NTO concentration.

Considering the deviation from straight line, the linear region of the sonser was determined as 0.01-0.1 mg/mL.

APPENDIX B

This appendix describes details of all the calculations performed in Chapter 3. Firstly, Canonical ensemble parameters used for energy refinement are demonstrated in Figure B-1.
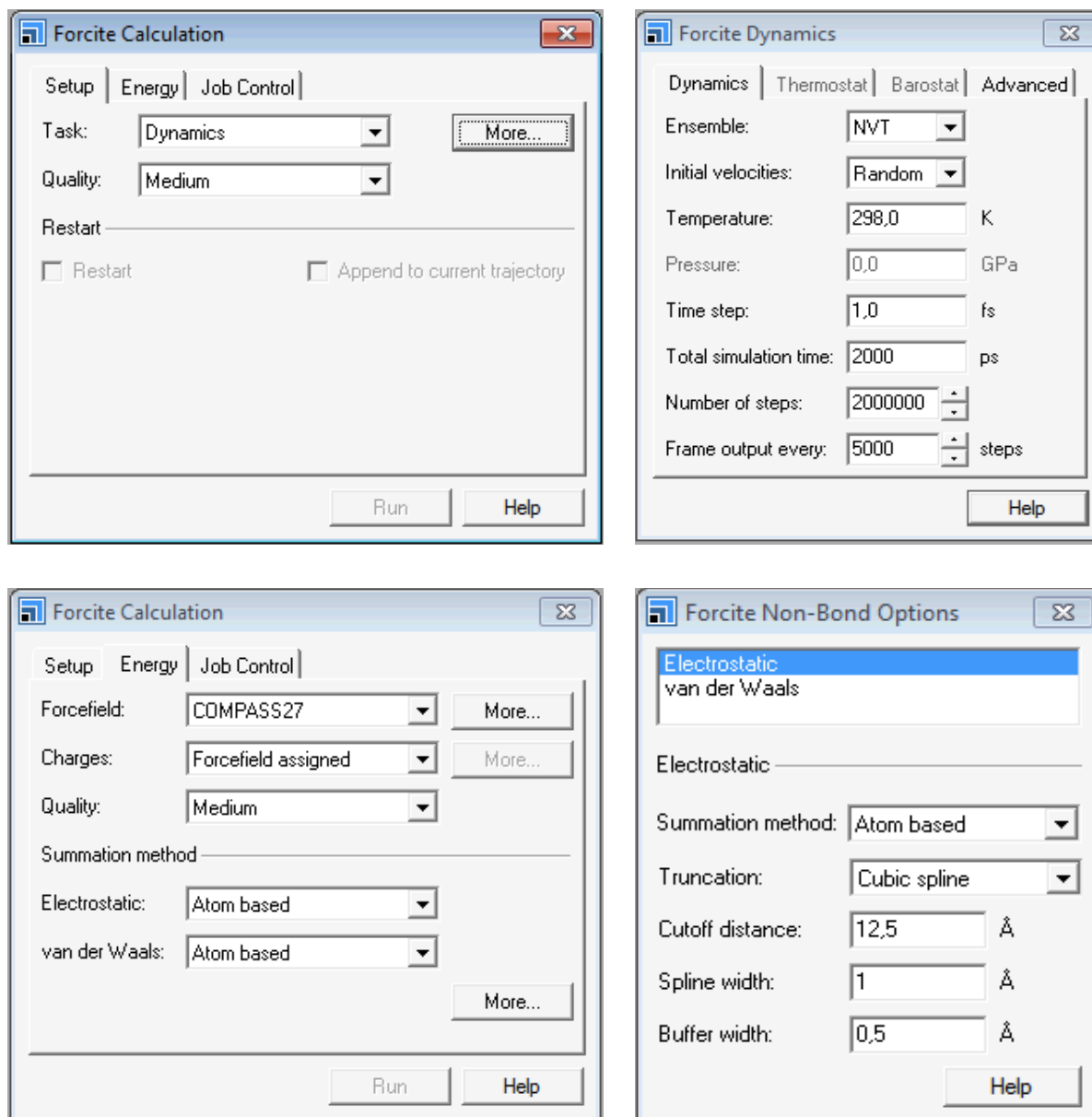
Figure B 1 Setup and energy parameters for canonical ensembles.

Isothermal-isobaric ensemble (NPT) MD simulations were carried out with the following parameters demonstrated in Figure B-2.
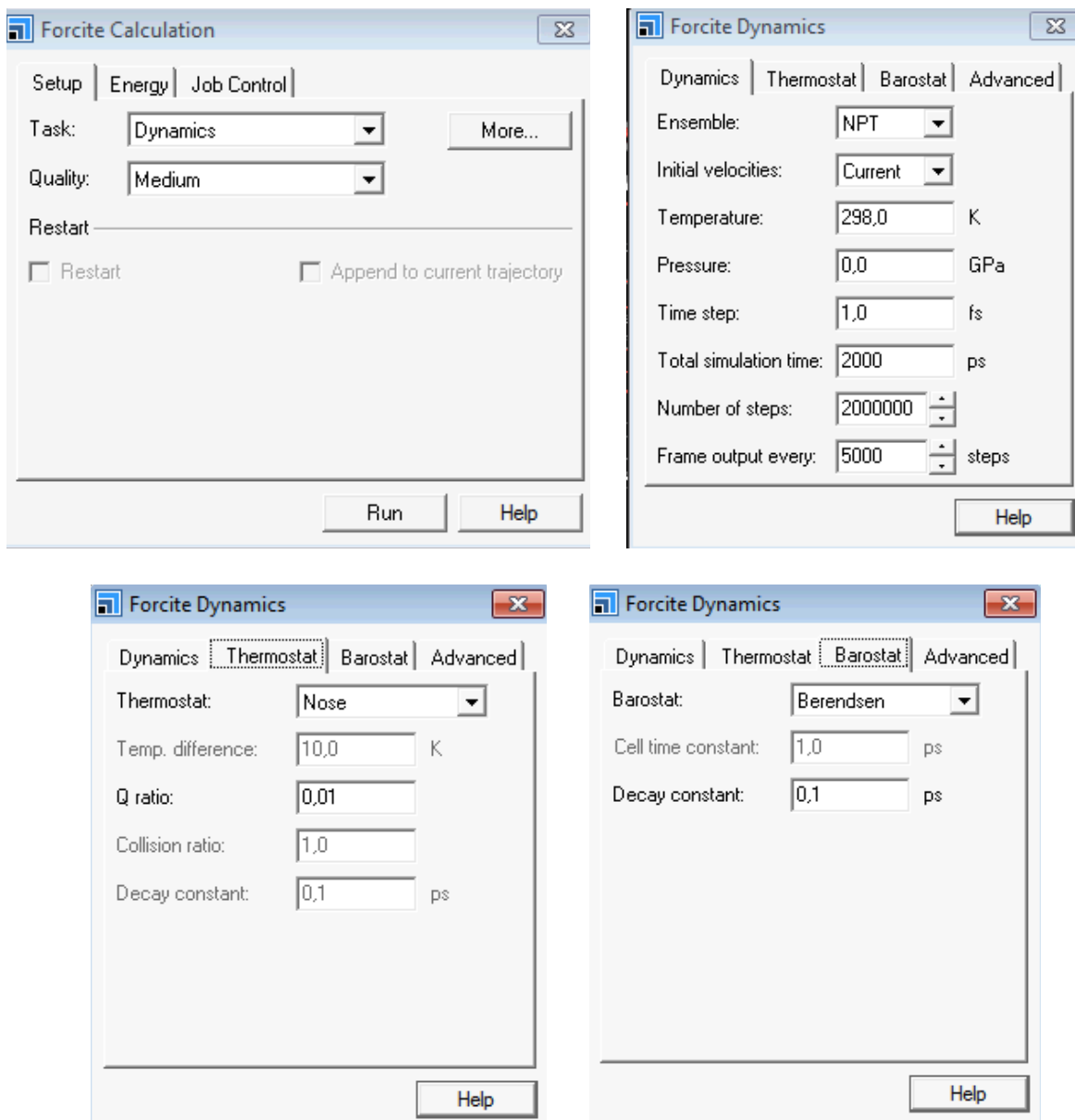
Figure B 2 Setup, thermostat and barostat parameters used in NPT ensemble.

For DPD studies, 20000 steps DPD equilibration were followed by 100000 steps of production DPDs. Details of the parameters used in all DPD calculation are provided in Figure B-3. Note that the interaction parameters are case-dependent, and given here as an example.
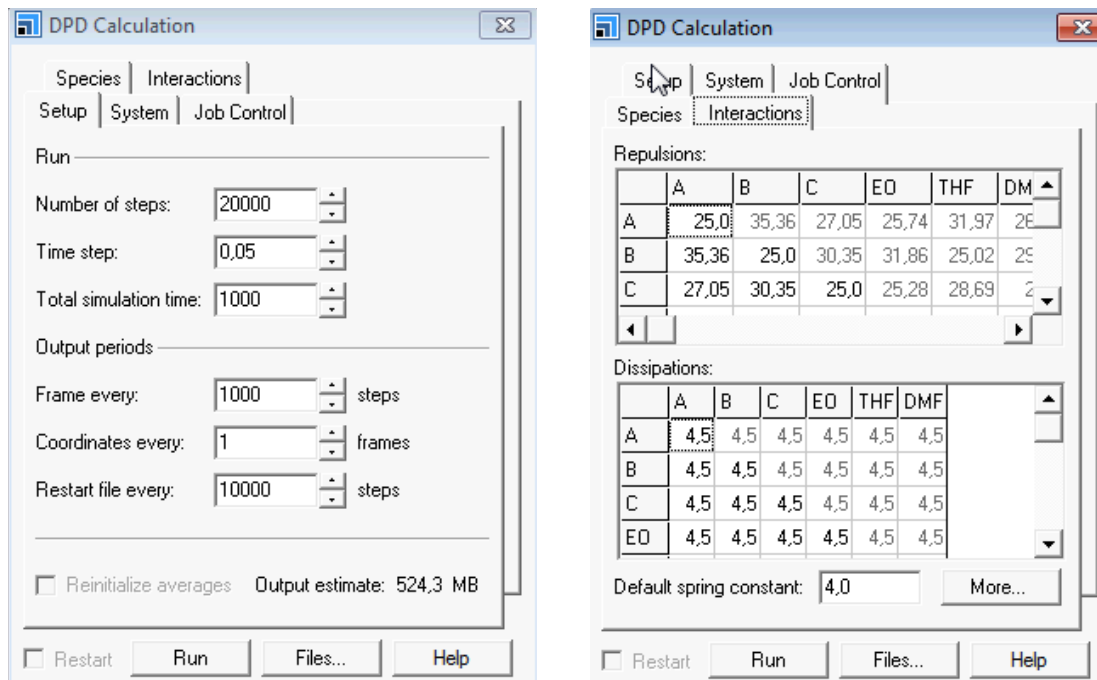

Figure B 3 Setup, interaction, dissipation and spring constant parameters parameters used in DPD calculations.

Appendix B.1 Fine Graining Script

To fine grain beads to atomistic details, a script prepared by *Marrink et al.*[180] was employed This script identifies and matches the beads with atomic information provided in the template molecule, and places each centroid to the corresponding bead's coordinate. Note that the editable settings section in the script should be adjusted for each trajectory. Details of this script are as follows:

```perl
#!perl

use strict;
use MaterialsScript qw(:all);

# Title: Creates initial atomistic model by reverse mapping from beads
# Author: Reinier Akkermans
# Version: 1.0
# MS Version: 5.5
# Modules: Materials Visualizer

# Fine-grains bead to atomistic representation. As input, requires a bead
document, and study table.
# The study table contains the marked up atomistic structures and the name
in the study table should
# map to the bead name.

# To make this work, there also needs to be a map between the bead name
and the centroid and motion-group
# name on the atomistic representation. This should be setup before the
initial mesoscale calculations
# are run otherwise it is very hard to do this post simulation.

# For each type of meso-molecule in the system, each bead in the molecule
must have a unique name that you
# can identify it with. Note that the ForcefieldType and Name can be
different so you don't have to set up
# duplicate forcefield types.

######################################################################
# Begin editable settings

my $forceConstant = 100; #  Defined on the restraint kcal/mol/A^2

my $doc = $Documents{"fullpolyTHF.xsd"}; # the bead document

my $std = $Documents{"patternTHF.std"}; # the study table with the marked
up pattern documents

# End editable settings
```

```
##############################################################################


# Create a hash table for quick access and a name list to enable set
creation
my %patterns;
my @names;
for(my $row = 0; $row < $std->RowCount; $row++)
{
      my $patternDoc = $std->Cell($row,0);
      if(defined $patternDoc)
      {
            my $name = $std->Cell($row,1);
            $patterns{$name} = $patternDoc;
            foreach my $motionGroup (@{$patternDoc->MotionGroups})
            {
                  push(@names,$motionGroup->Name);
            }

      }
}

# create the fine-grained document
my $docFine = Documents->New($doc->Name."_fine.xsd");

# loop over all molecules in the coarse-grained document
my $moleculesCoarse = $doc->UnitCell->Molecules;
foreach my $moleculeCoarse (@{$moleculesCoarse})
{
      my $name = $moleculeCoarse->Name;

      # find the corresponding template document (stop if not found)
      my $patternDoc = $patterns{$name};
      if(!defined $patternDoc){ die "Template document $name not found\n";}

      # copy the molecule into the new document
      my $moleculeFine = $docFine->CopyFrom($patternDoc);

      # move the motion groups into position
      foreach my $bead (@{$moleculeCoarse->Beads})
      {
            # the name of the bead
            my $beadName = $bead->Name;

            # the position of the bead
            my $beadXYZ = $bead->XYZ;

            # find the corresponding motion group (stop if not found)
            my $motionGroup = $moleculeFine->MotionGroups($beadName);
            if(!defined $motionGroup){ die "Motion group $beadName not
found\n";}
```

```perl
            # move the motion group (note: this does not work for
centroids)
            $motionGroup->RotationCenter = $beadXYZ;
        }

        # create anchors, distances and restraints
        foreach my $motionGroup (@{$moleculeFine->MotionGroups})
        {
            # the name of the bead
            my $motionGroupName = $motionGroup->Name;

            # find the centroid with the same name (stop if not found)
            my $centroid = $moleculeFine->Centroids($motionGroupName);
            if(!defined $centroid){ die "Centroid $motionGroupName not
found\n";;}

            # create an anchor at the centroid position
            my $anchor = $docFine->CreatePositionAnchor($centroid-
>CentroidXYZ);
            $anchor->Name = $motionGroupName;

            # create a distance monitor between the anchor and the centroid
            my $distance = $docFine->CreateDistance([$anchor,$centroid]);
            $distance->Name = $motionGroupName;

            # apply a restraint to the distance
            my $restraint = $distance->CreateRestraint("Harmonic",
                    [HarmonicMinimum => 0, HarmonicForceConstant =>
$forceConstant]);
            $restraint->Name = $motionGroupName;
        }
}

# create sets for easy selection on the UI later
foreach my $name (@names)
{
      my $filteredAnchors = FilterByName($docFine->PositionAnchors, $name);
      $docFine->CreateSet("Anchors_". $name, $filteredAnchors);

      my $filteredDistances = FilterByName($docFine->Distances, $name);
      $docFine->CreateSet("Distances_". $name, $filteredDistances);

      my $filteredRestraints = FilterByName($docFine->Restraints, $name);
      $docFine->CreateSet("Restraints_". $name, $filteredRestraints);

      my $filteredCentroids = FilterByName($docFine->Centroids, $name);
      $docFine->CreateSet("Centroids_". $name, $filteredCentroids);

      my $filteredMotionsGroups = FilterByName($docFine->MotionGroups,
$name);
      $docFine->CreateSet("MotionGroups_". $name, $filteredMotionsGroups);
}
```

```perl
# create a new cell but don't recalculate bonding as the bonds will be
non-sensical
my $lattice3D = $doc->Lattice3D;
Tools->CrystalBuilder->SetSpaceGroup($lattice3D->SpaceGroupCrystalClass);
Tools->CrystalBuilder->SetCellParameters(
      $lattice3D->LengthA, $lattice3D->LengthB, $lattice3D->LengthC,
      $lattice3D->AngleAlpha, $lattice3D->AngleBeta, $lattice3D-
>AngleGamma);
Tools->CrystalBuilder->Build($docFine, Settings(CalculateBonding =>
"No"));

my $runTime = time - $^T;
print "Total time taken: " . $runTime . " seconds\n";

###############################################################
# Subroutine to filter the items passed in by name

sub FilterByName
{
      my ($all, $name) = @_;
      my @filtered;
      foreach my $item (@$all)
      {
            if($item->Name eq $name)
            {
                  push(@filtered, $item);
            }
      }
      return \@filtered;
}
```

CURRICULUM VITAE

1. General

Name Surname:	M. Senem Avaz
Address:	Sabanci University Faculty of Engineering and Natural Sciences, 34956, Istanbul, TR
Date of Birth:	06.11.1985
Phone:	+905333403890
E-mail:	senemavaz@sabanciuniv.edu

2. Education

Year	Degree	School	Department
2017 (*July*)	Ph.D.	Sabancı University	Materials Science & Nanoengineering
2011-2012	Visiting Student	Bilkent University	Chemistry
2012	M.Sc.	Hacettepe University	Organic Chemistry (Computational Chemistry)
2008	B.Sc.	Hacettepe University	Chemistry
2003	High School	Özel Alp Lisesi *(Honor Student)*	-

3. Publications

ISI indexed	S. Avaz, R. B. Roy, V. R. S. S. Mokkapati, A. Bozkurt, Y. Z. Menceloglu, Graphene Based Nanosensor for Aqueous Phase Detection of Nitroaromatics, *RSC Advances,* **2017,** 7, 25519–25527 S. Avaz, O. Oguz, H. Kurt, Y. Z. Menceloglu, C. Atilgan, Soft Segment Length Controls Morphology Of Poly(Ethylene Oxide) Based Segmented Poly(Urethane-Urea) Copolymers In A Binary Solvent, *European Polymer Journal,* **2017,** *(Submitted)*
Google Scholar Indexed	*Selected Conference Paper:* S. Avaz, A. Taralp, Water Soluble Chitosan Derivatives via the Freeze Concentration Technique, *International Journal of Chemical, Molecular, Nuclear, Materials and Metallurgical Engineering,* **2015**, 9-2 *Book Chapter:* A. Zakharyuta, C. Şen, S. Avaz, T. Akkaş, S. Pürçüklü, T. Baytekin Birkan, T. Gönül, Laboratory Safety Handbook, *Sabanci University*, **2016**
Poster Publications, Oral Presentations	S. Avaz, A. Taralp, Water Soluble Chitosan Derivatives via the Freeze Concentration Technique, *ICP 2015: International Conference on Polymer*, **2015**, Paris, France S. Avaz, A. Taralp, Novel Synthesis Method For Chemical Modification Of Chitosan Derivatives with Enhanced Physical Properties, *247th American Chemical Society Meeting*, **2014**, Dallas, USA S. Avaz, A. Taralp, Chitosan Nanoparticles by Freeze Concentration Effect, *1st International Symposium on Nanoparticles/Nanomaterials and Applications*, **2014**, Lisbon, PORTUGAL

	S. Avaz, A. Taralp, Freeze-Concentration-Based Approaches to Prepare Novel Biomaterials, *IUPAC International Conference*, **2013**, Istanbul
	S. Avaz, V. Adar, Evaluation of Accuracy of Docking Results for Thrombin Inhibitors With Docking Program FlexX, *Drug Research & Development Conference*, **2009**
	S. Avaz, V. Adar, Synthesis of Beta Lactam Antibiotics by Staudinger Ketene-Imine Cycloaddition, *Drug Research & Development Conference*, **2009**, Ankara

4. Theses

M.Sc.	Theoretical investigation on conformational changes of HIV-1 protease enzyme during interaction with its inhibitors and design of new analogues, **2012**
Ph.D.	Experimental and Theoretical Approaches in Macromolecules Design, Synthesis, Modification and Nanosensor Applications, **2017**

5. Experimental Techniques

Organic Chemistry	1 year of experience in synthesis of Beta Lactam Antibiotics
Materials Synthesis	4 years of experience in chemical modification of natural macromolecules, nanoparticle synthesis from natural polysaccharides, molecularly imprinted films preparation
Micro/Nano Fabrication	1 year of experience in Class 100 Clean Room

6. Characterization Tools

Spectroscopy	Attenuated Total Reflectance-Fourier Transformed Infrared Spectrophotometer (ATR-FTIR), Ultraviolet-Visible Absorption Spectrophotometer (Uv-Vis), X-Ray Diffraction Spectrometer (XRD), Raman Spectrometer
Imaging	Scanning Electron Microscopy (SEM), Optical Microscopy
Thermal	Differential Scanning Calorimeter (DSC), Thermogravimetric Analyzer (TGA)
Physical	Dynamic Light Scattering DLS, Contact Angle, Surface Profiler, Plasma Asher, Thermal Evaporator, Deep Reactive Ion Etching (DRIE)
Thin Film, Coating	Spin Coating, Dip Casting, Electrospinning

7. Computational Methods

Atomistic Methods	Molecular Dynamics Simulations (MD), Molecular Docking
Mesoscale Methods	Coarse Graining, Dissipative Particle Dynamics Simulations (DPD), Fine Graining
Computational Tools	Materials Studio, Sybyl7.3, FlexX, SiteID, HyperChem7.5, AutoDock4.0, PMV1.5.4, ChemOffice 2004, Gromacs, VMD 1.8.7, UCSF Chimera molecular modeling and visualization tools, MestreNova, Origin Pro 8.0.

8. Academic Experiences

Year	Title	University	Department/Course
2012- present	Research Assistant	Sabancı University	Materials Science & Nanoengineering
2012-2015	Teaching Assistant	Sabancı University	Academic Support Program
2014	Teaching Assistant	Sabancı University	Introduction to Materials Science Course
2013-2014	Teaching Assistant	Sabancı University	Natural Sciences Course
2012-2013	Teaching Assistant	Sabancı University	First Year Math Course
2011- 2012	Teaching Assistant	Bilkent University	General Chemistry Lab Course

9. Personal Activities

➢ Rhythmic gymnastics Turkey championships winner (2000, 2001, 2002)
➢ Member of Rhythmic Gymnastics Turkish National Team (1999- 2005)
➢ National Rhythmic Gymnastics Judge (2007-present)

10. Scholarships

➢ Ministry of Youth and Sports, National Athlete Scholarship (2005-2014)
➢ Sabanci University, Full Ph.D. Scholarship (2012-2017)